NUMERICAL ANALYSIS OF RADIO FREQUENCY INDUCTIVELY COUPLED ION THRUSTER AND COMPUTATION OF ITS PERFORMANCE PARAMETERS

A THESIS SUBMITTED TO
THE GRADUATE SCHOOL OF NATURAL AND APPLIED SCIENCES
OF
MIDDLE EAST TECHNICAL UNIVERSITY

BY

ERDAL BOZKURT

IN PARTIAL FULFILLMENT OF THE REQUIREMENTS
FOR
THE DEGREE OF MASTER OF SCIENCE
IN
AEROSPACE ENGINEERING

OCTOBER 2019

Approval of the thesis:

NUMERICAL ANALYSIS OF RADIO FREQUENCY INDUCTIVELY COUPLED ION THRUSTER AND COMPUTATION OF ITS PERFORMANCE PARAMETERS

submitted by **ERDAL BOZKURT** in partial fulfillment of the requirements for the degree of **Master of Science in Aerospace Engineering Department, Middle East Technical University** by,

Prof. Dr. Halil Kalıpçılar
Dean, Graduate School of **Natural and Applied Sciences** _____

Prof. Dr. İsmail H. Tuncer
Head of Department, **Aerospace Engineering** _____

Prof. Dr. Nafiz Alemdaroğlu
Supervisor, **Aerospace Engineering, METU** _____

Examining Committee Members:

Prof. Dr. Serkan Özgen
Aerospace Engineering, METU _____

Prof. Dr. Nafiz Alemdaroğlu
Aerospace Engineering, METU _____

Prof. Dr. D. Funda Kurtuluş
Aerospace Engineering, METU _____

Prof. Dr. İsmail Rafatov
Physics, METU _____

Prof. Dr. Nevsan Şengil
Astronautical Engineering, THK University _____

Date:

I hereby declare that all information in this document has been obtained and presented in accordance with academic rules and ethical conduct. I also declare that, as required by these rules and conduct, I have fully cited and referenced all material and results that are not original to this work.

Name, Surname: Erdal Bozkurt

Signature :

ABSTRACT

NUMERICAL ANALYSIS OF RADIO FREQUENCY INDUCTIVELY COUPLED ION THRUSTER AND COMPUTATION OF ITS PERFORMANCE PARAMETERS

Bozkurt, Erdal
M.S., Department of Aerospace Engineering
Supervisor: Prof. Dr. Nafiz Alemdaroğlu

October 2019, 122 pages

The main goal of this thesis is geometric and parametric analysis of a simulated cylindrical two-gridded Radio Frequency Inductively Coupled (RF-ICP) ion thruster. In addition, instrumental performance of this thruster and the effects of a fixed shape of the electrodes on ion trajectories are investigated. The simulations of the plasma and the ion optics are performed by using COMSOL Multiphysics software. The first step is checking the reliability of the software. Radial and axial simulation parametric results of chosen experimental geometry are compared with the results of the experiment. After this validation, the coil turn, the anode electrical potential, the plasma chamber geometry, the coil RF electrical frequency, and finally, the coil location upon plasma chamber are changed, and the results are discussed.

The next step is focusing on the performance parameters that are thrust and specific impulse. For this purpose, Bohm ion velocity and the ion density at the sheath edge are determined to calculate the current density for the geometry ($AR = 2,\ CT = 3$). At last, ion optic system of the RF-ICP thruster is analyzed. Perveance and ion

trajectories of the thruster are studied. The optimum perveance is found as 1.09486×10^{-6} $A/V^{3/2}$ for 9.49 mA Child current. Also, the effects of specified boundary which ions are released are investigated to the trajectories of the ions.

Keywords: Plasma Physics, Inductively Coupled RF Plasma, RF ICP Ion Thrusters, COMSOL

ÖZ

RADYO FREKANSI İNDÜKTİVE EŞLENİKLİ İYON İTİCİSİNİN SAYISAL ANALİZİ VE İTİCİNİN PERFORMANS PARAMETRELERİNİN BİLGİSAYAR ORTAMINDA HESABI

Bozkurt, Erdal
Yüksek Lisans, Havacılık ve Uzay Mühendisliği Bölümü
Tez Yöneticisi: Prof. Dr. Nafiz Alemdaroğlu

Ekim 2019 , 122 sayfa

Bu tezin ana hedefi 2 elektrotlu RF-ICP plazma iticisinin bilgisayar ortamında simülasyonunu ve bu doğrultuda geometrik ve parametrik analizleri yapmaktır. Ek olarak, bu iticinin aletsel performans hesabı ve geometrisi sabit tutulmuş elektrotların iyon yörüngelerine olan etkisi incelenmiştir. İticiye ait plazma ortamına ve iyon optiğine ait simülasyonlar COMSOL Multi-fizik yazılımı ile gerçekleştirilmiştir. Gerçekleştirilmiş ilk adım bu yazılımın ürettiği simülasyon sonuçlarının güvenirliğinin test edilmesidir. Bu yolla, deneysel analizleri yapılmış bir sistem ve bu sisteme ait geometri literatürden seçilmiştir, sonra da radyal ve eksenel parametrik sonuçlar COMSOL da yapılan simülasyon sonuçları ile karşılaştırılmıştır. Bu güvenirlik testinden sonra, sarım sayısı, anot elektriksel gerilimi, plazma odası geometrisi, sarımlara bağlanan RF gücün frekansı, ve son olarak ta sarımların plazma odası üzerindeki yerleri değiştirilerek simülasyonlar yapılmış ve sonuçlar tartışılmıştır. Sonraki adım RF ICP iticisinin performans parametreleri olan itki ve özgül itki hesabı olmuştur. Bu amaçla plazma kabuk kenarı üzerinde Bohm iyon hızı ve iyon sayı yoğunluğu, ardından da

elektrik akım yoğunluğu hesaplanmıştır ($AR = 2,\ CT = 3$). Son olarak RF ICP iyon iticisine ait iyon optik sistemi için simülasyonlar, perveance ve iyon yörüngeleri için hesaplar yapılmıştır. İyon akımı $9.49\ mA$ iken en iyileştirilmiş perveance değeri $1.09486 \times 10^{-6}\ A/V^{3/2}$ olarak bulunmuştur. Aynı zamanda, iyonlar 2'li ızgara sisteminde, ekran ızgarası üzerinde farklı yüzeylerden Bohm hızında harekete bırakılmış ve bunun iyon yörüngelerine olan etkisi incelenmiştir.

Anahtar Kelimeler: Plazma, Indüksiyon Eşlenikli Radyo Frekans Plazma, RF İyon Plazma İticileri

To all my family member

Meral Bozkurt, Kemal Bozkurt, Haydar Bozkurt, Döndü Bozkurt

ACKNOWLEDGMENTS

I would like to thank my supervisor Professor Nafiz Alemdaroğlu for his constant support and guidance. It was a great honor to work with him for the last ten years and our cooperation influenced my academical and world view highly. I also would like to thank Post. Dr. Ümmügül Erözbek Güngör and Professor İsmail Rafatov for their support and guidance. Dr. Ümmügül has provide to me an academic perspective and work support. I also thank to Prof. İsmail Rafatov for the knowledge that he has contributed the computational skils to me. Working with all of them is great honor for me.

TABLE OF CONTENTS

LIST OF TABLES

TABLES

LIST OF FIGURES

FIGURES

LIST OF ABBREVIATIONS

ABBREVIATIONS

EP	Electric Propulsion
MHD	Magneto Hydro Dynamics
MPDT	Magneto Plasma Dynamic Thruster
PPT	Pulsed Plasma Thrusters
RF	Radio Frequency
RIT	Radio Frequency Ion Thruster
ICP	Inductively Coupled Plasma
Isp	Specific Impulse
1D	1 Dimensional
2D	2 Dimensional
3D	3 Dimensional
CT	Coil Turn
AR	Aspect Ratio
V_{bound}	Voltages of the Chamber Boundaries
n_e	Electron Number Density
n_ε	Electron Energy Density
μ_e	Electron Mobility
E	Electric Field
D_e	Electron Diffusion Constant
n_ε	Electron Energy Density

CHAPTER 1

INTRODUCTION

1.1 Propulsion systems

Propulsion systems are composed of some devices that supply an action force to the system or change the velocity of the spacecraft. The system can move freely by using these devices. There are two types of propulsion systems. One of them is the chemical propulsion and the other one is the electric propulsion. The first artificial satellite was the Sputnik 1 and it was launched in 1957. After its launch, thousands of these spacecrafts have been delivered into the space. Orbit transfer, station keeping or maneuvering were the base motions for them. Therefore, the chemical space thrusters have been used. On the other hand the propulsive performance of the chemical thruster was limited by the energy of the chemical fuel, which they contained. The engineers and scientists have tried to find a way to increase efficiency of the thrusters.

The major advantage of the EP (Electric Propulsion) is the low mass fuel consumption due to high fuel velocity. As compared, the chemical engines consume much more fuel. They work on during very small time period while the EP thrusters can work on during thousands of hours continuously without failure. The only drawback of EP is that they produce small amount of thrust due to low exhaust gas mass flow rate level. The thrust is in the mili-Newton level when compared with the chemical engines, which produce thousands of tons propelling force. Therefore, to reach a velocity of the particular space mission takes much longer time than that of the chemical ones. However, the constellation mission of the CubeSat spacecrafts needs very small, accurate and gently pushing force to achieve the fine positioning between each other and this case is important due to requirement of the mission not to be limited with

time. Additionally, in the future, the EP technology would be more preferred after the improvement of the solar array technology and their enhanced energy production efficiency.

As an additional way of the space propulsion, electric thrusters consist of the large spectrum of thruster family. They are electrothermal, electrostatic and electromagnetic propulsion.

1.1.1 Electric Propulsion Types

According to the acceleration principles of the propulsion system, they are classified with three major titles: electrothermal, electrostatic and electromagnetic propulsion.

1.1.1.1 Electrothermal thrusters

These types of thrusters use electric energy for the heating of propellant, the examples of these types of thrusters are the resistojet and arc jets. The heated propellant is released from an expanded nozzle and the heat or enthalpy transforms to kinetic energy of the gas and the required acceleration is obtained by this way. The generated energy or velocity of the heated gas is determined from the temperature of it at the upstream of the nozzle. The operating principle of the resistojets is the ohming heating of the gas via electric current passing through a "heater" or "resistor" which is made from a conducting wire, as shown in the Figure 1.1a. Its main disadvantage is that it has low specific impulse value $300 - 400$ s , on the other hand, the main advantage of it is having higher thrust values up to 10 N when compared to the other electrical thruster types.

In order to compensate the amount of the lower specific impulse problem, the arc jets were developed which its basic schematic is shown in the Figure 1.1b. The heating mechanism is changed as compared to the resistojets and rather than heating the gas via electric resistors, the propellant gas is heated with high arc current in the ionized gas. It is created between an upstream conical cathode and a downstream annular anode through the expanded exhaust nozzle. The ionized gas temperature is much

higher than current supplier electrodes. Therefore, the velocity of the released gas is much higher than that of the resistojets.

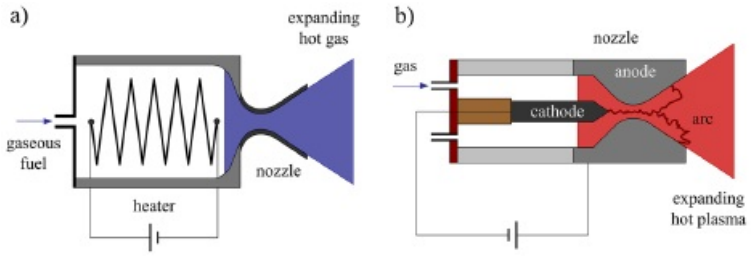

Figure 1.1: a) Resistojet thruster , b) Arcjet thruster [3].

In the arc jets, the specific impulse can reach to 1000 s based on the used fuel such as hydrogen, hydrazine or ammonia. The main disadvantage of the arc jet thrusters is the erosion problem of the electrode. The arc current heats them and metal ablation problem takes place and the erosion of the electrodes is an issue in that point.

In the early 1980s, resistojets were used for the station keeping and attitude control of commercial satellites. The first arc jet was taken advantages on the satellite AMSAT-OSCAR 13, in 1988 [14].

1.1.1.2 Electromagnetic Propulsion

Magneto Plasma Dynamic Thrusters (MPDT) and Pulsed Plasma Thrusters (PPT) are included in this type of electric propulsion field and their related schematic pictures are shown in the Figure 1.2. Electromagnetic thrusters take advantage of not only from electric fields and but also the magnetic fields to accelerate the fuel. By this process, they produce enough thrust for the planned mission. With a pulsed discharge enough amount solid fuel is ionized and acceleration takes place in PPT's by means of the external magnetic field and with the result of the Lorentz Force [15], which is seen as purple arrow in the Figure 1.2-b.

MPDTs use too much electrical current to ionize lots of portion of the propellant gas. When the fuel gas is injected to the thruster chamber, the gas atoms are ionized between the anode and cathode due to the electric field. Meanwhile, the current produces the magnetic field which is perpendicular to the electric field and the resulted

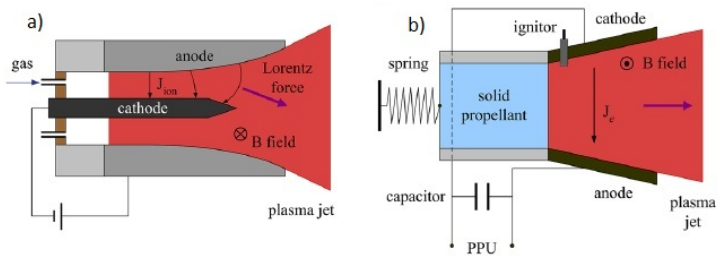

Figure 1.2: a)MPDT and b)PPT [3].

Lorentz Force $F = j \times B$ pushes the plasma from the thruster chamber toward the exit of the nozzle. When the power supply is weak to produce self-sustaining magnetic field and to generate Lorentz force, an external magnetic field is used. MPDTs sustain very high thrust level as compared to the other EP types. On the other hand, very high level power supplies are needed for the operation of these thrusters. Up to date, a MPDT requires 500 kW of electric power working with 8 kA electrical current for generating 20 N-thrust [16]. Nonetheless, to reach such level of power seems not possible with the current technology. On the other hand, the nuclear power technology especially fusion reactors will enable to sustain this kind of power level with the plasma engineering in the near future .

1.1.1.3 Electrostatic Propulsion

In an electrostatic thruster, the plasma is generated by using an RF or DC (Direct Current) source. Emerging ions are pulled away from the screen grid and accelerated toward to the other grid which is called accel grid. On the other hand, some electrostatic thrusters such as Hall Effect thrusters use double layer sheath mechanism instead of the grids.

a) Hall Effect thrusters:

Another type of EP is the Hall Effect thrusters. The thrust and the specific impulse levels of the Hall Thrusters are acceptable for the North-South station keeping of geosynchronous orbit telecommunication satellites. Although the mechanical structure of the Hall thruster has intermediate-level hardness, their physical working principles are very complicated. The working fuel, which is most frequently neutral

Xenon gas, is injected from the holes of the anode part of the thruster. Also, the anode part is biased with positive potential with respect to external cathode. The external cathode delivers not only free electrons to the thruster and but also the electrons which are neutralizing the positive charged ion beam. By this way, the system is prevented from biasing with negatively. The electrons which are coming from the neutralizer to the interior region of the thruster is trapped within $E \times B$ field and azimuthal Hall current is built up as seen in Figure 1.3.

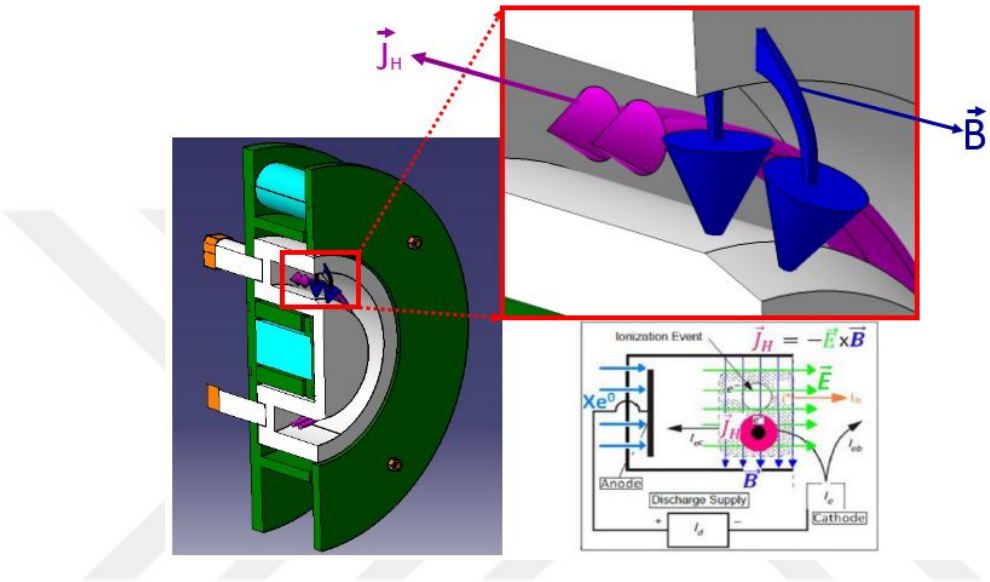

Figure 1.3: Hall Thruster Schematic

The E field is generated between the anode and cathode; on the other hand, the magnetic field B is radially oriented. The magnetic field is between the outward and inward part of the gate in the thruster and it is produced via the external electromagnetic coils or with the permanent magnets. The appearance of the plasma channel has annular ring shape geometry as is seen in the Figure 1.3 with a white-grey color. When working fuel is encountered with the electrons where Hall current is, they are ionized and free ions emerge. Later, the acceleration of the ions take place since they see the electric field between the anode and cathode. The ions are not affected by the magnetic field due to their large mass with respect to that of the electrons. As a result of these processes, the desirable thrust is obtained.

b) Ion Thrusters: Ion thrusters, also known as ion engines, are electrostatic thrusters that depend on Coulomb forces to accelerate positively charged ions having heavy

atomic nucleus such as, Ar and Xe atoms. They are often used for propellant in every type of electric thrusters due to having non-toxic structure. First of all, the relation between thrust density and atomic mass of the propellant is given at the Eq.1 from the reference [17]. According to the Eq.1 when M_i increases, the thrust density also increases with the square of the atomic mass of the used propellant. The derivation of the Eq.1 is completed at the Appendix-A

$$\frac{T}{A} = \frac{2}{9e^2}\varepsilon_0 \frac{v_{ex}^4}{d^2} M_i^2 \tag{1}$$

where T is total produced thrust, A is the total grid area which ions are passing, e is the unit charge, ε_0 is the permeability of the free space, v_{ex} is the exhaust ion velocity, d is the diameter of the one hole of the screen grid, M_i is the atomic mass of the used propellant.

When the atomic mass of the propellant increases at the same amount of the exhaust gas velocity, they sustain higher momentum and therefore they produce more thrust-per-unit-area than light weight nucleus . The other way to increase to the thrust density is to increase the exhaust gas velocity. Because thrust density is related with the forth power of the exhaust gas velocity.

Although an ion thruster which consists of an ionization chamber with or without an internal electron source cathode, a grid system is used for ion extraction and acceleration. Also, the external electron emitting cathode is mandatory for the neutralization of the ion beam; otherwise, the spacecraft would be charged with negatively.

At the same time, with the neutralization process, the ions are not attracted back by the thruster chamber, on the other hand, the ions would flow back to the plasma chamber due to the negative electric field between the ion plume region and accel grid. Therefore, the net thrust would not decrease in some amount with that prevented ion back-streaming [18].

The major disadvantage of the ion thrusters is the limitation of the ion current density due to the positive charge accumulation between the screen and accelerator grids. While they are passing from the grid, ions repel each other due to their same positive charge and the electrons are absent between gaps at significant amount. The extracted

ion current cannot exceed the level at which the repulsing force between the ions is at the high amount in the gap and they would keep new ions from entering. This effect is called the space charge limitation and it reduces the thrust density seriously. Therefore, ion thrusters must have a bigger exit area than the Hall thrusters with the same thrust level.

Because there is not any space charged limited issue in the Hall Effect thrusters, and the extracted current that is taken from the thruster is not limited. The generation and acceleration of the ions is sourced due to quasi-neutral plasma [18, 19]

The most common type of the ion thruster is the direct-current (DC) electron-bombardment ion thruster which firstly advanced by Kaufman from NASA in the 1960s [20]. Other types of the ion thrusters include inductively-coupled plasma (ICP) discharge radio-frequency (RF) ion thruster and electron cyclotron resonance (ECR) RF ion thruster. The studies on the ICP RF ion thrusters have been initiated by German scientists [21, 22], on the other hand, works on ECR RF ion thrusters have been mainly initiated in Japan [23].

The comparison of the performance parameters of the propulsion types is seen from the Table 1.1.

Table 1.1: The table of typical operating parameters for thrusters with flight heritage [1].

Thruster	Specific Impulse (s)	Input Power (kW)	Efficiency Range (%)	Propellant
Cold gas	50–75	-	-	Various
Chemical (monopropellant)	150–225	-	-	N_2H_4 H_2O_2
Chemical (bipropellant)	300–450	-	-	Various
Resistojet	300-400	0.5–1	65–90	N_2H_4 monoprop
Arcjet	500–1000	0.9–2.2	25–45	N_2H_4monoprop
Ion thruster	2500–3600	0.4–4.3	40–80	Xenon
Hall thrusters	1500–2000	1.5–4.5	35–60	Xenon
PPTs	850–1200	<0.2	7–13	Teflon

-RIT: The first tested RF ion thruster in space launched by the Space Shuttle Atlantis in 1992. It was a technology demonstration project onboard European Retrievable Carrier (EURECA) spacecraft. RIT-10 worked for 250 hours and it produced 5-10 mN thrust and obtained 3000 s specific impulse for this first mission, on the other hand, it ended with failure. The reason of it was the overheating problem of plasma coils and discharge chamber at the end of 240 hours. At the later version of the RF ion engine, this problem was solved and the RIT-10 was onboard for the Advanced Relay Technology Mission Satellite (ARTEMIS) for 7500 hours [24]. After the malfunction of the upper stage engine of the ARTEMIS, the remaining orbit was completed with RIT-10. The first orbital transfer to geostationary orbit using RF ICP ion propulsion with the 15 mN thrust achieved at 19 February 2002 [4,22,24,25]. The journey lasted 7.500 hours. Figure 1.4 shows the RIT-10 ICP ion truster [24].

An RF-ICP ion thruster is basically composed of an axisymmetric, conical, spherical or cylindrical discharge chamber which can be made of a dielectric material and a helical spiral coil wrapped around this chamber that is feed with RF current whose

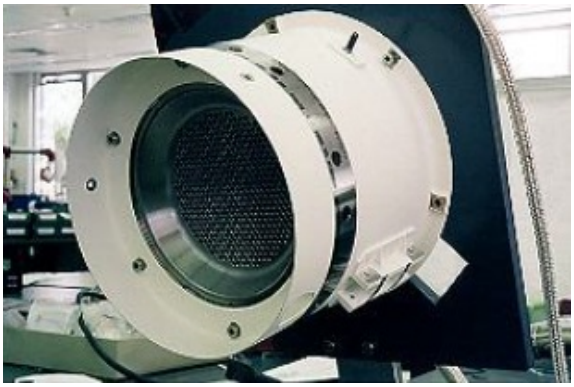

Figure 1.4: RIT-10 [4].

frequency is at low mega-hertz range. This RF current is responsible for the creation of the plasma and to sustain it. The grids are responsible for the extraction and acceleration of the ions and to generate thrust.

In fact, working principle of RF-ICP thruster is explained as follow. The electrons are released from an external cathode. These electrons are pulled into the chamber of the thruster due to the high positive potential of the screen grid with respect to the ground [22]. The neutral particles are bombarded by these electrons and more free electrons emerge in the medium and the plasma is ignited in the discharge chamber. When the coils around the chamber are fed with RF currents, they create the oscillating magnetic field along the chamber symmetry axis and this magnetic field induces the oscillating azimuthal electric field. That process obeys to the Maxwell Faraday's Law of induction. This electric field accelerates the electrons azimuthally through the channel. More emerging electrons collide with neutral particles along with their trajectory and the further ionizations take place. Therefore, sustainability of the plasma is preserved. By this way, the coil electric power is transferred to the plasma. In order to full forward electric power absorption, an impedance matching device should be used. Because when the coil impedance match with the plasma impedance, full power absorption is possible between the coils and the plasma. For trust generation, two or three grids can be used. The first grid keeps the plasma at the certain level of electric potential, extracts the ions from chamber with a slow velocity with respect to ion plume velocity. After the extraction process, the ion beam is accelerated with the presence of the second grid which is called accel grid which has the negative po-

tential with respect to the ground, and it also focuses the ion beam. Moreover, the back-streaming of the electrons which is coming from neutralizer is prevented by the negative electric potential between accel grid and plume. Due to these process the transportation of the electrons to the plasma chamber is prevented and the ionization efficiency is enhanced and therefore the obtained thrust is increased with this extra amount of the ions. The illustration of two-grid RF ion engine is shown in the Figure 1.5 [24].

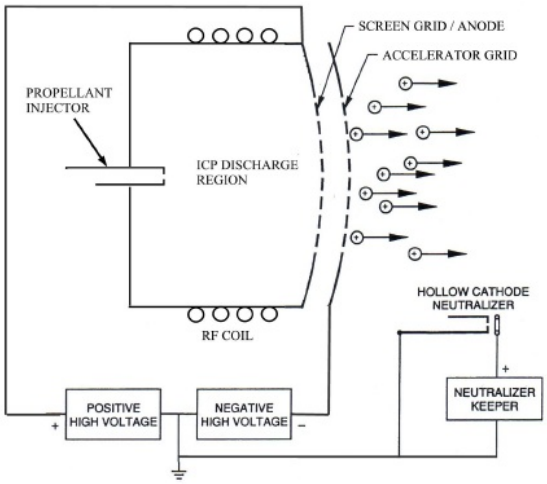

Figure 1.5: The Basic Schematic of the Simple Two-Grid RF Ion Engine [5].

The precise manoeuver controlling of RF ICP ion thruster is possible by adjusting the applied RF electrical power. That condition is mandatory for the fine tuning missions like as the formation flight [5], gravitational wave detectors [26], space interferometers [27] and advanced space telescope applications [28].

The second advantage of the RF ICP ion thruster is that they do not need any internal electron emitter cathode. From the replacement of the cathode to the utilization of the RF coil, the main parameter for erosion of thrusters is eliminated [5]. Therefore, the lifetime of the thruster can be suspended at the order of 15 000 hours [29]. In addition, due to the absence of the interior cathode, the thruster would be smaller in volume and size. The RF ICP ion engines do not need any electromagnet or permanent magnet to confine the plasma [24]. Therefore, they can be much lighter, much smaller and much more efficient than its other correspondent although all ion thrusters are using the same ion acceleration mechanism. However, their plasma production mechanism

isn't the same [5, 30]. Additionally, mechanical construction of the RF-ICP is very simple in contrast to the Hall Effect thrusters and MHD thrusters. So, the easy manufacturing of a RF ICP ion thruster is an advantage [31]. The RF ICP ion source has high plasma density which is at the level of $10^{18}\ m^{-3}$ and they can be operated at the low gas pressure ($\sim$ 1 mTorr). These working parameters are very suitable when the high fraction of the ionization rates and the space conditions are needed [31]. The RF ICP ion engines have lower beam divergence, higher thrust and higher ion beam velocity when compared to that of the Hall Effect thrusters [32]. When the beam divergence is smaller, the contamination at the spacecraft becomes smaller. Therefore, the electric hardware, such as cameras and solar arrays, is affected lesser from the high energetic ion beam which gets out of the thruster.

Due to the RF ICP ion engines are very scalable in size and in power level, they are used in nanosatellite applications. Moreover, the inductive plasma in an RF ion thruster is maintainable for a wide range of the propellant flow rate and RF power [24]. Mercury, Argon, Krypton and Xenon are used as a propellant gas in RF-ICP ion thrusters. Among these, Xenon is the most preferable propellant due to low first ionization energy (12.1 eV) and its high atomic weight (131.3 g/mol). The more efficient usage of the discharge power is sustained with this low ionization energy [33]. Also, the more the mass of the propellant means that, the more the thrust density is and this situation is seen with the calculation in the Eq.1 of two different mass for two different propellant. Advantages and disadvantages are summarized briefly so:

-Advantages of the RF ICP ion thrusters:

-High specific impulse values 3500-7000 s

-Simple mechanical design

-Lower thruster volume

-Low ion beam divergence angle <17-25 Degree

-Long operational life time >20.000 hour (>2.282 year)

-High electric efficiency (70-75%)

-Disadvantages of the RF ICP ion thrusters:

-Due to space charge effects, limited accelaration voltages and the risk of the inducing arc between grids with the increasing electric potential drop.

-The life time problem due to erosion of the electrodes

-High temperature working environment.

1.2 Thruster Principles

1.2.1 Thrust

Production of thrust in the electric propulsion systems depends on the same physical principle as the thrust generation for the chemical engines. Both of them accelerate and eject the propellent from spacecraft with a very high velocity. The mass which leaves from the spacecraft pushes it at the opposite direction with the time rate change of the momentum of the ejected material. This propulsive force is called thrust and it is expressed with $T = \dot{m}v_{ex}$ where $\dot{m}$ is the mass flow rate of the ejected propellant and v_{ex} is the ejected exhaust gas velocity of the propellant.

1.2.2 Rocket Equation

The acceleration of the spacecraft via thrust takes place with the Newton's second law. If the spacecraft is not in the atmosphere such as in upper space orbit, the drag and gravity losses can be neglected and the acceleration of the spacecraft can be expressed with the Eqn 2 from the reference [19]. The Eqn 2 means that obtained thrust is the opposite side of the time rate of the change of the momentum via accelerated and ejected propellant gas.

$$T = -\frac{\mathrm{d}}{\mathrm{d}t}(m_p v_{ex}) \tag{2}$$

where m_p is the total propellant mass and v_{ex} is the exhaust gas velocity. If the 2nd

law of the Newton is written the Eqn 3 is obtained.

$$T = M(t)\frac{\mathrm{d}v}{\mathrm{d}t} = -\frac{\mathrm{d}}{\mathrm{d}t}(m_p v_{ex}) \tag{3}$$

where $M(t)$ is the total mass of the spacecraft as the sum of the propellant mass of the spacecraft, v is the velocity of spacecraft. The M decreases with time by ejection of the propellent.

If the required calculation is done the Eq.4 is obtained. The derivation of the Eq.4 is completed in the Appendix-B.

$$m_p = m_d[e^{\Delta v/v_{ex}} - 1]. \tag{4}$$

where m_d is the dry mass of the spacecraft. Δv differs from a mission to another one. When it is high, the propulsive requirement of a given mission is also high. For a given Δv , it is clearly seen from Eq.4 that when v_{ex} exhaust velocity is higher, the needed propellant mass is lower. Due to this benefits of the mass reduction of the propellent, the quantity of the exhaust velocity has important point and it determines the thrust performance characteristics of a propulsion device. A typical rocket engine with bipropellant fuel has $3 \sim 4$ km/s exhaust gas velocity. On the other hand, when an electric propulsion thruster is used, it can reach to $10 \sim 40$ km/s [19]. In the chemical propulsion, the exhaust velocity depends on the chemical bonds in the fuel. Therefore, it is limited with molecular bound of them. On the other hand, there is not any kind of limitation in the electric propulsion. The only limitation is related to the electric power. Thus, it depends on which kinds of power supply is used such as nuclear, solar, or so on..

Because of the lots of successful space missions, the advantages of electric space propulsion have been seen explicitly. In order to notice it, the SMART-1 mission can be considered. This satellite was mainly Sweden designed spacecraft and it was in the orbit on September 27, 2003. It is launched from Guiana Space Center and later it was in the orbit of the Moon thanks to the Hall Effect electric propulsion thruster. The exhaust velocity of this engine was about 16,100 m/s. The Δv of this mission was 3.9 km/s and the dry mass of that spacecraft was 287 kg. When these parameters

are plugged into the Eq.4, the mass of the calculated required propellant is found as 78.73 kg. At the beginning of the mission, 82 kg Xenon propellant was loaded to this spacecraft and 3.27 kg propellant was redundant in the case of some problems such as the gas leakage. If a chemical propulsion device was used for the same mission with having 4000 m/s exhaust velocity, the fuel mass budget of this spacecraft would be completely different. After the calculation by using Eq.4, it is found that 474 kg fuel would be needed for that chemical propulsion device in the same mission and it shows to the advantage of the electric propulsion technology.

1.2.3 Specific Impulse

In the literature of the propulsion engineering, the specific impulse is the ratio of the thrust for the propellant weight consumed in the unit of time. Specific impulse for constant thrust and propellant mass flow rate is given with the Eq.5 from the reference [19].

$$I_{sp} = \frac{T}{\dot{m}g} = \frac{v_{ex}}{g} \tag{5}$$

where g is the acceleration of gravity, 9.807 m/s. Specific impulse is a measure of how efficiently thrust is produced and this thrust efficiency is related to the propellant exhaust velocity.

1.2.4 Total Efficiency

The total efficiency of an electric propulsion device is the ratio between the jet power and input electrical power, P_{in}. Jet power P_{jet} is the kinetic thrust power of the plasma beam which is leaving from the thruster. With the measurement of the thrust of the engine, with the mass flow rate for the fuel consumption and input electric power, the total efficiency can be expressed by Eq.6 from the reference [19].

$$\eta_T = P_{jet}/P_{in} = \frac{T^2}{2\dot{m}P_{in}} \tag{6}$$

1.3 Outline of the Thesis

This thesis is structured as follows: The second chapter presents a brief literature survey. The third chapter presents a review of the fundamental concepts of the plasma physics. The forth chapter includes a benchmark problem of an experimental system to successfully validate the numerical solutions of the COMSOL Multiphysics software. The fifth chapter involves plasma chamber simulations. In this way, the changes on the plasma parameters are examined when the coil turn, the anode voltage, the chamber geometry, the coil RF frequency and the location of the coils are changed. The sixth chapter includes, the performance values of the RF ion thruster such as thrust and specific impulse are calculated with the final plasma chamber geometry by changing the plasma gas pressure, coil electric power and RF coil frequency. Furthermore, the examinations of the ion trajectories are performed and the proper ion trajectories are traced. The last chapter consists of the conclusion.

1.4 Objective:

The objective of this thesis is to understand the RF inductively coupled plasma production process by adjusting the macroscopic physical parameters, such as, system power level, discharge gas pressures and RF coil frequency. In this way the aim is to determine the physical parameters of the plasma such as, plasma density and plasma temperature. The second aim is to examine the proper ion trajectories and to extract the ions from the plasma chamber with sufficient rate. Finally the last aim of this thesis is to obtain the thruster performance parameters by changing other macroscopic system parameters such as gas pressure, system electric power level and RF coil electric frequency. For these purposes commercial numerical software, COMSOL, is used to understand the quantity and distribution of this plasma parameters in the chamber and to see the proper ion trajectories.

CHAPTER 2

LITERATURE SURVEY

The numerical modelling efforts about the plasma physics are relatively new in the scientific world. Numerical simulations upon inductively coupled plasma is implemented a lot of times in the litreture. The heating of the gas is performed with electromagnetically and it is the fundamental part of this process. In terms of the underlying physics of the RF ion thrusters and not only plasma processing and but also plasma torching have the same physical principles. The numerical workings upon these two areas also helps to understand principles of the RF ion thrusters. As for the plasma processing, Kawamura [34] offers a numerical model for inductively coupled plasma. Suekane [35] presented a simpler version of inductively coupled plasma model for plasma torches, which the model developed in this study greatly benefited from. This work includes the evaluation of the boundary conditions for the electromagnetic equations. Hammond [36] built a 2D fluid model of the inductively coupled plasma, which is an example how to handle the electron energy equation. Kumar [37] and Hsu [38] also provided numerical models for inductively coupled plasma, incorporating energy equations for electrons and also other species along with the boundary conditions. Parent [39] developed a new scheme to solve for the species transport equations using fluid model for plasma. Additional to the RF plasma modeling efforts, there are other methodologies developed to simulate other EP plasma devices. The state of the art in plasma modeling for electric propulsion applications is using the kinetic model with the Particle-In-Cell (PIC) algorithm. Oh [40] laid out the basics of the particle tracking simulations for quasi-neutral plasma. Fife [41] developed a hybrid-PIC simulation scheme where the electrons are assumed to be fluid but remaining species are tracked using particles. Szabo [42] developed a fully kinetic model for plasma thrusters. The code AQUILA [43] is developed to simulate Hall thruster plume us-

ing the Hybrid-PIC approach. There are few numerical models for ion thrusters in general, and there are models for inductively coupled plasma, but the number of the models for RF ion thruster is very limited. A leading example [44] is based on evaluating the discharge loss per ion with an analytical model. This 0D model is simple but successful at predicting the performance of ion thrusters in real applications. It lays out the effect of the induced magnetic field due to the RF coils on the ion confinement and discusses factors that result in a decrease in the discharge loss per ion. Another recent 0D model [45] indicates a tradeoff between mass utilization efficiency and power transfer efficiency with increasing gas flow rate. Additional to the analytical models, there are also one or multi-dimensional RF ion thruster discharge chamber modeling studies. A simple transformer model [46] is first laid out for 1D modeling, assuming that the thruster is large enough to assume 1D approach could be valid. Then this model is extended to a 2D model [24] which evaluates the plasma parameters of RF ion thrusters with the help of additional experimental data specific for the thruster to be modeled. In that study, the plasma is treated as a continuum as it is treated in the same way as in this work. There are also studies with the kinetic approach, using a PIC (Particle-In-Cell) code to solve for the spatial distribution of the plasma parameters. An example model [47] is developed to evaluate the performance of the micro RF ion thrusters. A 3D fully kinetic model [48], that requires strong computation power, is laid out recently for RF ion thrusters. Compared to a PIC code implementation, the usage of the fluid approach decreases the computational cost drastically. Plasma must obey the continuum approach for the fuid modeling to be possible. The investigation whether the inductively coupled plasma inside the RF ion thruster discharge chamber obeys thecontinuum approach is already performed[24].

CHAPTER 3

BASIC PLASMA PHYSICS

The RF ICP ion thrusters produce thrust electrically. Working principle of these thrusters is based on the plasma discharge physics. It is very important to understand the physics of these devices to improve the application for the spacecraft missions. For this purpose not only theoretical but also experimental studies are initiated and are backed by numerical studies. The numerical analysis for thrusters is essential to map the physical structure of the system. In this way, the performance of the thrusters can be controlled by optimizing the relevant physical parameters. These basic plasma physics concepts are required for simulating the system. This is why this section on basic concepts of the plasma physics are introduced.

3.1 What is the Plasma?

In the universe, more than 99 % of the observed matter consists of plasma. It is the forth state of matter [49]. The particles in this state are very energetic with high temperature. For example, ionosphere layer of the earth is in the plasma state. The plasma objects in the space can be seen from the earth clearly. Therefore, the astrophysics and space sciences are closely related with the plasma science. Some examples of the plasma objects are;

- Aurora borealis
- Solar wind
- Magnetosphere of Earth and Jupiter
- Solar corona and sunspots

- Comet tails
- Gaseous nebulae
- Stellar interiors and atmospheres
- Galactic arms
- Quasars, pulsars, novas and black holes.
- Light bulbs
- Laboratory plasmas [8].

If the molecules in the gas state are heated enough, the particles are ionized and the electrons begin to oscillate. Then, the state is changed into the plasma. The method of heating can be different from that of the chemical reactions. They are realized by electromagnetic forces such as RF ICP system or by means of electromagnetic wave heating, like in microwave heating. When the electrons acquire enough energy, their kinetic energies override the electrostatic bonding forces of the atoms and the ionization takes place. They move around of the atom freely and the plasma is generated. If a quasi-neutral gas contains charged and neutral particles this is called as "plasma" [6].

In the 1920s, the famous scientist Irving Langmuir did his first experiments on the gas discharges. During the World War II, the invention of the microwave tubes to generate radar is used as the first important application of it. In the 1950s, the plasma physics became hot topic for the study of the controlled nuclear fusion reactor. By means of it, the conditions of the core in the stars are recreated and the abundant amount of energy are taken. In order to get these conditions the required plasma number density should be more than $10^{19}\ cm^{-3}$ and the plasma temperature should be sustained between 10 to 100 keV [8,50]. If this idea is put into practice, the biggest invention of the human history could be achieved since the invention of the fire. Because the humanity can not provide this amount of energy until now, since it would be only possible by using the nuclei of the heavy hydrogen atom that is abundant in our oceans for this purpose [8].

Expect the usage of the nuclear fusion in the wide range of the spectrum, the plasma are used in such devices as microwave tubes, gas lasers, free-electron lasers, etc. The plasma based particle accelerators are used by the high energy physics [8].

Intense X-ray sources using pulsed power technology to simulate the nuclear weapons' effects. The National Ignition Facility is being built at Livermore, California for internal confinement fusion. The femto-second lasers can produce plasmas for the need of the studies of the very short time scale chemical and biological events. In the industrial plasmas which is cooler, higher pressure and having high complexity are being used for hardening-coating of the metals, such as in airplane turbine blades and automobile parts. The plasma is used for treating plastics for paint adhesion, and for forming diamond coatings. The application of the plasma science over the semiconductor manufacturing is very important. Without the use of plasma, no-fast computer chips could be manufactured. Magneto hydro dynamic generators with high power conversion efficiency produce more electricity than that of a conventional coal or gas based thermo electric power plant.

The other main usage area of plasma physics is in the propulsion of the spacecraft in free space. The plasma thrusters are mainly used in this field and it is thought that the journey to Mars for the mankind may be sustained with a plasma based thruster thanks to the significantly low propellant mass requirement and with enough electric power supply.

3.2 Debye Length

One of the fundamental parameters of the plasma physics is the Debye Length. It defines the distance of the penetrated electric field into the plasma and therefore it exhibits the electric potential distribution throughout the plasma and its quasi-neutrality.

At the beginning, electrons are so mobile that they leave the bulk plasma much more rapidly than the ions due to their smaller masses. The ratio of the mass between a hydrogen ion and an electron is $m_i/m_e \sim 1836$ and therefore the thermal velocity of the electrons is much higher than that of the ions and the ions can be thought as stationary. Later they left behind from electrons and it causes the net positive charge in the bulk plasma. After that, a very strong electric field emerges due to the net positive charge which prevents any further loss of the electrons. These electrons are pulled to their original position and the condition of the quasi-neutrality is maintained

in the bulk plasma.

Every charged particle does surround each other in order to sustain the quasi-neutrality of the plasma. When there is a local displacement of the charge at the unit volume, strong electric fields emerge at the space of the plasma which obeys to the Eq.7 which is known as the Poisson's equation.

$$\vec{\nabla}.\vec{E} = \frac{1}{\varepsilon_0}(n_i - n_e) \tag{7}$$

where $\vec{E}$ is the electric field, n_i is the ion number density, n_e is the electron number density, ε_0 is the permeability of the free space.

Eq.7 says that when the right hand side of Eq.7 is larger than zero, the net charge is positive and there is an electric flux passing outside the closed surface which is a boundary of a sphere as shown in Figure 3.1.

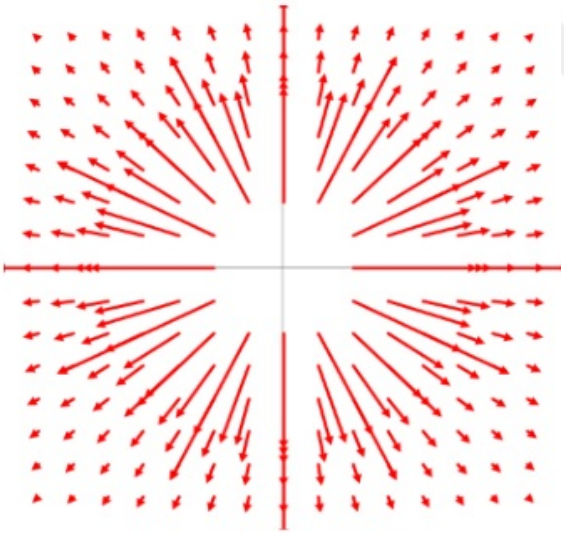

Figure 3.1: Electric Field Distribution at the 2D circular space.

Figure 3.1 says that when the distance r is increasing from the center point of the unit sphere, the electric field decreases with the inverse square of the r distance. This property is seen in Figure 3.1, and the decreasing magnitude of the electric field can be calculated with Eq.8. It is seen from Eq.8 that when the r distance increases, the

magnitude of the electric field vector is decreasing also.

$$\overrightarrow{E}(r) = \frac{1}{4\pi\varepsilon_0}\frac{Q}{r^2}\vec{r} \tag{8}$$

If the net positive charge at the sphere is increasing, the electric flux and the magnitude of the electric field vector also increases. This case obeys the Poisson's Equation, Eq.7 and a comparison or an experiment can be made to see the physical inside of this situation, as a thought experiment.

Let say that at the first stage there are 21 ions and 20 electrons in the unit volume of the sphere resulting in net charge of 1 C. The net charge is increased to 20 C by putting away 19 electrons somehow. The results of the electric field distribution can be summarized in Figure 3.2.

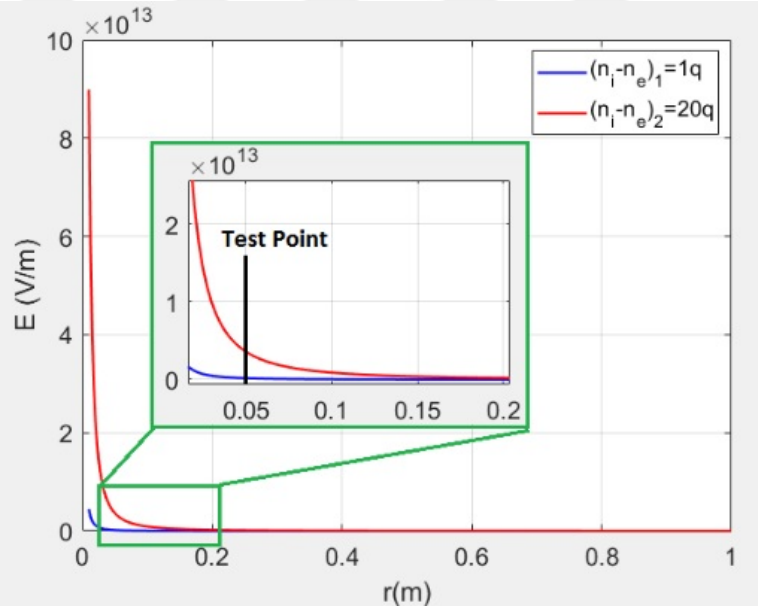

Figure 3.2: Electric field distribution for two different charge sources.

When the two cases are compared, at the test point, it is seen that, the electric field goes to zero for 1 C net charge when r equals to 0.05 meter. On the other hand, the 20 C net charge produces larger electric field and it goes to zero more at a larger distance than 0.05 meter. For the second cases it can be said that with increasing positive charge density the electric field can penetrate larger distance throughts the space.

For the plasma, similar cases can be created with additional features. When the

plasma is in quasi-neutral state, if we disturb its properties, we should look at to see what happens when the local charge imbalance emerges. When a positive charged metal ball is immersed into the plasma, ball pulls the plasma electrons to the surface. This situation of changing net charge density is compared,to the penetration of the electric field is seen in Figure 3.2 for two different cases. It is seen that when the net charge decreases, the electric field penetration distance also decreases in the plasma. The positive electric force of the charged metal ball causes this accumulation.

In the unit volume when the density of the electrons decreases, the net positive charge increases and therefore the penetration of the electric field increases, and at a certain point the electric field and electric potential goes to zero. At that point the net charge is zero and the plasma is in quasi-neutral state again.

The increasing or decreasing number of the electrons is calculated with Eq.9 which is the Boltzman equation.

$$n_e = n_0 e^{e\phi/kT_e} \tag{9}$$

where n_0 is the electron number density at the bulk plasma and k is the Boltzmann constant, e is the unit charge and ϕ is the plasma potential. When inserting of the Eq.9 into Eq.7, Eq.10 is obtained.

$$\overrightarrow{\nabla}.\overrightarrow{E} = \frac{1}{\varepsilon_0}(n_i - n_0^{e\phi/kT_e}) \tag{10}$$

With respect to Eq.10, when the charge of the metal ball is increased, the electric potential also increases and as a result the surrounding electron number density around the metal ball increases respectly (Eq.9). At the same time, when the thermal kinetic energy of the electrons decreases, the electron number density increases as shown in Eq.9.

The relation between the electric field and the electric potential is given by Eq.11.

$$\overrightarrow{E} = -\overrightarrow{\nabla}\phi \tag{11}$$

After substituting of Eq.11 into Eq.10, Eq.12 is obtained which is a different form of the Poisson's equation,

$$\nabla^2\phi = -\frac{1}{\varepsilon_0}(n_i - n_0^{e\phi/kT_e}) \tag{12}$$

After solving Eq.12, the potential distribution function is obtained in Eq.13.

$$\phi(x) = \phi_0 exp(-|x|/\frac{\varepsilon_0 kT_e}{n_e e^2}) \tag{13}$$

Whether the electric flux increases or decreases in the unit volume of the sphere, there is a point which defines as the Debye Length. At this point quasi-neutrality is sustained that the number of the ions and electrons are equal and the electric field and electric potential are zero there.

The Debye length is calculated with Eq.14.

$$\lambda_D = \sqrt{\frac{\varepsilon_0 kT_e}{n_e e^2}} \tag{14}$$

where ε_0 is the permeability of the free space, k is the Boltzmann constant , and e is the unit electric charge, T_e is the electron temperature and n_e is the electron number density.

It is seen from Eq.14 that an increment of the electron density results with decreasing of the Debye length. At the same time increasing the electron temperature results in increasing the Debye length. The potential distribution which the metal ball produces is seen in Figure 3.3.

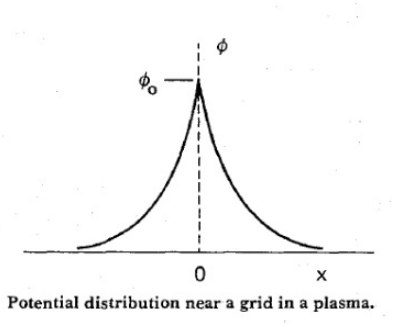

Potential distribution near a grid in a plasma.

Figure 3.3: The electric potential distribution around positive test charge when immersed into the plasma [6].

The useful forms of Eq.14 are shown in Eq.17 from reference [6]. The calculation of the first constant of Eq.17 is presented in Eqn.15.

$$\begin{aligned} k_1 &= 1.38065 \times 10^{23} J/K \\ \varepsilon_0 &= 8.85 \times 10^{-12} F/m \\ e &= 1.6 \times 10^{-19} C \\ constant_1 &= \sqrt{\frac{\varepsilon_0 k_1}{e^2}} = 69 \end{aligned} \tag{15}$$

The calculation of the second constant in Eq.17 is presented in Eq.16.

$$\begin{aligned} k_2 = k_1/e &= 8.6291 \times 10^{-5} eV/K \\ constant_2 &= \sqrt{\frac{\varepsilon_0}{e}} = 7437 \end{aligned} \tag{16}$$

$$\begin{aligned} \lambda_D &= 69\,(T_e/n)^{1/2} \qquad [m],\ T_e\ in\ K \\ \lambda_D &= 7437\,(k_2 T_e/n)^{1/2} \qquad [m],\ k_2 T_e\ in\ eV,\ T_e\ in\ K \end{aligned} \tag{17}$$

If the dimensions "L" of a system are much larger than λ_D, then whenever local concentration of the charges emerge or external potentials take place in the system,

the electric potentials of these ingredients are shielded out in a short distance with respect to the dimension of the system. After the distance of the Debye Length, the electric potential would damp and the electric field cannot penetrate to the bulk plasma [6]. The dependency of the electric potential to the space charge density is given with Eq.12 from reference [6].

The number of the ions or electrons within the sphere whose radius is Debye lenght can be calculated in Eq.18.

$$N_D = n\frac{4}{3}\pi\lambda_D^3 = 1.38 \times 10^6 T_e^{3/2}/n^{1/2} \qquad (T_e \; in \; K) \tag{18}$$

When the condition of $\lambda_D \ll L$ is realized with Eq.19.

$$N_D \lll 1 \tag{19}$$

3.2.1 Criteria for the Plasma

Two conditions have been previously given for an ionized gas to satisfy as a plasma in the previous section. The third condition is about collisions. If the charged particles collide with neutral atoms so frequently their motion is controlled by ordinary hydrodynamic forces rather than by electromagnetic forces. Such a situation is encountered in a jet exhaust. Let say ω is the typical plasma oscillation frequency and let say τ is the residence or reaction time for the collisions. When ω is high, τ should be low enough and vice versa.

In conclusion, a plasma system should satisfy Eq.20 from reference [6].

$$\lambda_D \ll L \tag{20a}$$

$$N_D \lll 1 \tag{20b}$$

$$\omega\tau > 1 \tag{20c}$$

3.3 Plasma Sheaths

The sharp interface between the bulk plasma and the chamber walls or electrodes which have a voltage is called as the plasma sheath. Sheaths are important in plasma physics and engineering because they are used in various areas from semiconductor manufacturing to space propulsion. The sheath is primarily formed at the surface of the plasma and the net charge gradient takes place in there. ϕ_p is called as the plasma potential and it is the potential of the bulk plasma. It will permanently be more positive than the system walls. With the minority of the electrons in that region the light emission decreases and the dark region appears in here. The formation of the plasma sheath is a non-linear problem which is separated into three regions as shown in Figure 3.4.

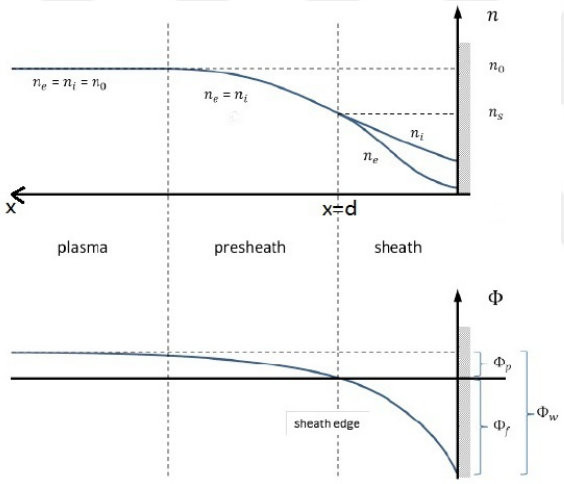

Figure 3.4: Plasma Potential and Particle Number Density Variation in the Plasma Sheath [7].

The plasma in the Figure 3.4 exists in the region $x > 0$ and it is in touch with a wall at $x = 0$ location. The sheath, which has a width of d, is a region that the ion density suppressed the electron density and this mechanism induce a local positive space charge density at that region. At the sheath region or at the Debye sheath, there is a potential drop from bulk plasma to the system wall. This drop produces an electric field. Due to this E-field, the ions are accelerated towards to the wall while the electrons are pushed towards the opposite side where the bulk plasma exists.

Another type of the sheath is known as the Child-Langmuir sheath. When the potential drop between the bulk plasma and the system is very high with respect to the electron temperature, negligible electron flux exists and there are only ions there. Sheaths of this type are named as Child-Langmuir sheaths [19, 51].

The sheath problem including the self-consistent solution for the electron density, ion density, plasma potential and ion velocity is applicable for low pressure plasma and in this case the non-collision assumption is valid in the region $x > d$.

Sheaths are specifically important in the areas of space electric propulsion and material processing. Since their characteristics define the acceleration of the ions that produce the thrust in propulsion technology and how charged particles from plasma interact with the processed surface is important in the semiconductor manufacturing. Specially, the kinetic energy and directions of the ions approaching the outlet of the plasma thruster, in other words to the sheath or grids, determine the amount of the propulsive power of the thruster. At the same time while ions are striking to the substrate, the process parameters are described by the physics of the sheaths in material processing technology. There may be a huge amount of electric potential drop which is tens to hundred volts and which gives tens to hundred electron volts of kinetic energy to the ions at the sheaths. This ion kinetic energy or the velocity create the propulsive power which moves the spacecraft. At the same time ion energies lead to sputtering and chemical activation of surfaces in contact with the plasma in the branch of the material processing.

3.4 Plasma Oscillations

- Plasma Frequency:

Waves are repetitive motions in a continuous medium. In the air, we are accustomed to hear sound waves and we all know that the radio waves from radio and TV's. In water, there are water waves. In a plasma, there are electromagnetic waves and also for each species two kinds of sound waves exist such as ion acoustic waves. For sure, if the plasma is partially ionized, the neutrals are able to have their own sound waves as well. Plasma waves or plasma oscillations happen in the electron

fluid medium. A very high characteristic frequency usually appears in there with a microwave range spectrum. If we imagine that a bundle of electrons are dislocated form their original position, they cause to left behind a chunk of positively charged ions. When the charge neutrality is broken down, the electric field emerges and it pulls these electrons to their original positions back to the ions. In the absence of the collisions, these electrons move forward from ions due to their thermal energy and the process will repeat with the pulling of them by ions left behind, and the electrons continue to oscillate back and forth, such as a mass-spring system or like a simple pendulum. The ions cannot move that time scale because the movement of the electrons is so fast and the ions can be thought as stationary due to their higher mass and inertia compared to that of the electrons. A simple illustration of this situation is shown in Figure 3.5. In this Figure, gray rectangles represent the ions whereas the yellow ones represent the electrons.

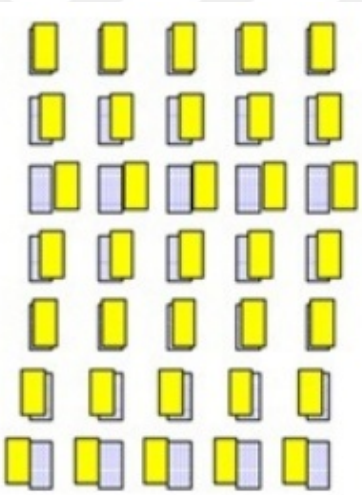

Figure 3.5: A Plasma Oscillation: Dislocated Electrons Oscillate Around Approximately Stationary Ions [8].

The frequency of this oscillation, represented by ω_p, is given by Eq.21, from the reference [8].

$$\omega_p = \left(\frac{n_e e^2}{\varepsilon_o m}\right)^{1/2} \quad (rad/s) \tag{21}$$

where n_e is the electron number density in units of m^{-3}, m is the mass of the electron in kg. The plasma oscillation frequency in terms of plasma electron number density

is written as Eq.22 from reference [6].

$$f_p = 8.9\sqrt{n_e}, \quad n_e[m^{-3}], \quad f_p[Hz] \tag{22}$$

where f_p is the plasma frequency.

CHAPTER 4

VALIDATION AND BENCHMARKING OF COMSOL FOR A 2D AXISYMMETRIC INDUCTIVELY COUPLED ARGON PLASMA MODEL

The numerical simulations of low-pressure radio frequency (RF) inductively coupled Argon discharge are carried out by using the finite element method (FEM) based on COMSOL© Multiphysics software. Two-dimensional axisymmetric ICP model is used to compute the axial and the radial profiles of the electron density (n_e), the electron temperature (T_e), and the plasma potential (V_p). The axial analyses are obtained at two different gas pressures 30 and 40 mTorr for a fixed radial position, $r = 10$ cm and $P = 300$ W. While the radial measurements are done at $P = 200$, 300 and 400 W for a fixed $z = 4$ cm and $p = 30$ mTorr [2].

4.1 System Principles

The RF ion thrusters are composed of three main parts:

- Inductive plasma generator
- Ion accelerator grids
- Electron neutralizer cathode

as seen in Figure 4.1.

For plasma generation, some part of the system boundary is wrapped by N-turn coil, whose one end is directly connected to a RF (13.56 MHz or its harmonics) power supply. This generator applies an oscillating current to the Tesla coils that are responsible

for the magnetic field generation around the ICP plasma. This is resulted in Ohmic (inductive) heating due to interaction of the created species (ions and electrons) in the plasma. In order to transmit full inductive electromagnetic forward power to plasma, an impedance matching network device is used. In this way reflected power from plasma is prevented and a stable plasma generation is sustained. At the same time, there is a connection between the ICP plasma and an ion accelerator with two (or more) grids. The first grid is generally called as screen grid that is responsible for the ion extraction. The other grids are used to accelerate the ions out of the ICP plasma by means of the applied high negative bias voltage with respect to the screen grid. Finally, the third part (hallow cathode) is used for neutralization of the accelerated ion beam [19].

This chapter presents the validation and benchmarking of the self-consistent RF-ICP parametrical (electron density n_e, electron temperature T_e, and plasma potential V_p) simulations that are obtained via COMSOL© Multiphysics software with an experiment [9]. The $2D$ axisymmetric FEM is used for numerical analysis according to the fluid dynamic assumption [2].

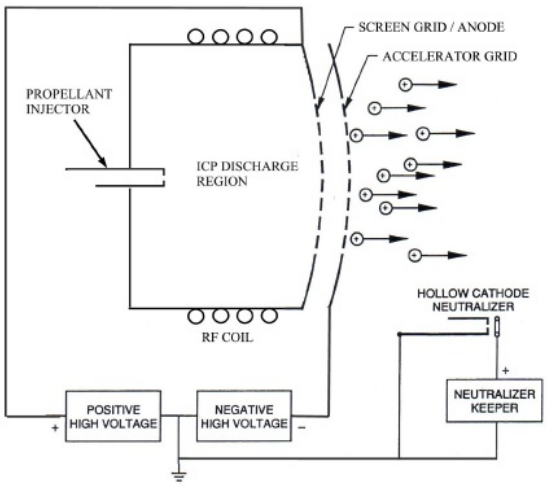

Figure 4.1: The Basic Schematic of Two-Grid RF Ion Engine [5]

4.2 Numerical Method

4.2.1 The COMSOL Model

The computations were run by using the frequency-domain ICP and Magnetic Field interfaces of COMSOL's plasma and AC/DC modules respectively. Two-dimensional ($2D$) axisymmetric finite element method (FEM) was used for numerical analysis. The geometry for the experimental system which is taken from the literature is seen in Figure 4.2 [9]. The simulation geometry of our RF-ICP plasma is clearly presented in Figure 4.3 [2].

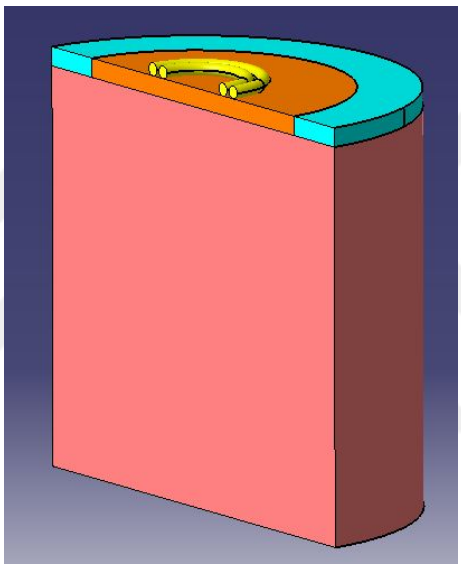

Figure 4.2: The geometry of the experimental set-up

As seen from Figure 4.3, two-turn coils ($\varnothing = 0.95$ cm) are placed onto a quartz window ($\varepsilon_r = 4.2$, $\varnothing_{1/2} = 10$ cm, $t_{thickness} = 1.2$ cm). The coils are surrounded by a domain in order to use finite mesh for the solution of the Ampere's Law. All plasma walls are grounded (0 Volts). The computational domain is filled with 36740 mesh elements that are in general triangular in shape. The final mesh of the geometry and a closer view around the coils are shown in Figure 4.4 [2].

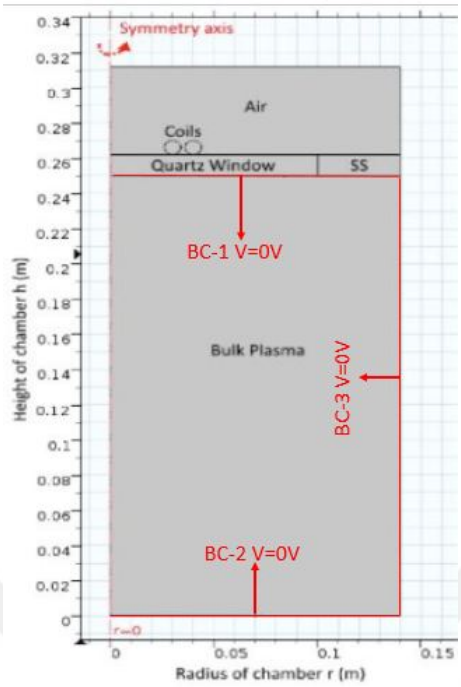

Figure 4.3: Simulation geometry of the RF-ICP plasma [2].

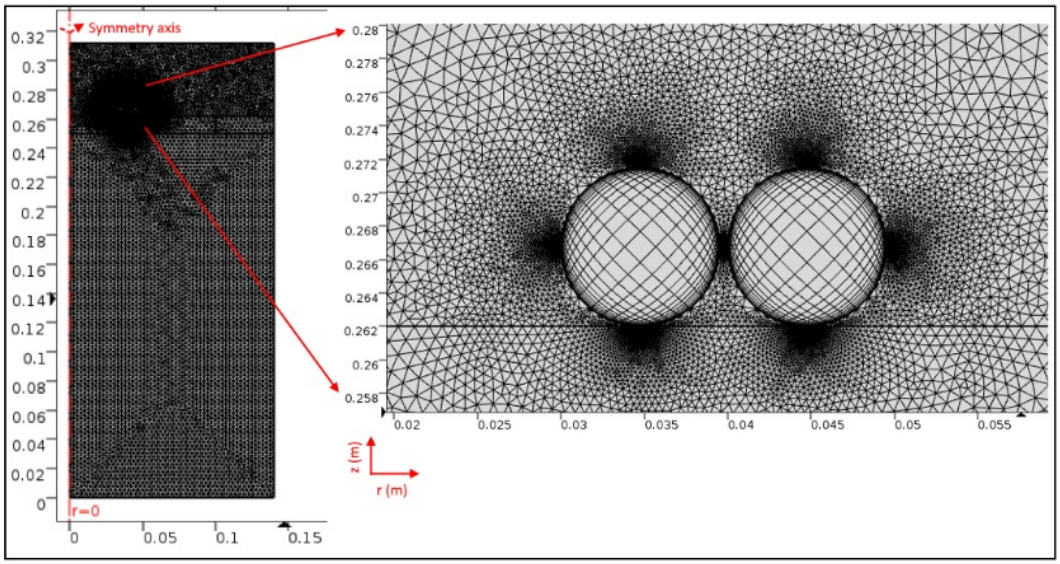

Figure 4.4: Mesh of the RF-ICP plasma [2].

The axial simulations(n_e, T_e, V_p) are run for two different pressures of 30 and 40 mTorr at a fixed RF power of 300 W and a radial distance of 10 cm whereas the radial simulations are run for various RF powers of 200, 300 and 400 W at a fixed gas pressure of 30 mTorr and an axial distance of 4 cm. Each simulation is completed in about 6 minutes 40 s with a processor of 4 GHz-AMD FX(tm)-8350 having Eight-Core with 8 GB-RAM [2]. In the computer solutions the initial time step size is fixed to the 10^{-13} s but further step sizes are also used and the computations are performed with adaptive time stepping technique and the computational system reaches a steady state condition within 0.01 s [2]. The computations are completed with the 111 iterations and computational solution time is 8 minutes, 44 s. The convergence history plot is given in Figure 4.5

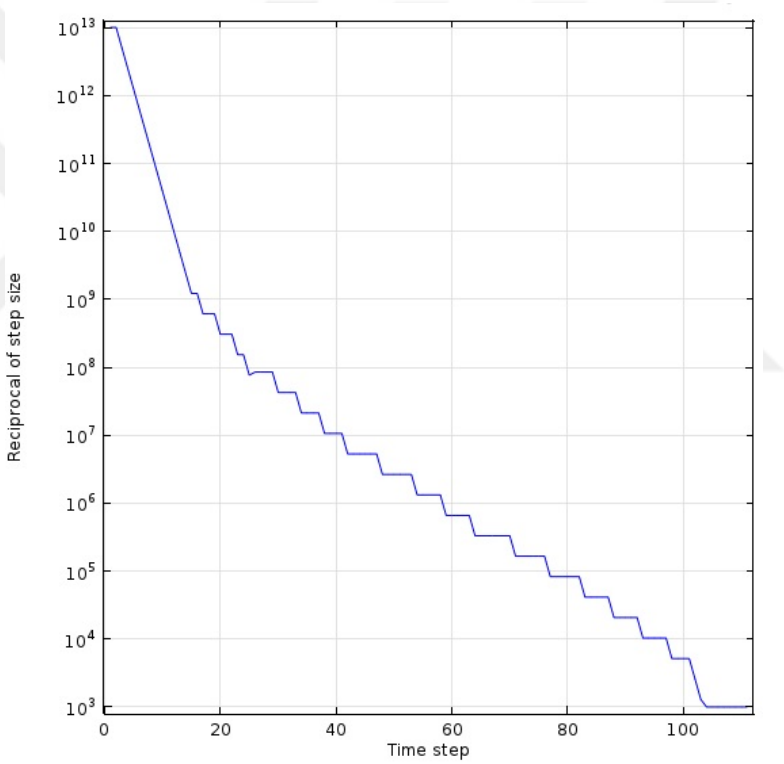

Figure 4.5: Convergence history plot

4.2.2 Theory

The fluid theory used to understand the physical mechanism of high-dense, continuum ICP (magnetized) plasmas is called as the Magneto-hydrodynamics (MHD). In this

theory, the Maxwell's equations are coupled with hydrodynamics. In fact, the origin of these equations is the Vlasov equations. The model equations are discretized with the finite element method (FEM). This numerical method is commonly used for solving the engineering, mathematical and physical problems. Some of the well-known physical problems are heat transfer, fluid flow, structural analysis, mass transport and electromagnetic problems [2].

4.2.2.1 Domain Equations

The COMSOL ICP interface domain equations are mainly described by the Fluid (continuity or drift-diffusion equations) and the electromagnetic (Maxwell's equations) submodels. In fact, there is a strong parametrical relation between these two submodels to get self-consistent solutions. After getting values of electric and magnetic fields from the EM model, these values are used in the Fluid model to calculate the plasma parameters. Then, the plasma conductivity is directly solved from these parameters and they are inserted into the EM model. In this way, these two submodels are coupled to each other [52].

The transport of electrons and the transport of the mean electron energy are described by the following drift-diffusion equations Eq.23 and Eq.24 in 2D axisymmetric domain from references [9, 53–55].

$$\frac{\partial n_e}{\partial t} + \overrightarrow{\nabla}.[-(\mu_e.\overrightarrow{E})n_e - D_e.\overrightarrow{\nabla}n_e] = R_e - (u.\overrightarrow{\nabla})n_e \tag{23}$$

where n_e is the electron density, μ_e is the electron mobility, $\overrightarrow{E}$ is the electric field, D_e is the electron diffusivity, R_e is the electron source coefficient and $(u.\overrightarrow{\nabla})n_e$ is the convective term (neglected for our calculations) from the references [2, 9, 53–55],

$$\frac{\partial n_\varepsilon}{\partial t} + \overrightarrow{\nabla}.[-(\mu_\varepsilon.\overrightarrow{E})n_\varepsilon - D_\varepsilon.\overrightarrow{\nabla}n_\varepsilon] + \overrightarrow{E}.\overrightarrow{\Gamma_e} = R_\varepsilon - (u.\overrightarrow{\nabla})n_\varepsilon \tag{24}$$

where $\overrightarrow{E}.\overrightarrow{\Gamma_e}$ term is the joule (Ohmic) heating, R_ε is the gain or loss of electron energy due to reactions and collisions and $(u.\overrightarrow{\nabla})n_\varepsilon$ is the convective term (neglected for our calculations) from reference [2].

The steady-state electromagnetic fields inside the ICP reactor are calculated from the Maxwell's equations by using the AC/DC module. For a known frequency, the induced currents are obtained by solving the following frequency domain Ampere's law equation from the references [2, 9, 53–55], and the derivation of this equation is completed in Appendix C of the thesis.

$$(j\omega\sigma - \omega^2\varepsilon_0\varepsilon_r)\overrightarrow{A} + \overrightarrow{\nabla} \times (\mu_0^{-1}\mu_r^{-1}\overrightarrow{\nabla} \times \overrightarrow{A}) = \overrightarrow{J_e} \tag{25}$$

$$\overrightarrow{B} = \overrightarrow{\nabla} \times \overrightarrow{A} \tag{26}$$

where j is the imaginary part, ω is the RF angular frequency, σ is the plasma conductivity, ε_0 is the vacuum electric permittivity, ε_r is the relative electric permittivity, μ_0 is the magnetic vacuum permeability, μ_r is the relative magnetic permeability, $\overrightarrow{A}$ is the magnetic vector potential, and $\overrightarrow{B}$ is magnetic field, $\overrightarrow{J_e}$ is the external current applied to the coil. For the electromagnetic model assumption, all the coils are connected in series and they have the same conduction current. In addition, the induced electric field and so the induced current is only in the azimuthal direction (no radial and vertical parts). Therefore, the input power can be written from Eq.27, from references [2, 9, 53–55]

$$P_{ind} = \frac{1}{2}Real(E_\phi . J_{e\phi}) \tag{27}$$

where E_ϕ is the azimuthal component of the induced electric field, $J_{e\phi}$ is the azimuthal component of the induced current. Note that, the displacement current is neglected due to being very small as compared to the induced current [2].

4.2.2.2 Boundary and Initial Conditions

The number of electrons in the plasma decreases by loss due to reactor wall interaction but at the same time, it increases with the secondary electron generation in the plasma. Therefore, the general electron and energy flux equations can be shown in

Eq.28 and Eq.29 from reference [54, 56].

$$\overrightarrow{n}\overrightarrow{\Gamma_e} = \frac{1-r_e}{1+r_e}(\frac{1}{2}v_{e,th}n_e) - (\sum \gamma_i(\overrightarrow{\Gamma_i}.\overrightarrow{n}) + \overrightarrow{\Gamma_t}.\overrightarrow{n}) \tag{28}$$

$$\overrightarrow{n}\overrightarrow{\Gamma_\varepsilon} = \frac{1-r_e}{1+r_e}(\frac{5}{6}v_{e,th}n_\varepsilon) - (\sum \gamma_i\varepsilon_i(\overrightarrow{\Gamma_i}.\overrightarrow{n}) + (\varepsilon\overrightarrow{\Gamma_t}.\overrightarrow{n})) \tag{29}$$

For our fluid model calculations, the boundary is the reactor wall. Therefore, we neglect the secondary emission flux terms $\sum \gamma_i(\overrightarrow{\Gamma_i}.\overrightarrow{n})$, and $\sum \gamma_i\varepsilon_i(\overrightarrow{\Gamma_i}.\overrightarrow{n})$. In addition, we assume that the thermal emission flux term $(\overrightarrow{\Gamma_t}.\overrightarrow{n})$ is also zero. After setting the reflection coefficient r_e to 0.2, both boundary equations turn into Eq.30 and Eq.31, from references [2, 54, 56].

$$\overrightarrow{n}.\overrightarrow{\Gamma_e} = \frac{1}{3}v_{e,th}n_e \tag{30}$$

$$\overrightarrow{n}.\overrightarrow{\Gamma_\varepsilon} = \frac{5}{9}v_{e,th}n_\varepsilon \tag{31}$$

where $\overrightarrow{n}$ is the normal vector to the surface and $v_{e,th}$ is the electron thermal velocity.

Selection of initial conditions effects significantly the verification of the used model. In any case, the first important initial condition is setting the voltage, V to "0" at $t = 0$ in order to satisfy the Poisson's equation. The second one is setting the initial values of all magnetic vector potentials (axial, radial and azimuthal) to zero. For our calculations; driving RF frequency is set to 13.56 MHz, excitation inert gas is Argon, initial electron density is taken as ($n_{e,0}$) is $1 \times 10^{15}\ m^{-3}$, initial mean energy (ε_0) is uniform and equals to 5 Volts, initial reduced electron mobility (μ_{en}) is $4 \times 10^{24}\ m^{-1}V^{-1}s^{-1}$ and the gas temperature is 300 K.

4.2.2.3 Plasma Chemistry

Table 4.1: Modeled chemical reaction set in the ICP Argon discharge [2].

No.	Process	Reaction	$\Delta\varepsilon$ (eV)
1	Elastic collision	$Ar + e \rightarrow Ar + e$	
2	Ground state excitation	$Ar + e \rightarrow Ar^* + e$	11.5
3	Ground state ionization	$Ar + e \rightarrow Ar^+ + 2e$	15.8
4	Step-Wise ionization	$Ar^* + e \rightarrow Ar^+ + 2e$	4.24
5	Superelastic collisions	$Ar^* + e \rightarrow Ar + e$	-11.5
6	Metastable pooling	$Ar^* + Ar^* \rightarrow Ar^+ + Ar + e$	
7	Two-Body quenching	$Ar + Ar^* \rightarrow Ar + Ar$	

It is in fact rather hard to understand and explain the physical principles of inductively coupled plasma systems. Therefore, the simple and well-known Ar plasma chemical reaction mechanisms are preferred for this chapter [2].

The Argon plasma is generated and sustained in an ICP plasma reactor. With the plasma ignition by RF generator, the electrons, radicals and ions are created in time. In this way, the plasma medium becomes conductive. The created species mainly depend on RF frequency, gas flow and heating phenomena in the plasma. For our modeling, we only concentrated on the interaction between four species; e (electron), Ar (neutral), Ar^* (excited) and Ar^+ (singly-ionized) as given in references [2, 9, 54, 56].

4.2.2.4 The Experimental Setup

The experimental set-up used for the generation of the plasma is shown in Figure 4.6. This same set-up is also used for simulations in the COMSOL code. The experimental values obtained for the plasma are then compared with those of the simulations. The comparisons of the experimental and the simulated results are then used to validate and verify the both of the results obtained. In a way, a cross-check of the results are made and the present research performed on plasma physics is strongly validated. Therefore, this section is intended to describe the appropriate experimental conditions to validate and benchmark our COMSOL ICP plasma module [2].

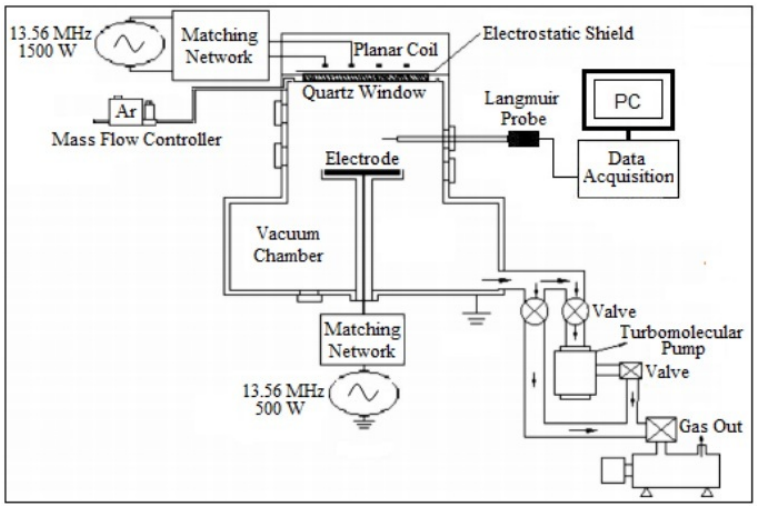

Figure 4.6: Schematic View of the Planar-Type ICP RF Plasma System used for the Experimental Analysis [9]

A detailed sketch of the RF inductively coupled plasma system is shown in Figure 4.6. As seen from Figure 4.6, the shape of the plasma system seems like an inverse "T" letter. From the geometry of the plasma system it can be decided that the system can be devided into two upper ($|$) and lower ($-$) parts. The dimensions of the upper part are 28 cm in diameter and 25 cm in length. There is a quartz window ($\varnothing = 20$ cm with thickness 1.2 cm) on the top of the upper part. Two-turn planar coupling coil ($\varnothing = 8$ cm and $\varnothing = 6$ cm) is put into a copper tube (for chilling) is attached to the outer surface of the quartz window. A 1500 W , 13.56 MHz, RF source with its matching network system is connected to the coil. Volume ($\varnothing = 30$ cm, $h = 21$ cm) of the lower part is a bit smaller than that of the upper part. A Teflon isolated aluminum electrode is welded to the bottom of the lower part. The electrode is connected to another grounded 500 W, 13.56 MHz RF source to ignite the plasma. For diagnostic analysis, a commercial $(HidenProbe, HidenAnalytical, Ltd.)$ Langmuir probe is inserted into the plasma at a distance of 4 cm fixed distance away from the upper part for radial parametrical analysis, at 10 cm fixed distance away from the central axis of the plasma for axial variational analysis. The probe tip is a tungsten wire, whose diameter is 0.2 mm and length is 10 mm. A mass flow controller unit controls the amount of Argon gas injected into the plasma [2].

4.2.2.5 Results and Discussion

Figure 4.7-4.11, presents the experimental and simulated axial distributions of RF-ICP plasma parameters (n_e, T_e and V_p) at a radial distance of 10 cm and 300 W RF coil power under two different (30 and 40) mTorr gas pressures [2].

The evolution of axial electron density is shown in Figure 4.7. and is observed that the simulated results almost match up with the experimental results. A similar increase in the density is observed with the gas pressure in both cases due to high collision rate. According to the measured data, the electron density is nearly constant in the bulk plasma region at the system center and it decreases toward the sheath regions that are closer to the top and the bottom walls. The numerical results show that up to $z = 12$ cm region the distribution becomes practically constant.

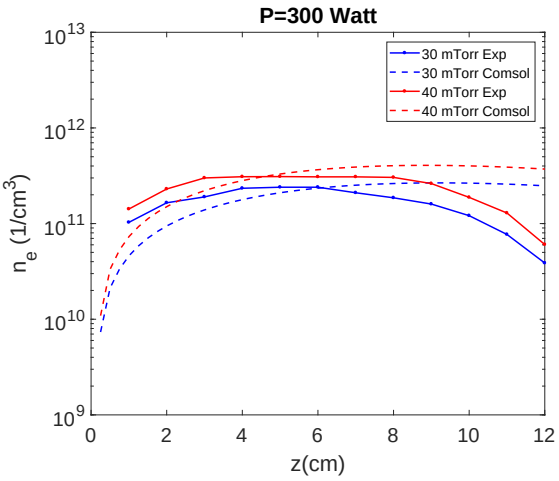

Figure 4.7: The axial distribution of the electron density for both simulated and experimental results operated for 30 and 40 mTorr at $r = 10$ cm and $P = 300$ W [2].

The numerical simulations cover the whole z-domain as seen in Figure 4.8. It is seen that both species have almost the same profile (quasi-neutrality) except towards the boundaries and the density decreases towards the bottom sheath region. The ion density on the right boundary (bottom of the chamber-cathode) is almost 10 times greater than the electron density due to the ion shielding while the electron density is 1.3 times greater than that of the ion density on the left boundary (quartz window-anode) due to the electron shielding [2]. The reason for decreasing density through the bottom boundary is due to the ion shielding effects [2].

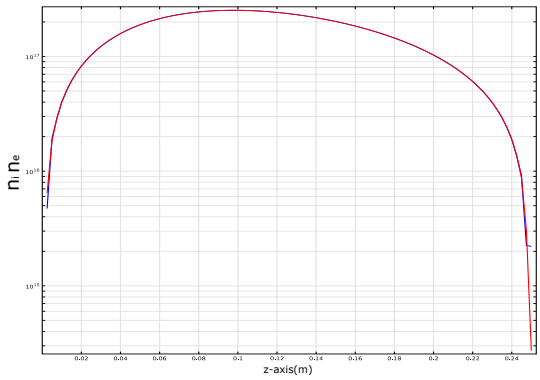

Figure 4.8: The extended axial distribution of n_i-blue line and n_e-red line for the simulated results operated for 30 mTorr at $r = 10$ cm and $P = 300$ W. The units are in cm^{-3} [2].

Figure 4.9 shows the axial profiles of simulated and measured electron temperature of RF inductively coupled discharges under the same operating conditions (30 and 40 mTorr, 300 W).

The values of the simulated temperatures are lower than that of the experimental results. The measured data reveals that the temperatures decrease gradually toward the sheath regions due to decreasing azimuthal electric field (or induced power) and has one peak of the value in the bulk plasma region where the E-field is higher due to the higher inductive power density at the unit volume. Also, results decrease with the gas pressure. When the electron particle number increases, the kinetic energy per unit electron would decrease and the electron temperature would decrease as well. Additionally, both the simulated and experimental temperatures decrease through the bottom boundary. When looking at the differences between the experimental and simulation results, it is observed that although the trends are different, the magnitudes of results are similar.

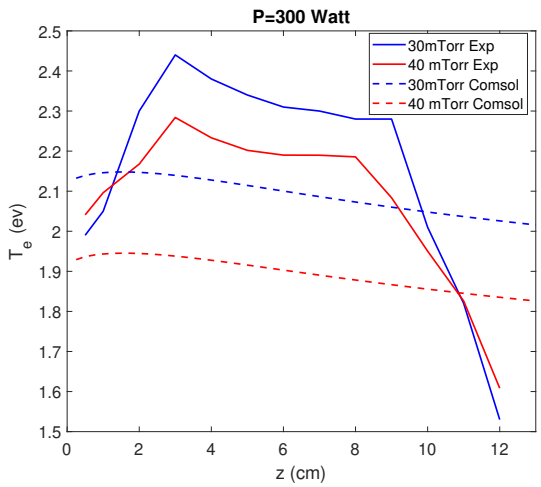

Figure 4.9: The axial distribution of the electron temperature for the results operated in 30 and 40 mTorr at $r = 10$ cm and $P = 300$ W [2].

The comparison of the plasma potential variation along the axial distance is shown in Figure 4.10. All the profiles are very similar to the profiles of the electron density results. However, the experimental potential values are higher than the calculated potentials. Almost no change is observed with gas pressure. By covering the whole z-domain as seen in Figure 4.11, the simulated potential drops (0 Volts) in the sheath region is clearly observed. As mentioned before, the reason of these further drops is low diffusion and drift electron velocities in the simulated data. Moreover, the simulated results are almost 4V lower than the measured values.

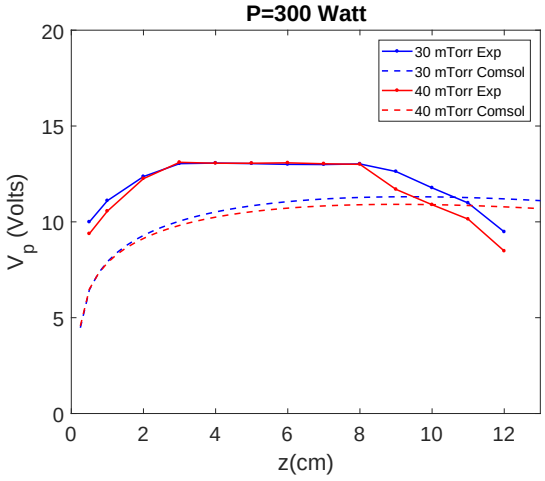

Figure 4.10: The axial distribution of the plasma potential for both simulated and experimental results operated for 30 and 40 mTorr at $r = 10$ cm and $P = 300$ W [2].

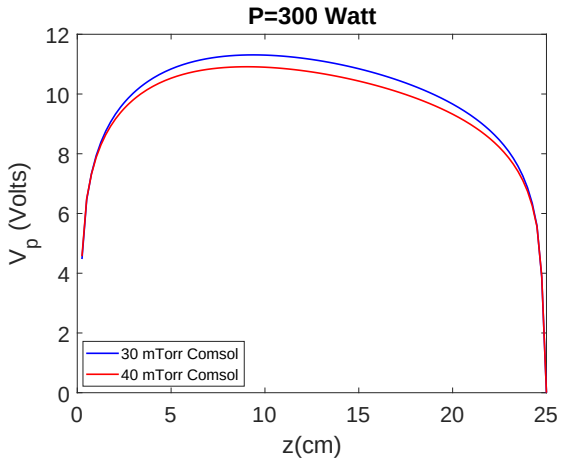

Figure 4.11: The extended axial distribution of the plasma potential of the simulated results operated for 30 and 40 mTorr at $r = 10$ cm and $P = 300$ W [2].

The radial distribution of the plasma parameters (n_e, T_e, V_p) for three different RF powers; 200, 300, 400 W at $z = 4$ cm and $p = 30$ mTorr are presented in Figures 4.12 - 4.14. From Figure 4.12, both calculated and measured electron density profiles decrease with the radial distance and they are almost the same except 200 W. [2].

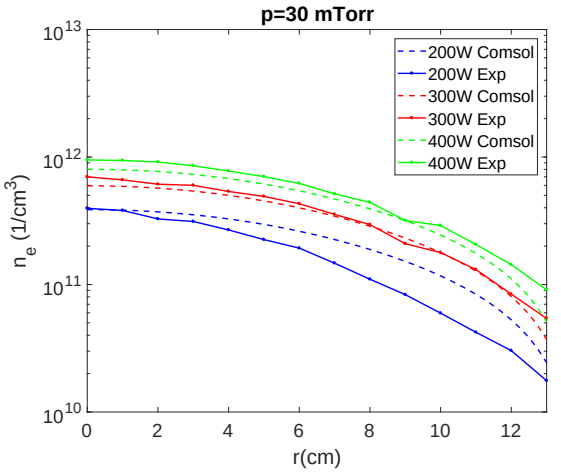

Figure 4.12: The radial distribution of the electron density for both results operated for 200, 300 and 400 W at $z = 4$ cm and $p = 30$ mTorr [2].

From Figure 4.13, the numerical electron temperatures are lower than that of the experimental measurements. In fact, their radial profiles are almost similar. Both decreases with the radial distance and they get closer to each other toward the right wall of the system. There is no RF power effect on the calculated electron temperatures whereas the temperature increases with RF power according to the experimental re-

sults. There is almost 1.2 eV difference between the numerical and the experimental values and it decreases gradually with the radial distance [2].

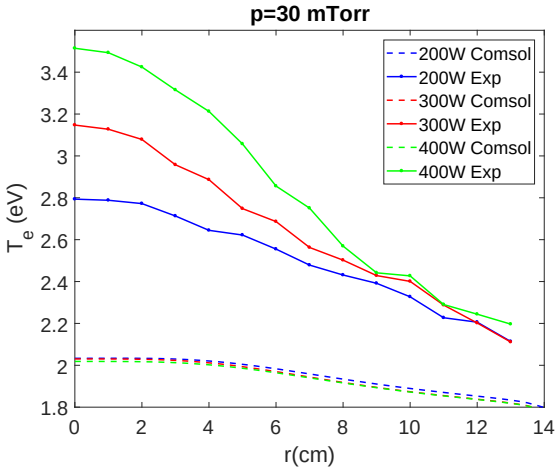

Figure 4.13: The radial distribution of the electron temperature for both results operated for 200, 300 and 400 Watt at $z = 4$ cm and $p = 30$ mTorr [2].

From Figure 4.14, it can be observed that both results have similar plasma potential profile curves for all RF powers under the same gas pressure (30 mTorr). As mentioned in the radial temperature analysis, no RF power effect is observed for the numerical results while a slight increase is detected with increasing power. In both cases, the plasma potential decreases towards the side walls. The overall difference between the simulated and the measured results is approximately 4 V [2].

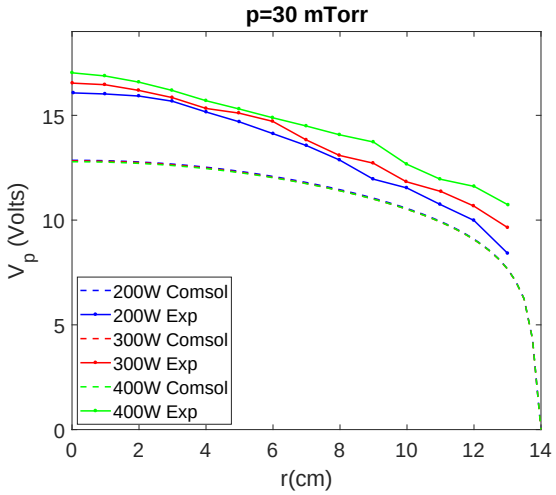

Figure 4.14: The radial distribution of the plasma potential for both simulated and experimental results operated for 200, 300 and 400 W at $z = 4$ cm and $p = 30$ mTorr [2].

In conclusion, 2D axisymmetric fluid and global models are used for simulating the Argon two-coil planar RF-ICP discharges by using the COMSOL software and the results are compared with the experimental results. The axial and radial evolutions of the electron density, the electron temperature and the plasma potential are analyzed by both numerical and experimental methods. In general, the model simulations match up with the measured results. Therefore, the next step is to develop used model for simulating a RF ion thruster [2].

CHAPTER 5

PLASMA CHAMBER SIMULATIONS

In that chapter the used mesh is shown from the Figure 5.1, on the other hand, this mesh is only for when CT equals to 23 and AR equals to 6. The BC1 and BC2 equals to 0 Volts at all sections except the Section 5.2.

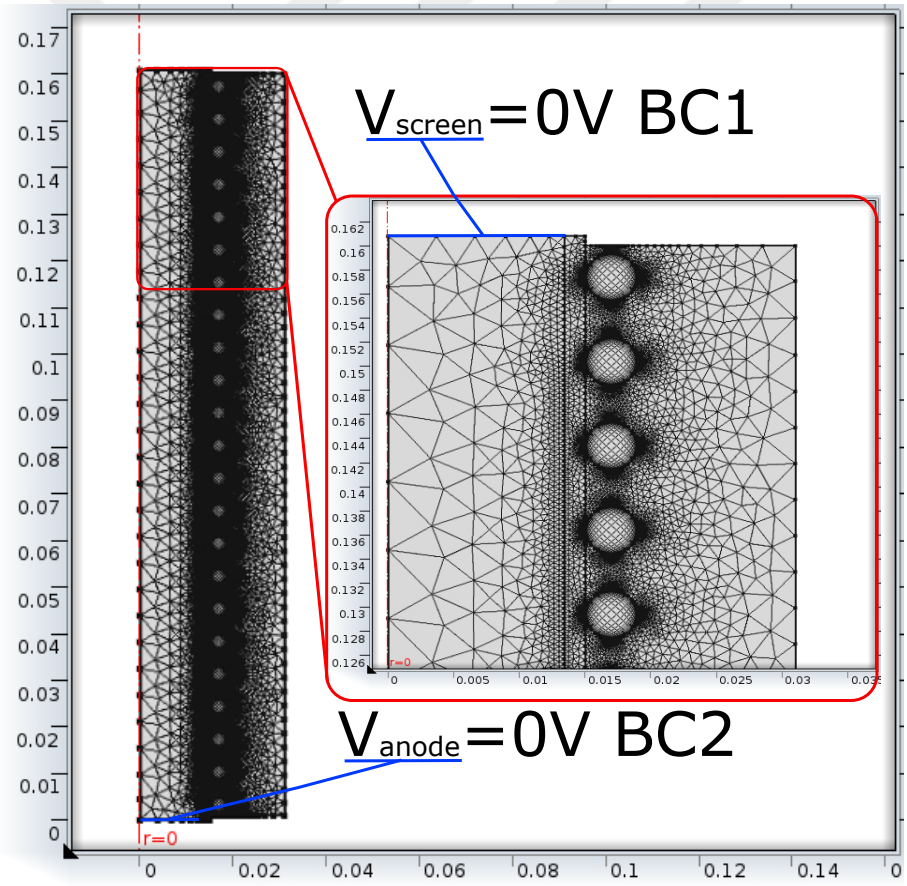

Figure 5.1: The mesh to be used in that Chapter except the Section 5.2

The convergence history plot is given in Figure 5.2. Selection of initial conditions significantly effects the verification of the used model. In any case, the first impor-

tant initial condition is setting the voltage, V to "0" at $t = 0$ in order to satisfy the Poisson's equation. The second one is setting the initial values of all magnetic vector potentials (axial, radial and azimuthal) as zero. For our calculations; driving RF frequency is 13.56 MHz, excitation inert gas is Argon, initial electron density ($n_{e,0}$) is $1 \times 10^{15}\ m^{-3}$, initial mean energy (ε_0) is uniform and equals to 5 Volts, initial reduced electron mobility (μ_{en}) is $4 \times 10^{24}\ m^{-1}V^{-1}s^{-1}$ and the gas temperature is 300 K. The computational system reaches a steady state condition within 0.01 s [2]. In the solutions the initial time step size is fixed to 10^{-13} s but calculations for further steps are performed with adaptive time stepping technique. The computation is completed with the 117 iteration and is performed with a processor of 4 GHz-AMD FX(tm)-8350 having Eight-Core with 8 GB-RAM. The computational domain is filled with 106974 mesh elements that are in general triangular in shape. [2] and computational solution time is 1 minute 21 s.

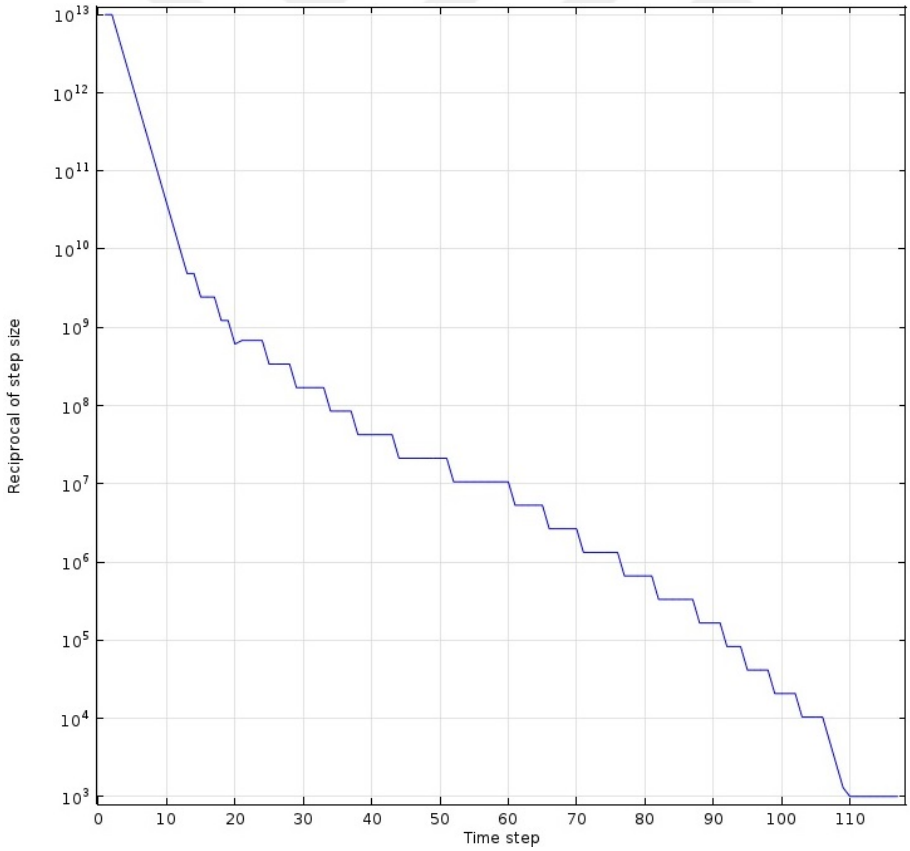

Figure 5.2: Convergence history plot

5.1 The effects of changing the coil turn to the plasma parameters

The effect of changing coil turn number to the electron and ion density is seen from Figures 5.3 and 5.4. 2D density variations of two different chamber configurations are clearly observed in Figures 5.3 and 5.4 with height expression. The hills of the height expression means higher value of n_e, n_i

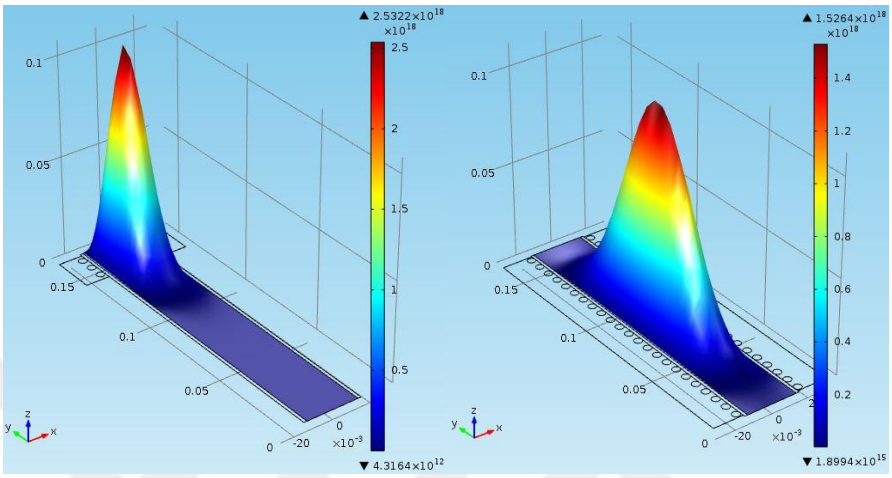

Figure 5.3: The effect of changing the coil turn number on distribution of n_e

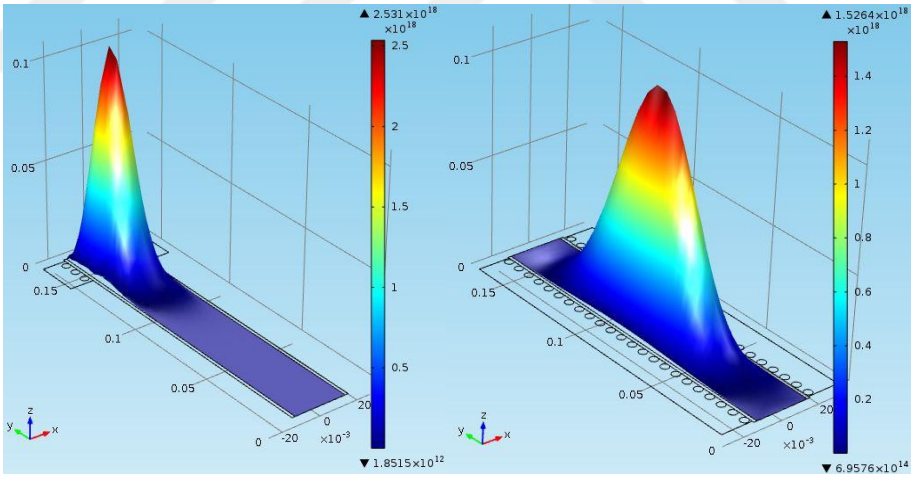

Figure 5.4: The effect of changing the coil turn number on distribution of n_i

In Figures 5.3 and 5.4 the simulation parameters are $P = 300$ W, $p = 40$ mTorr, AR=6, $V_{bound} = 0$ V and the ion-electron density unit is m^{-3}. The left distributions belong to 3-turn coil chamber while the right graphs show the density distributions for 23-coil chamber. As seen from Figures 5.3 and 5.4, the electron and ion densities have maximum values (red) due to the generation of a concentrated plasma column at the RF coils locations. These maximum values tend to decrease with increasing coil

turn numbers. At the same time, the figures on the left side of the Figures 5.3 and 5.4, indicate that the electron and ion density distribution have their highest values over the screen grid and if such density profiles are desired, coil turns should be as low as possible, such as 3 coil turns, and the location of these coils must be placed as close to the screen grid. Therefore, the resulting ion density distribution will have its maximum value at the location of the screen grid for maximum performance thruster.

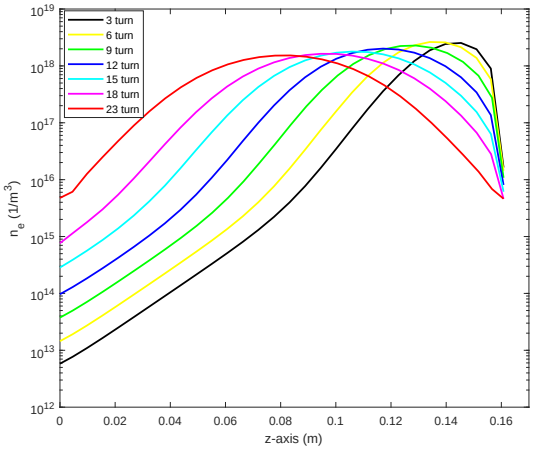

Figure 5.5: The effect of changing coil turn to the electron density n_e at 1D.

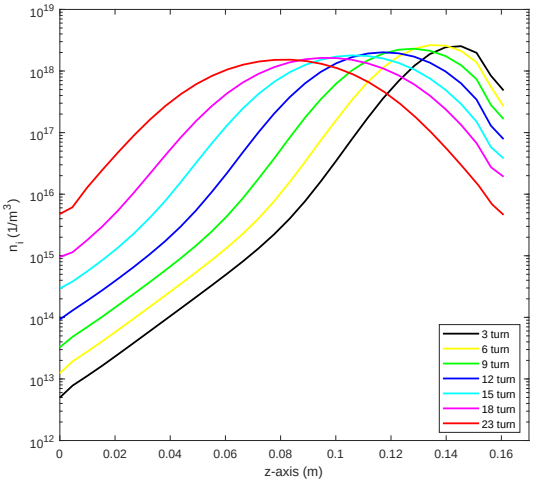

Figure 5.6: The effect of changing coil turn to the electron density n_i at 1D domain.

Figures 5.5 and 5.6 show the evolution of n_e and n_i densities respectively along the z-axis with respect to coil-turn numbers. For Figures 5.5 and 5.6 the simulation parameters are choosen as $P = 300$ W, $p = 40$ mTorr, AR=6, $V_{bound} = 0$ V and unit is m^{-3}. When the coil turn number is increased, the peak value of the densities does not change significantly. With decreasing coil turn number the tail of the density profiles decreases as well, since the region of the tail does not include any RF coil wrap.

Therefore, it can be said that the densities have their maxima at the coil locations. Besides, increasing the coil turn number effects the distribution of the density giving more uniform distributions along the z axis resulting in a density distribution more Gaussian.

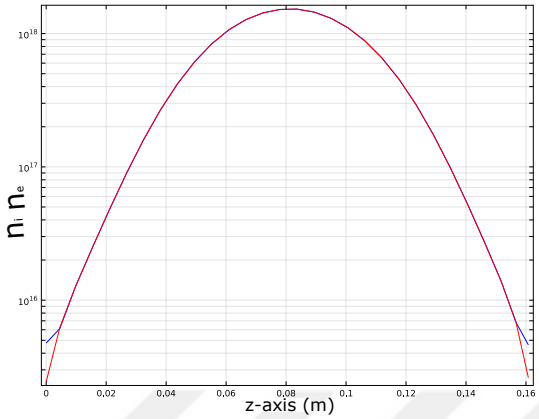

Figure 5.7: The n_e and n_i distribution together.

When the n_i, n_e density distributions along the z-axis for fixed plasma conditions are investigated, a very familiar profile is observed as seen in Figure 5.7. In Figure 5.7 the working parameters are set as $CT = 23$, $P = 300$ W, $p = 40$ mTorr, AR=6, $V_{bound} = 0$ V and unit is m^{-3}. The blue line indicates n_i and the red one n_e distributions. The densities are match due to the quasi-neutrality in the bulk plasma region. There is a slight difference between the electron and ion densities at both sheath regions (left and right). From Figure 5.7, the ion density (blue line) is a bit higher than the electron density (red line) at these sheath regions.

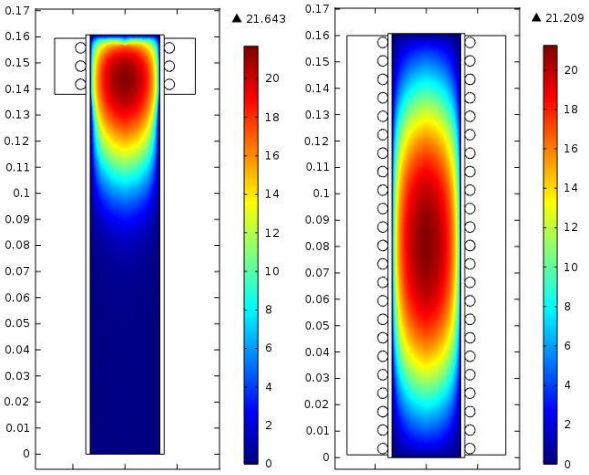

Figure 5.8: The effect of changing coil turn to the V_p at the 2D domain.

Figure 5.8 shows the variation of the plasma potential distribution with respect to coil

turn numbers. It is observed that the potential distribution becomes more uniform with increasing coil turn numbers. For Figure 5.8, the working parameters of the simulations are $P = 300$ W, $p = 40$ mTorr, $V_{bound} = 0$ V , AR=6 and the units is in $Volts$.

For both simulations, the highest value of the potential is observed at the center of the coil region and it decreases toward to the edges. As seen from the left configuration, the plasma potential drops sharply at the screen grid (sheath region). Because the plasma potential depends on the electron temperature and in the sheath region, the electron temperature is very low. In fact, in the sheath region, the electrons are repelled towards the bulk plasma region while the ions take their place in this region.

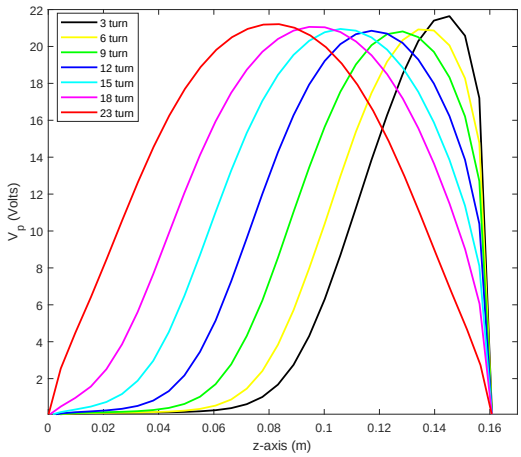

Figure 5.9: The effect of changing coil turn to the V_p at the 1D domain.

As seen in Figure 5.8, it is observed from Figure 5.9 that the plasma potential clearly drops at the screen grid. The working parameters of this simulations are; $P = 300$ W, $p = 40$ mTorr, $V_{bound} = 0$ V, $AR = 6$ and the unit is in Volts. With increasing number coil turns, the potential distribution over the coil regions reaches a peak. The peak values at the center are the same for all configurations and they decrease toward to the sheaths.

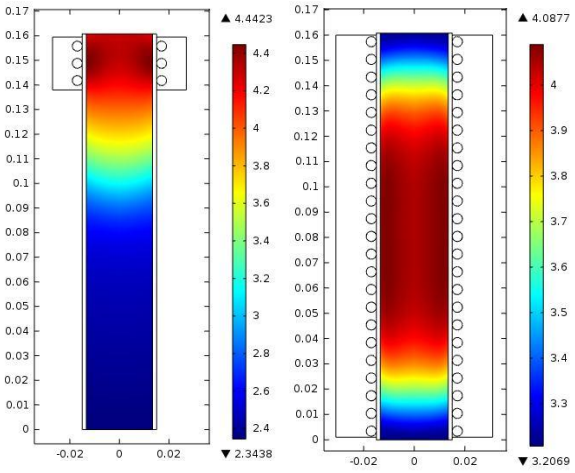

Figure 5.10: The effect of changing coil turn to the T_e at the 2D domain.

For Figure 5.10, the working parameters of the simulations are $P = 300$ W, $p = 40$ mTor, $AR = 6$, $V_{bound} = 0$ V , and the units is in eV. At the left of Figure 5.10 $CT = 3$ and at the right $CT = 23$.

As shown from Figure 5.10, the electron temperature gets its highest value at which the coil is wrapped around. Because, at this area, the electromagnetic energy is generated and this generated energy is absrobed from the plasma due to the coils.

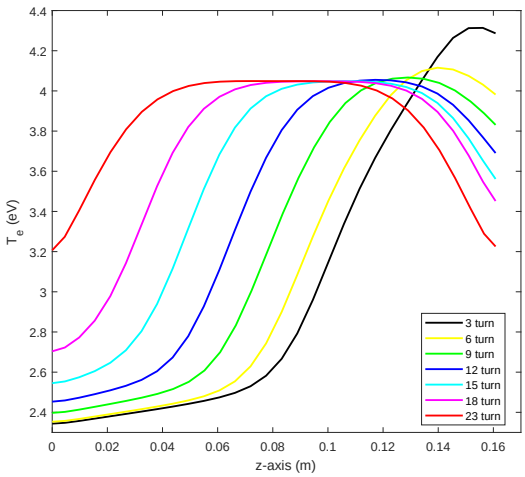

Figure 5.11: The effect of changing coil turn to the T_e at the 1D domain.

When compared to Figures 5.5 and 5.6, similar profile shapes are observed in Figure 5.11. However, the peaks of T_e due to high-turn are smoother in Figure 5.11. The

working parameters of the simulations are $P = 300$ W, $p = 40$ mTorr , $V_{bound} = 0$ V, $AR = 6$ and the unit is in $Volts$

5.2 The effects of changing anode voltage on the plasma parameters.

The screen voltage is fixed to 0 V in order to see Child-Langmuir sheath phenomena at the screen grid for a single aperture system. The anode voltage is increased up to 300 V. Then, distributions of the physical parameters; such as, voltage, electric field, electron and ion densities are investigated. The working parameters of the simulations for this section are $P = 1200$ W, $p = 40$ mTorr, $AR = 6$, $CT = 18$ and the unit is in $Volts$. Figure 5.12 shows 2D distribution of the plasma potential but with height expression distribution. When looked to the variation of the potential in Figure 5.12, the hills represents to higher value of the potential. As seen from Figures 5.12 and 5.13, there is a sharp electric potential drop at the sheath edges which equal to a few Debye lengths. At the bulk plasma, on the other hand, the electric potential distribution is highly uniform due to high numbers of coil turns, which is 18 turns for this case. This orderly distribution of the plasma is seen not only from Figure 5.12 and but also from Figure 5.13

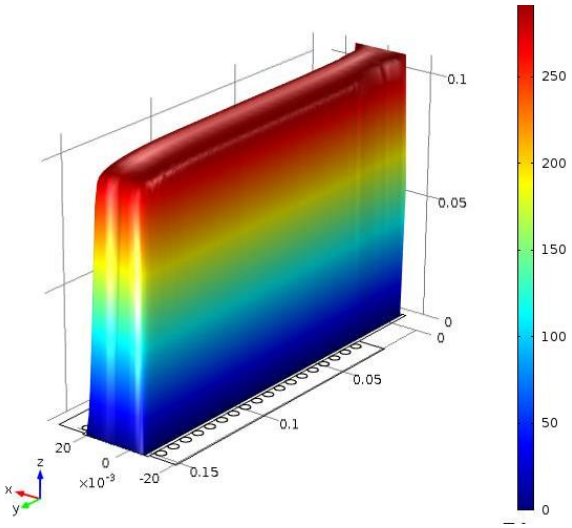

Figure 5.12: The 2D electric potential distributions when anode voltage is 300V.

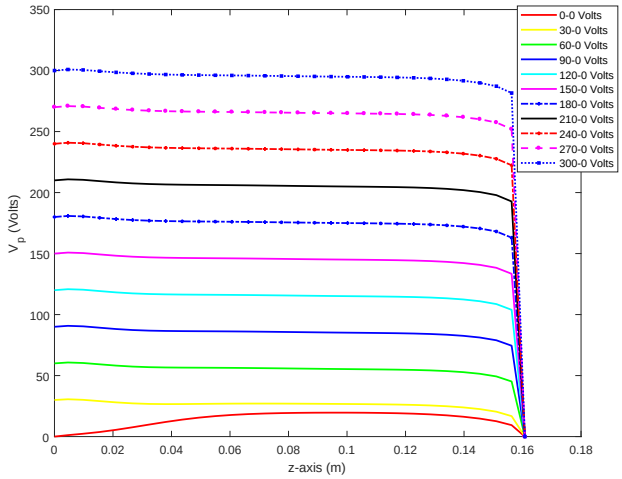

Figure 5.13: The electric potential distributions at 1D for 11 different anode voltage.

From Figure 5.14, the distribution of the electric potential along the walls of the plasma chamber is investigated for a single anode voltage of 300 Volts. The existence of the sheath is seen at the surface of the plasma chamber apparently at the left of Figure 5.14. As clearly seen from Figure 5.14 (right), a sharp decrease (drop) in the value of electric potential at the sheath region is observed.

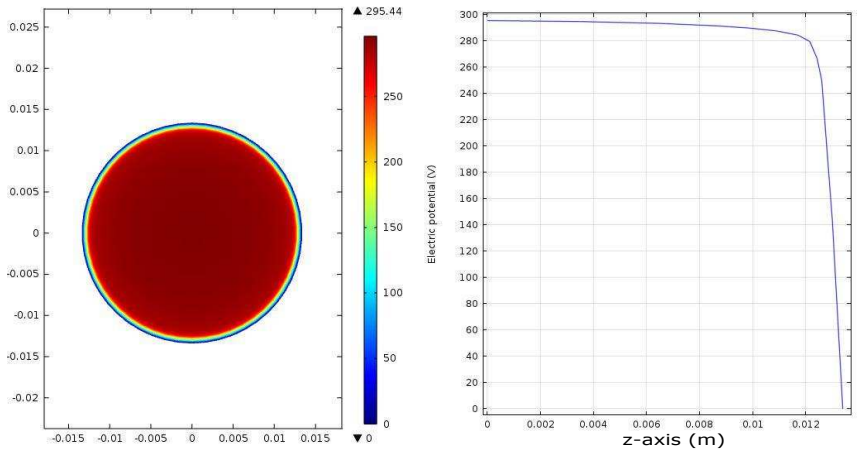

Figure 5.14: The radially varying electric potential distribution $V_{anode} = 300$ V.

From Figures 5.12 and Figure 5.15, there is an inverse relationship between the electric field and the electric potential. There is a sharp electric potential drop at the screen grid, whereas, there is a sharp positive electric field in there as expected in the Child sheath.

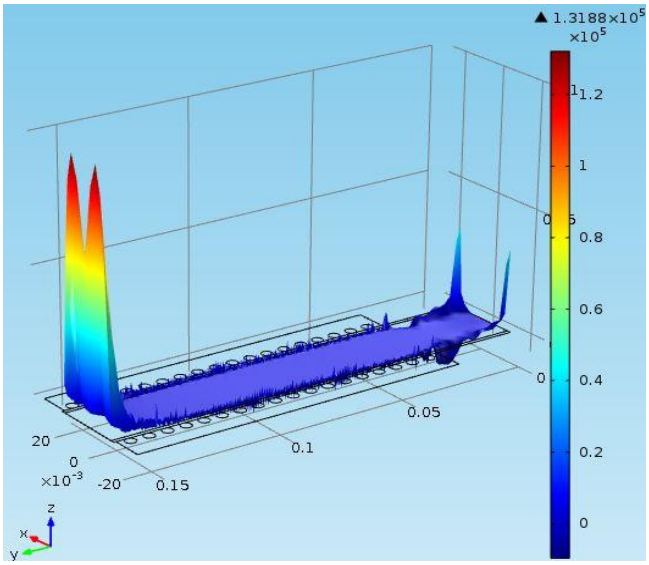

Figure 5.15: The z-component of the electric field, $V_{anode} = 300V$, $V_{sceen} = 0V$

In Figure 5.16, the evolution of electric field at the sheath region with respect to different anode voltages are seen at 1D. With increasing anode voltage, the electric field strength increases as well.

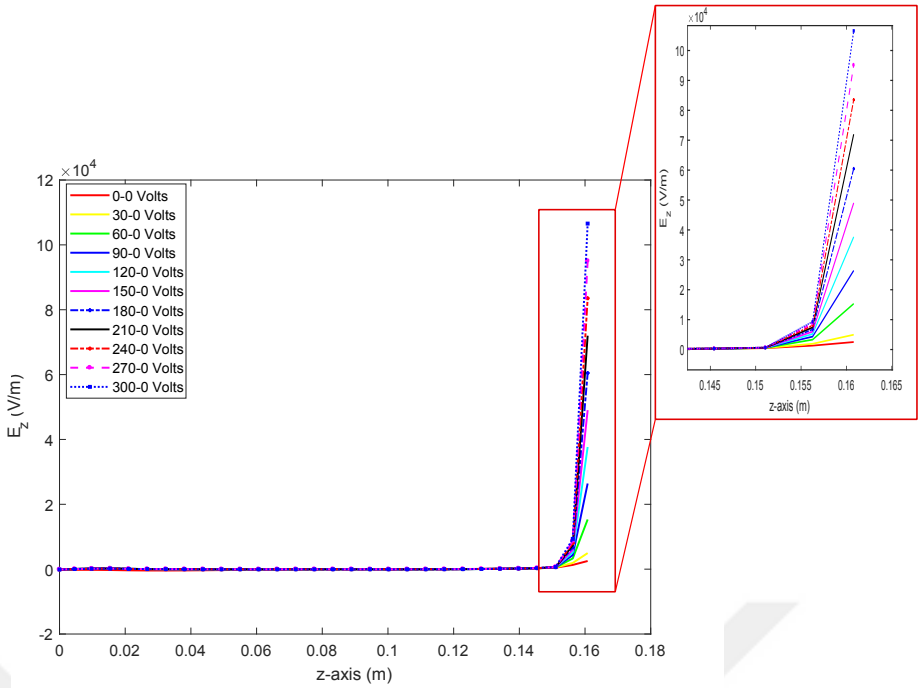

Figure 5.16: The electric field distributions for 11 different anode voltage

The Child Langmuir plasma sheath is seen very clearly from Figures 5.17 and 5.18 at this single aperture system. When anode voltage is 300 V at the maximum level, the electron density is nearly zero at the sheath edge as stated by the Child sheaths due to the high positive electric field in that region. It is seen from Figure 5.17 that the ion density is decreasing slightly with increasing anode voltage. On the other hand, although there is a slight decrease in the ion density, the order of the ion densities is about $10^{17}\ m^{-3}$ at the screen grid and it is a very high value when compared to the electron densities.

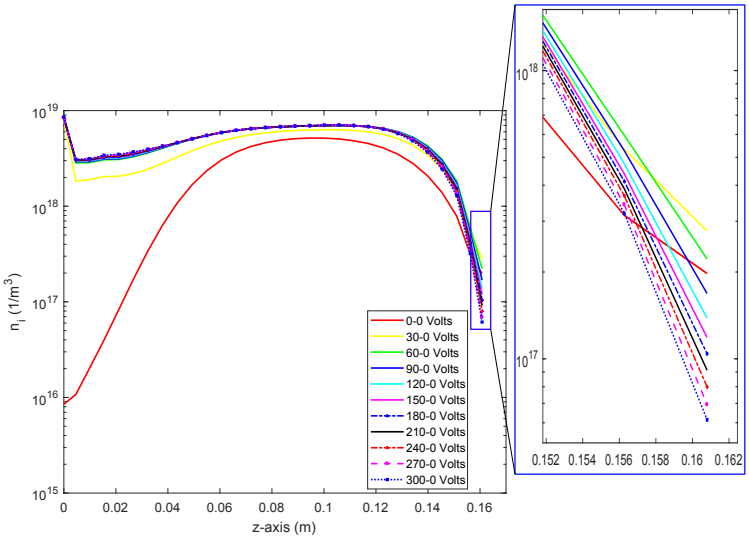

Figure 5.17: The effects of 11 different anode voltage on n_i at 1D.

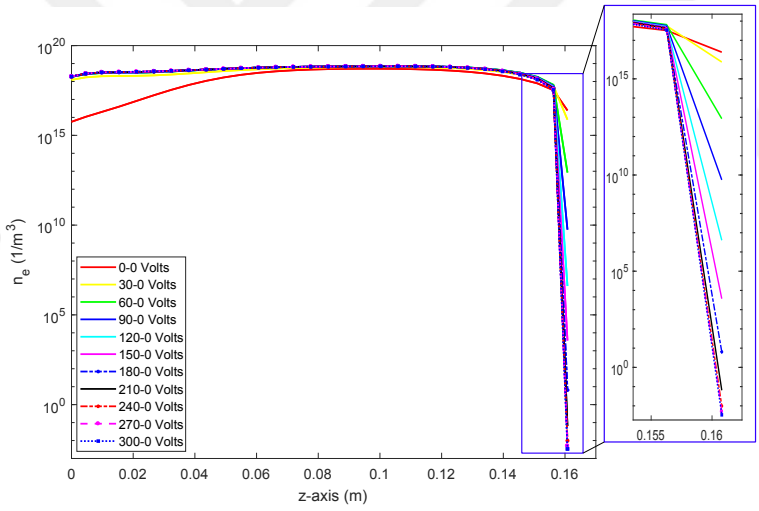

Figure 5.18: The effects of 11 different anode voltage on n_e at 1D

5.3 The effects of chamber geometry on the plasma parameters

Geometrical analysis of the system were done with respect to the Aspect Ratio. This ratio depends on two dimensions (length and diameter) of the plasma chamber. By fixing the diameter to $26,8$ mm from reference [57], the length is changed from $53,6$ mm to $160,8$ mm as shown in Figure 5.19.

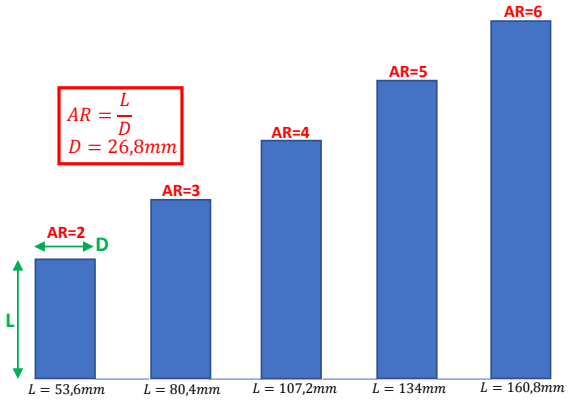

Figure 5.19: The geometries for five different Aspect Ratios.

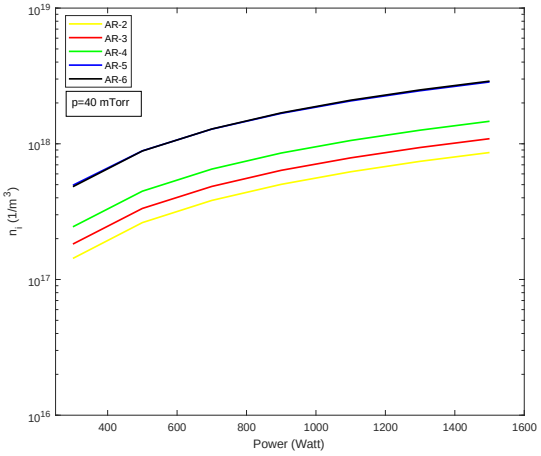

Figure 5.20: n_i at the screen grid vs. power for 5 different AR

For Figure 5.20, the working parameters are $p = 40$ mTorr, $V_{bound} = 0$ V. As seen from Figure 5.20, at constant pressure of 40 mTorr, the ion density increases with RF power and AR. High AR means high volume of the chamber. At constant pressure, if the volume gets larger, the density increases due to ideal gas law $PV = nRT$. In addition, with increasing RF coil power, the mean kinetic energy or the temperature of the free electrons would rise and therefore, the collisions between the electrons and the neutral atoms would increase. This will result in more ionization and more ion density. In addition, the ion densities of the $AR = 5$ and $AR = 6$ are overlapped.

As observed in Figure 5.20, the ion density increases with pressure which is demon-

strated in Figure 5.21, at 120 mTorr. There is a very small difference between the densities of $AR = 5$ and $AR = 6$ chambers at 120 mTorr pressure.

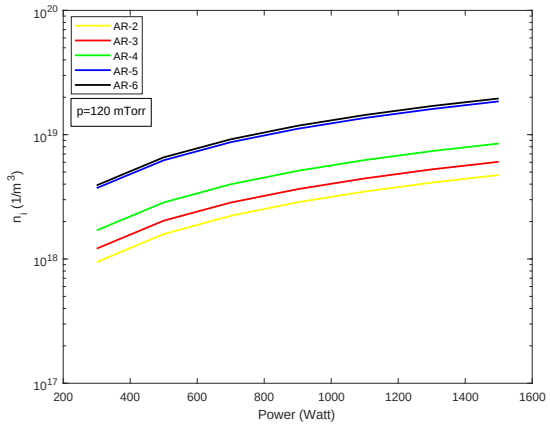

Figure 5.21: n_i at the screen grid vs. power and for 5 different AR, $V_{bound} = 0$ V.

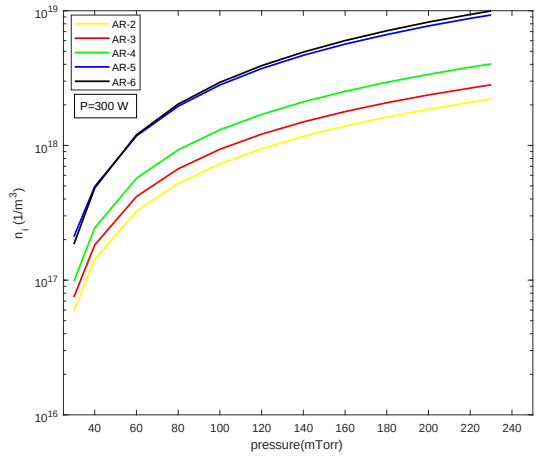

Figure 5.22: n_i at the screen grid vs. pressure, $V_{bound} = 0$ V, for 5 different AR.

From Figure 5.22, at a given constant RF power of $P = 300$ W, the ion density increases with AR and gas pressure. The densities for $AR = 5$ and $AR = 6$ are almost the same but when the pressure increases, the n_i values are deviating slightly between $AR = 5$ and $AR = 6$.

5.4 The effects of coil frequency on the plasma parameters

For this analysis, the working parameters of the simulation are set $P = 300$ W, $p = 40$ mTorr, $AR = 6$, $CT = 3$, $V_{bound} = 0$ V. Up to 12 MHz frequency, the ion density increases with frequency but after that point it decreases with increasing frequency at constant power and gas pressure as shown in Figure 5.23. At max point (12 MHz), the ion density is $4.85 \times 10^{17} m^{-3}$. For our simulation procedures, we have used 13.56 MHz RF source which is very close to this peak frequency. The reason for chosen this frequency is that there is a standart for RF power generators in commercial electronics.

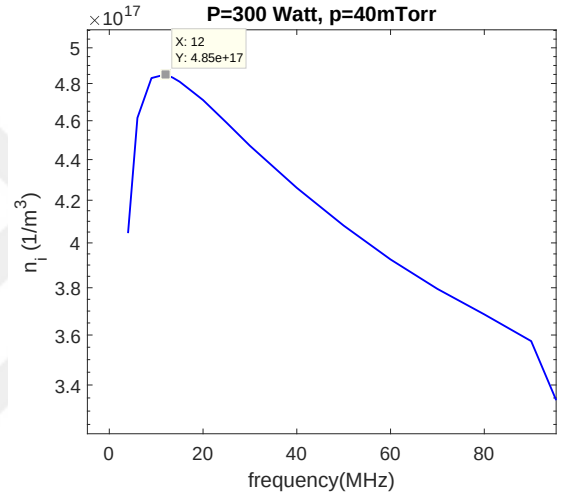

Figure 5.23: The n_i distributions that is taken at the screen grid location with respect to changing coil frequency at the 1D.

5.5 The effects of coil location on the plasma parameters

For this simulations, the working parameters are set to $P = 300$ W, $p = 40$ mTorr, $AR = 4$, $CT = 3$, $V_{bound} = 0$ V in that section. As seen from Figures 5.24 and 5.25, the electron and ion densities increase slightly when the coil location is shifted from middle section to the top (near to the screen grid). At the right of these two figures are seen that the densities are at higher levels at the surface of the screen grid.

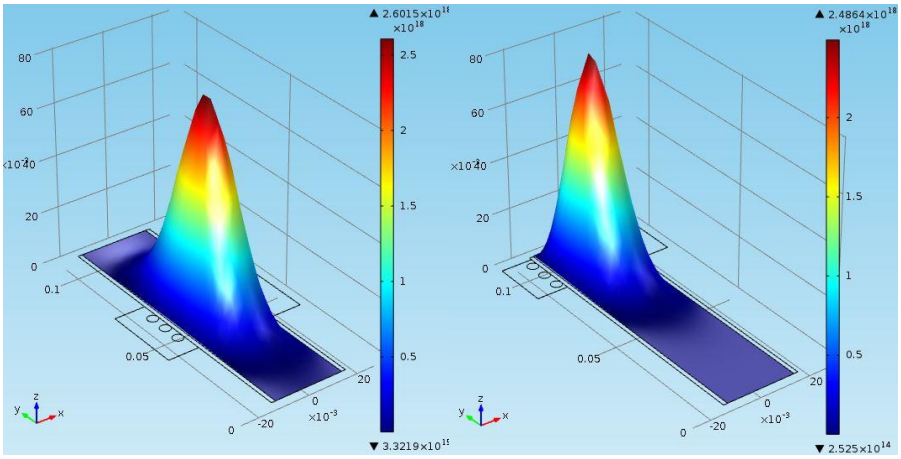

Figure 5.24: The effects on n_e when the coil locations are changed.

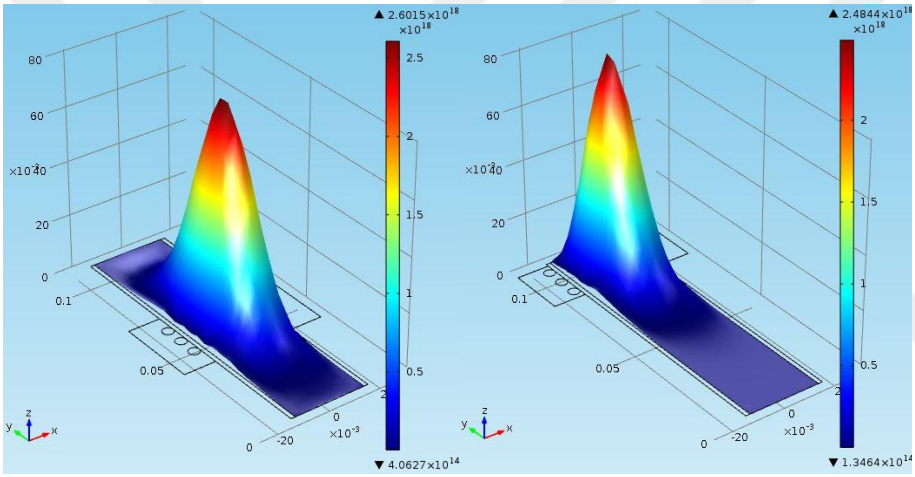

Figure 5.25: The effects on n_i when the coil locations are changed.

In Figure 5.26 blue lines indicate the ion density n_i, whereas, the red ones indicate the electron density n_e. At the left figure, the coils are placed at the middle section and at the right figure the coils are placed at the top. As seen from Figure 5.26, both electron and ion densities are the same due to quasi-neutrality nature of the bulk plasma. From the left graph (coils located at the center of the chamber), the ion densities are higher than the electron densities with almost the same amount for both sheath edges. However, when the coils are shifted towards to the screen grid, the difference between the ion and electron densities get higher at the sheath edge that is close to the screen grid. On the other hand, very small difference between these quantities is observed at the other sheath edge closer to the anode. At the screen grid

while there is an increase of about 24.5 times more ions, at the sheath edge there is an increase of 40.5 times for the ions when the coils are closer to the screen grid.

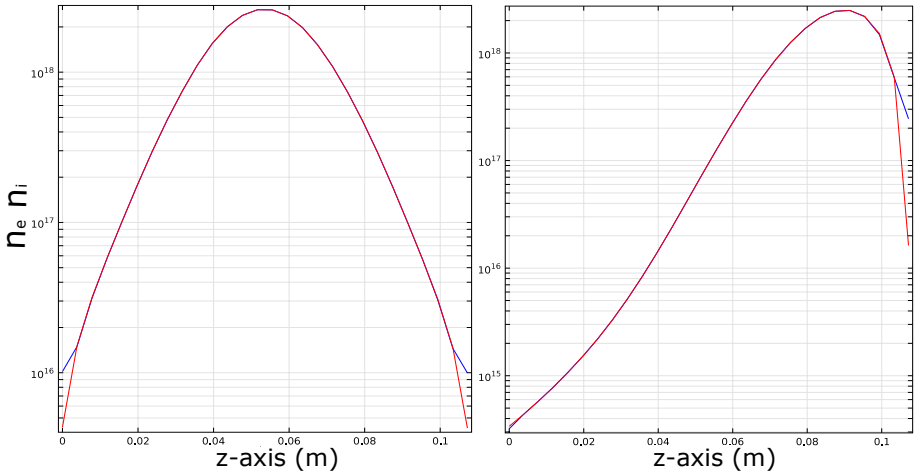

Figure 5.26: The effects of the changing coil location to the n_e and n_i.

Figure 5.27 shows the axial distribution of electron temperature when coils are placed at the middle (left figure) and at the right when coils are placed at the top. Figure 5.27 shows that although the shape profiles are the same, the maximum value of the electron temperature in the plasma increases a bit more (1.45 times) with changing the coil location from center to the up (close to the screen grid). Therefore, the coils location close to the screen grid is most desirable configuration in terms of the high ion density and high electron temperature to obtain high performance parameters, such as, thrust and Isp.

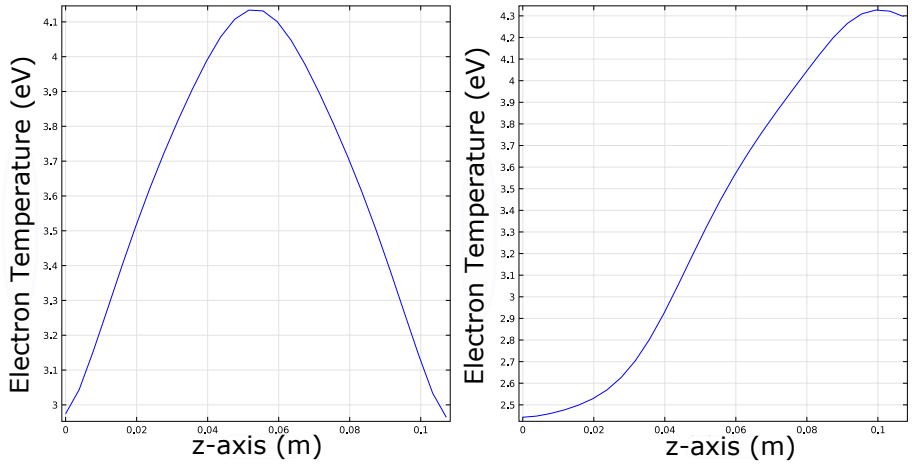

Figure 5.27: The effects of the changing coil location to the T_e.

CHAPTER 6

CHILD LANGMUIR SHEATH, ION OPTICS AND PERFORMANCE CALCULATIONS

6.1 Ion Optics

A sheath that has thickness on the order of a few Debye Length, is called Debye sheaths. It is assumed that the Debye shield exists when the potential drop between the system walls and bulk plasma is small with respect to electron temperature. This assumption gives permission for finite electron flux to sheath, and typically allow for electrically floating surface to be used. Therefore, no current is drawn from the plasma. The Debye Length can be calculated with Eq.32.

$$\lambda_D = \Big(\frac{\varepsilon_0 k_b T_e}{n_0 e^2}\Big)^{1/2} \tag{32}$$

The plasma sheath thickness depends on bulk plasma density and the electron temperature and is inversely proportional to the square root of the plasma density and is proportional to the square root of the electron temperature.

The other case is when the potential drop is large with respect to the electron temperature which causes almost no electron flux. Sheaths of this type are called Child-Langmuir sheaths. The maximum ion current density through a Child-Langmuir sheath is given by Eq.33.

$$j_{max} = \frac{4\varepsilon_0}{9}\big(\frac{2e}{M_i}\big)^{1/2}\frac{(V_S - V_A)^{3/2}}{l_e^2} \tag{33}$$

In this equation l_e is the sheath thickness, V_s is the voltage of the screen grid, V_a is

the voltage of the accel grid, ε_0 is the electric permittivity of the free space, e is the unit charge, and M_i is the mass of an ion.

If the system dimensions reduce to the 1D, by means of using the 1D Poisson's equation, the generic solution of the Child-Langmuir sheath can be found and is given in detail in Appendix-D. With taking into account this assumption, a high voltage plasma sheath will exist between the bulk plasma and any surface of contact, such as an electrode having high voltage with respect to the electron temperature. The ions that enter the sheath edge approach at least the Bohm velocity whose value doesn't depend on the potential drop between the plasma and high voltage electrode. After the ions enter the sheath, they are accelerated to very high velocities. The region of the sheath is the main interest of the design and the design of the electrodes is the most important point which shapes the sheath. Designing the geometry of the electrodes, and focusing and acceleration of the ions, is called the ion optics.

The grids used in the ion space thruster systems are the most widespread components. They supply not only high ion transparency but also suitable small grid when they are scaled with plasma sheaths. The common extractor units consists of two electrodes: screen grid and accelerator (accel) grid. The main extraction is supplied from screen grids, whereas, the acceleration of the ions is with the accel grid which interacts with plasma sheath properly. The screen grid only takes ions from bulk plasma and allow them to go through the place between the screen grid and the accel grids. Additionally, the screen grid has the potential which is nearly below from the plasma potential. This drop is of the order of 20-30 Volts. Due to small decrease of the electric potential between the anode and the screen grid, the ions that is coming from bulk discharge plasma is received by the screen grid. On the other hand, the velocity of the ions does not increase much when compared to that of the plume ions at the vacuum side of the thruster. The accel grid has negative potential with respect to the ground and the highest velocity ions is supplied from the accel grid. In this process, the ions follow the proper trajectory that of the electric field lines.

The reason why we have two succesive grids, screen grid and accel grid, for discharging ions from the thruster is to slow down the acceleration of the ions. This slowing down is done by increasing the voltage drop in two steps. Without this slow down

mechanism the rapid acceleration of the ions will erode the screen grid and its effectiveness will not persist for long. This effect can also be observed when one examines the potential drop values across these two grids as shown in Figure 6.14. The voltage drop across the first grid, screen grid, is about 70 V under the effect of which the ions are accelerated gradually but still not attaining their terminal velocity. However after the second grid, the accel grid, the voltage drop is remarkably increased and the ions are accelerated up to their terminal velocity which corresponds to the net acceleration potentail drop $V_T = 422V$ as seen in Figure 6.14. With this two step acceleration mechanism, the abrupt acceleration of the ions are prevented and the ions have enough time to reorganize their smooth trajectories when crossing through the grids of the screen. This reorganization will also help to reduce the erosion of the grid with random hitting of the ions on the surface of the grid elements. This surface erosion in turn will deform the geometry and the regular spacings of the grid and will reduce the thrust generated. Therefore two step screening of the ions are necessary to eliminate the risk of excessive erosion of the screen and the accel grids.

The high speed ions passing through the accel grid collide with the slow neutral atoms rarely resulting in charge-exchange reactions. After these reactions, the fast neutral atoms and low speed-low-energetic ions are produced. Furthermore, these ions are accelerated back to the thruster due to a negative electric field located between the space potential and the accel grid potential. Thus, they hit the accel grid with the energy that they receives from this negative electric field. Thereby, they erode and sputter the accel grid. In order to prevent this emerged back ion flows, the third grid is used who is named as a the decelerator (decel) grid and is typically positioned some distance downstream of the accel grid. When the decel grid is used, it shields the accel grid and prevents its erosion. In this study the decel grid is not used for the sake of simplicity and only screen and accel grids are used in order to be simple for operation. Figure 6.1, represents a clear diagram of the three-grid usage and it shows the corresponding electric potential along with three-grid system assembly.

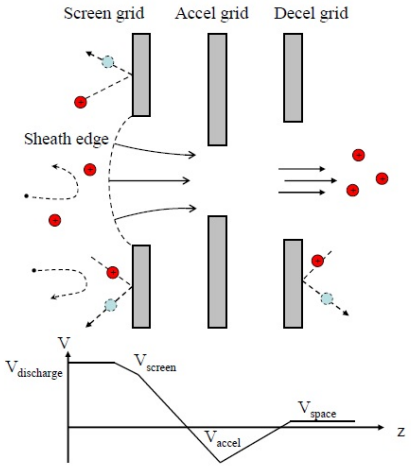

Figure 6.1: A three-grid configuration and electric potentials distribution [10].

The total extraction of the ion current is restricted by the voltage drop between the screen and the accel grids and the geometry of the apertures. The reason for the Child-limited current is the limited ion current caused from the repelling force between the positive charged ions. This repelling force between the ions can reach a limiting value for which the current flow or the ion current density is no longer allowed from the extractor system which causes the current to have a limited value due to this space-charge effects. Therefore, the extraction of excessive ions becomes ultimately impossible with this process. This limiting value is determined from the potential difference between grids and the grid geometries. In the extracting region there are no any electrons and their thermal kinetic energy is so small with respect to the potential drop between the grids and therefore, this sheath is called as Child Langmuir sheath. The extractable current density, thus, consists of only the ion flux whose value can be calculated with Eq.33.

When designing the grid assembly, the main aim is to match the sheath thickness, l_e, with the actual distance between the grids. Due to the fact that the sheath will form a slight dome, the desired sheath thickness is given Eq.52.

The most important design parameters for extractor grids of the electrodes comprise of the screen grid diameter, the accelerator grid diameter, the thickness of the electrodes, and the distance between electrodes. The screen grid diameter has a maximum value of a few Debye Length. The grid diameter of the accelerator electrode and the distance between the electrodes can not be determined analytically and must be de-

termined with computer simulations. In this thesis the simulation of the trajectories of the ions with the given geometry and with the given voltages of the electrodes are calculated with Charge Tracing Module of the COMSOL.

The trajectory of the ions are aligned by means of the proper geometry of the screen and accel grids such that the electric field between them focuses the ions. The transparencies of the ions and neutrals are determined with the screen and accel grids geometries. The ion transparency is determined by the screen grid while the transparency of the neutrals is set by accel grid. Accordingly, it is useful to maximize the ion transparency of the screen grid in order to increase the thruster operating performance while it is advantageous to minimize the neutral transparency at the accel grids in order to avoid neutrals from escaping and, therefore, to increase the ionization rate at the discharge chamber [19]. On the other hand, there is a lower bound for accel grid to do as small as possible since the high energy incoming ions begin to hit the accel grid beyond this lower bound and they start to erode the material. Equivalently the optimum lateral distance between the two grids is usually smaller than the screen grid aperture diameter with a minimum separation distance of about 1 mm per 2.3 kV of potential difference between the carbon based grids to avoid electric breakdown and to prevent arcing between the electrodes [58].

Between the screen and the accel grids, there is an acceleration and between the accel grid and the space potential or the plume potentail there is a deceleration. Space or plume potential is created by the ions where the plume is. Therefore, the ions coming from the discharge chamber sees the net acceleration potential V_N and the total beam velocity is not calculated with the potential between screen and accel grids or V_T. It is calculated by using the potential drop between anode potential and plume potential, V_N, as is seen from Figure 6.2.

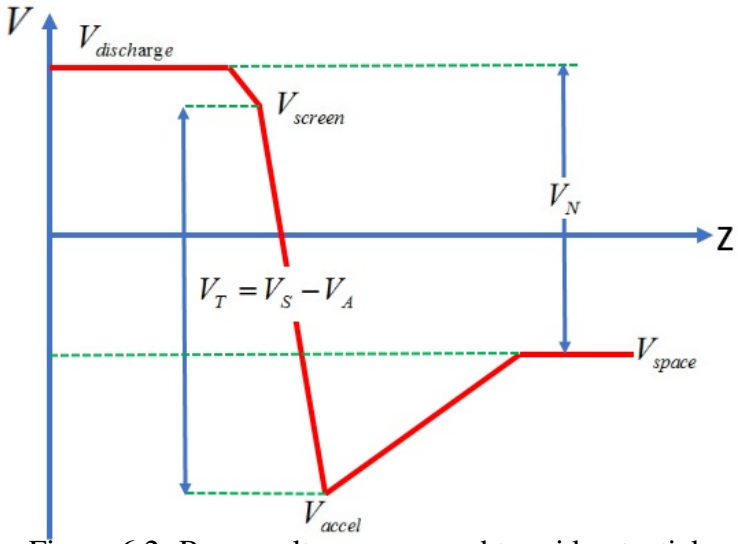

Figure 6.2: Beam voltage compared to grid potentials.

The potential drop between the grids is given as the potential drop V_T, which generally exceeds the beam voltage V_N and the accel electrodes are usually biased below common. The accel grid which is negatively biased pushes the electrons downstream which are coming from the neutralizer cathode, since there is a negative electric field at that region. If this were not the case, electrons would flow freely backwards to the thruster. This process is called as electron back-streaming. Back-streaming cause the current of the electrons which is recycled through the discharge anode to the neutralizer cathode, which is a source of inefficiency. Thus, while biasing the accel grid below common to avoid electron back-streaming, it enhances the efficiency.

Moreover, if the electric voltage between the screen and the accel grids is increased, the current drawn can be maximized. With these improvements, on the other hand, while $V_T = V_S - V_A$ is increasing with respect to the beam voltage, the ions of the charge exchange collisions are accelerated due to this negative electric field which is undesirable. The voltage dependency between V_T and V_N is given with their voltage ratio, R, which is generally designed to be between $0.7 - 0.8$ [59] and is given with Eq.34. By means of the acceleration of the ions at the second region, they hit the accel grid and they cause ion impingement. Therefore, the lifetime of the thruster would be

limited with this erosion.

$$R = \frac{V_N}{V_S - V_A} \tag{34}$$

The running pathway of the ions depend on the configuration of the aperture geometries. It also depends on the shape of the plasma sheath. The shape of the sheath is not fixed, but varies with the drop of the potential between the grids and the ion current density which is supplied from plasma discharge. This variance is determined by a parameter called the perveance. Perveance is explained in detail in the next section.

6.2 Perveance

The relation between the ion or the electron beam current and the extraction voltage of the source is defined by the perveance. The aperture size of the screen grid is determined so that sufficient extraction of the ions are provided. The grid gap distance is selected to ensure the maximum perveance. Maximum total current density, which is space charge limited, is calculated by using Eq.33, and I_{max}, which is the maximum electrical current transported through the all apertures, is calculated by using Eq.35.

$$I_{max} = k_{total} \frac{\pi \varepsilon_0}{9} \sqrt{\frac{2q}{M_i}} \Big(\frac{D_S}{l_e}\Big)^2 \Big(V_S - V_A\Big)^{3/2} \tag{35}$$

In this equation $V_S - V_A = V_T$ is the potential drop between the screen and the accelerator grids, M_i is the mass of the used propellant, k_{total} is the total grid number at the electrodes, D_s is the screen grid diameter. l_e is the effective sheath thickness and is calculated by using Eq.52. The space charge limited current is given in Eq.36 as simple explanation.

$$I_{max} = P(V_T)^{3/2} \tag{36}$$

The perveance can be calculated by using Eq.37 for the given electrode geometry.

$$P = k_{total\ grid\ number}\frac{\pi\varepsilon_0}{9}\sqrt{\frac{2q}{M_i}}\left(\frac{D_S}{l_e}\right)^2[A/V^{3/2}] \tag{37}$$

Upper value for the perveance can be determined by satisfying that the Child sheath thickness l_e is small with respect to the screen grid aperture diameter D_S or the visa versa.

The beam current variations may be defined in terms of the normalized perveance per grid by using Eq.38. Eq.38 shows that there is a maximum limit for the normalized perveance per grid for a particular gas used. For Mercury, the propellant of interest for electric space propulsion, the upper value is $3.03 \times 10^{-9} A/V^{3/2}$. For Argon, the propellant gas used in this thesis, has the value of $6.79 \times 10^{-9} A/V^{3/2}$. Normalized perveance per grid $\left(I_{max}/V_T^{3/2}\right)\left(l_e/D_S\right)^2$ will be used to describe the ion extraction performance of each aperture concerned.

$$P_{max} = \frac{I_{max}}{(V_T)^{3/2}}\left(\frac{l_e}{D_S}\right)^2 = \frac{\pi\varepsilon_0}{9}\sqrt{\frac{2q}{M_i}} \tag{38}$$

The perveance serves as a measure of the sheath placement with respect to the screen grid. The expected case of the sheath extends throughout the screen grid aperture and forms a concave "lens" to focus the ions through the smaller accel grid aperture as shown in Figure 7.1. This condition only becomes for certain match between the discharge plasma parameters and applied voltages V_T on the grids. Moreover, the concave lens and desired ion trajectories can not be determined analytically and must be calculated with computer simulations.

There are two governing parameters that control the location of the sheath edge and ion-focusing effect. The first one is the total coming ion current density from the sheath and the second one is the total potential drop between the grids. The ion current density is calculated with Eq.39.

$$J_i = en_i u_{Bohm},\ u_{Bohm} = \left(\frac{k_b T_e}{M_i}\right)^{1/2} \tag{39}$$

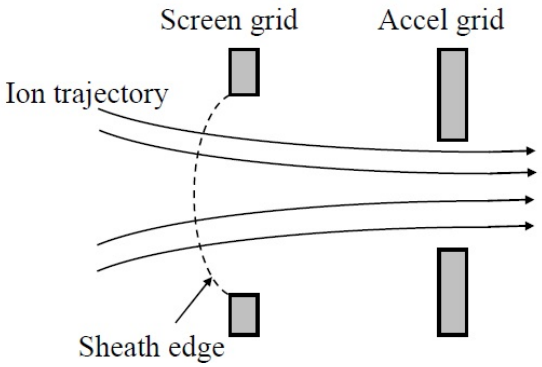

Figure 6.3: Optimum perveance [10].

where e is the unit charge, n_i is the ion number density, u_{bohm} is the ion Bohm velocity, k_B is the Boltzmann constant, T_e is the electron temperature, and M_i is the mass of an ion for used propellant gas. The ion number density n_i and the electron temperature T_e are calculated with the COMSOL software at the sheath edge in this thesis. With an increment in the bulk plasma density or a reduction in temperature of the electrons for constant V_T voltage, the thickness of the sheath will drop as it can be calculated from Eq.32 and the ion lens is carried toward the accel grid. The relation between the Child Langmuir sheath thickness and Debye Length is $l_e \approx (2-3)\lambda_D$, therefore, when Debye Length changes, the Child Langmuir sheath thickness also changes. At the limiting value of the increasing electron density or decreasing electron temperature, it ends up with some ions having ineffective focusing and increases the ion impingement on the accel grid. In this case, the perveance is higher than that of the optimum, and this situation is called as "over-perveance" as shown in Figure 6.4. This is an expected result because the perveance and the sheath thickness l_e are inversely proportional to each other as seen from Eq.37.

Additionally, decreasing the bulk plasma density or increasing the electron temperature causes the Debye Length to increase which can be calculated from Eq.32. With this condition the sheath boundary extends towards the discharge plasma. This situation is called as "under-perveance" due to the inverse relation between the Child sheath thickness and perveance. This case is seen in Figure 6.5. The ions are over-focused and they will cross the trajectories of the neighboring apertures as is shown in Figure 6.5. The second reason for the under-perveance is the increment of the voltage between the grids. When the ion current density is constant, increasing trend of the

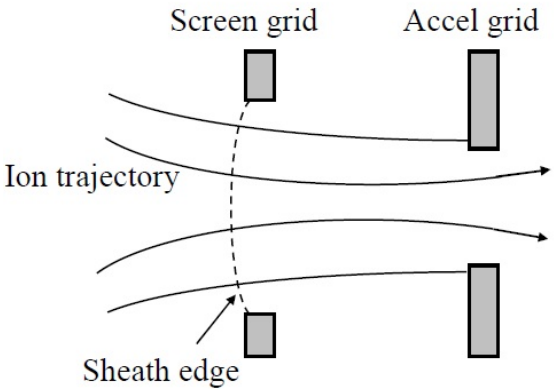

Figure 6.4: Over perveance [10].

sheath thickness can be seen from Eq.40. If the l_e is taken to the left hand side of Eq.35, Eq.40 can be obtained.

$$l_e = V_T^{3/4} I_{i,Child\max}^{-1/2} D_S \sqrt{\frac{k_{total}\pi\varepsilon_0}{9}} \left(\frac{2q}{M_i}\right)^{1/4} \tag{40}$$

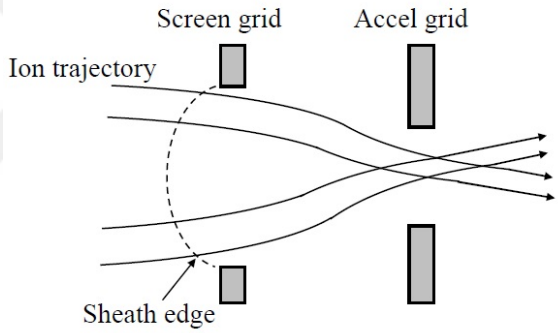

Figure 6.5: Under perveance [10].

The conditions for the perveance are seen from Figure 6.6. The optimum case for the perveance is given at the middle condition of this figure.

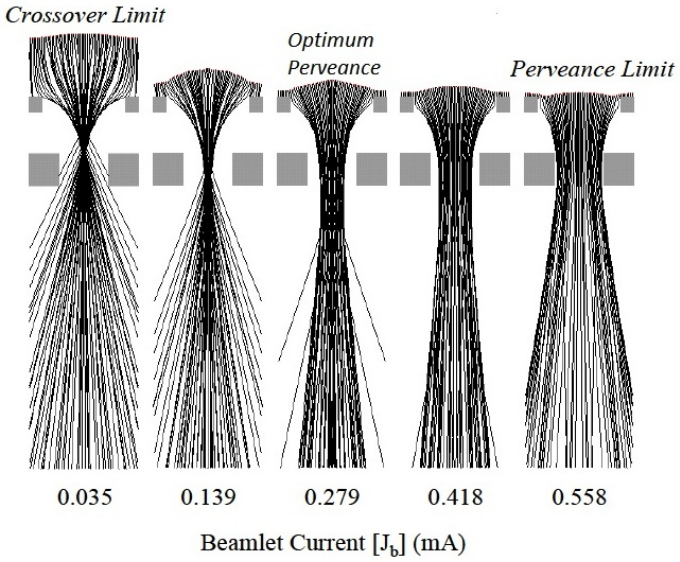

Figure 6.6: Trajectories of ion beamlets released from the sheath, the crossover limit, optimum perveance and perveance limits are seen [11].

6.3 Performance calculations of RF ICP ion thruster

In order to calculate the thrust, Eq.41 or Eq.42 can be used.

$$T = \dot{m}_{ion} v_{exhaust} \tag{41}$$

$$T = I_{i,Comsol} \frac{M_i}{e} \sqrt{\frac{2eV_N}{M_i}} \tag{42}$$

$$I_{sp} = \frac{1}{g} \sqrt{\frac{2eV_N}{M_i}} \tag{43}$$

First, the total ion currrent $I_{i,Comsol}$ and the total ion acceleration voltage V_N should be calculated to get the thrust T and the specific impulse I_{sp} by using Eq.42 and Eq. 43. Eq.42 is derived from Eq.41. Where M_i is the ion mass, e is the unit electric charge and g is the gravitational acceleration.

In order to obtain the total ion current, the ion current density should be calculated from the data of the Comsol simulations and therefore, the ion number density and

the electron temperature values at the sheath edge are used as two input parameters. The 2D n_i distribution over the solution space for the thruster in the Comsol is seen in Figure 6.7. The value of n_i is taken from the sheath edge at the 1D distribution as is seen from Figure 6.8. This value is $n_{i,Comsol} = 5.13 \times 10^{16}\ m^{-3}$. The 2D T_e distribution over the solution space of the thruster in the Comsol is seen Figure 6.9, and the T_e value is obtained from the sheath edge at the 1D distribution as one can see from Figure 6.10. This value is calculated as $T_{e,Comsol} = 3.43625$ eV at the sheath edge. These $n_{i,Comsol}$ and $T_{e,Comsol}$ data are obtained when the gas pressure is taken being equal to 50 mTorr, and system electrical power is equal to 300 W.

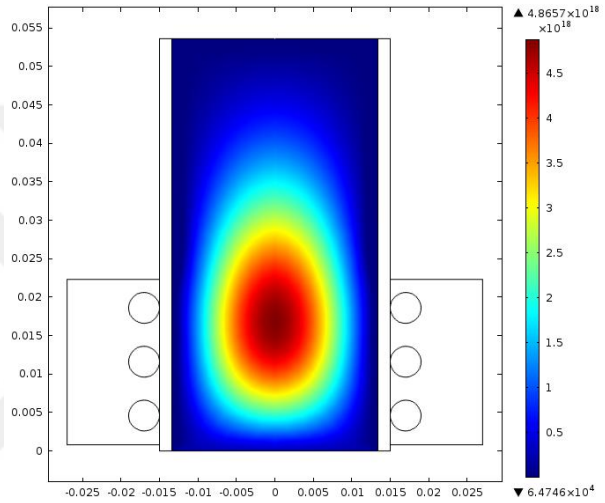

Figure 6.7: 2D ion number density result of the COMSOL.

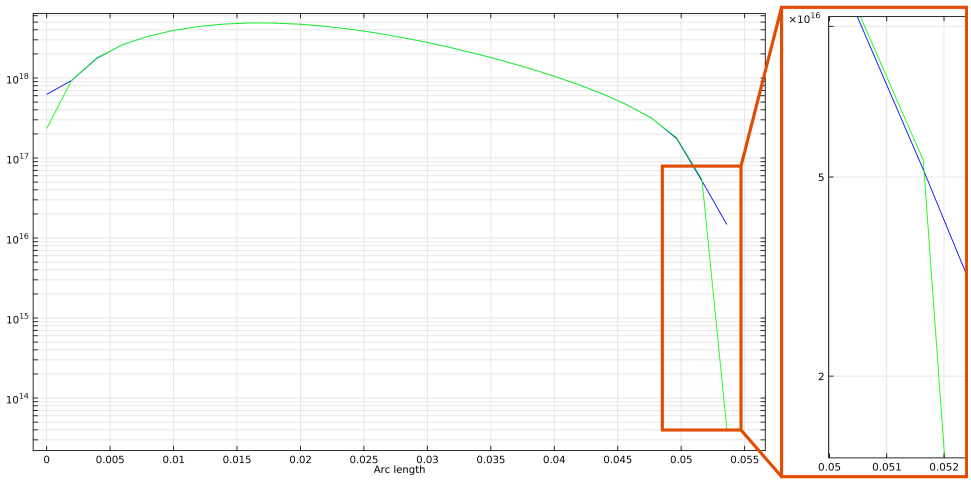

Figure 6.8: 1D ion-electron number density result of the COMSOL. Sheath edge results of the ions are in the right figure. Unit is in m^{-3}.

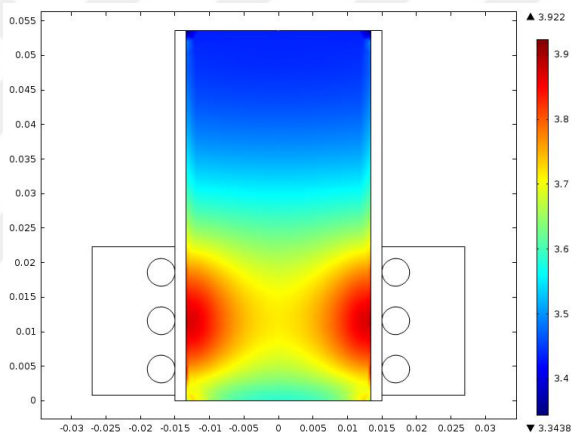

Figure 6.9: 2D electron temperature result of the COMSOL. The unit is in eV.

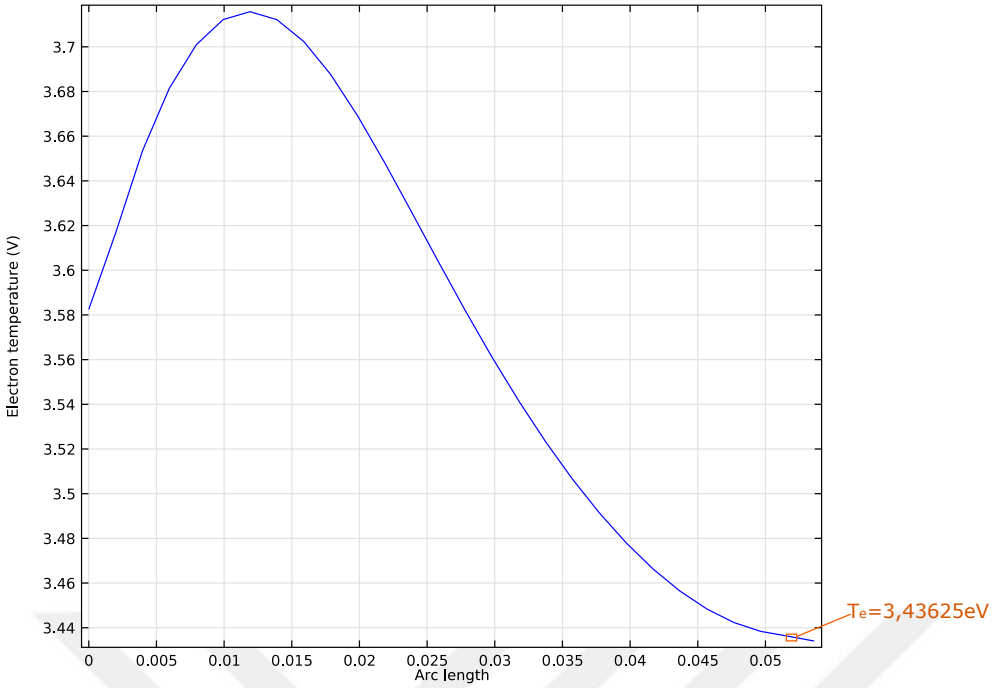

Figure 6.10: 1D electron temperature result of the COMSOL.The unit is in eV.

To obtain the ion current density value, Eq.44 is used

$$J_{i,Comsol} = en_{i,Comsol}u_{Bohm,Comsol} \tag{44}$$

where $u_{Bohm,Comsol}$ is the ion Bohm velocity at the sheath edge calculated with Eq.45.

$$u_{Bohm,Comsol} = \sqrt{\frac{eT_{e,Comsol}}{M_i}} \tag{45}$$

$u_{Bohm,Comsol} = 2878.92$ m/s is obtained after this calculation. The ion current density is obtained by using the Eq.44 and it is calculated as $J_{i,Comsol} = 23.63\ A/m^2$ when $n_{i,Comsol} = 5.13 \times 10^{16}\ m^{-3}$.

The total ion current should be obtained for the calculation of thrust as is seen from Eq. 42 and is calculated with Eq. 46 for this aim.

$$I_{i,Comsol} = J_{i,Comsol} \times\ Area_{Total} \tag{46}$$

$Area_{total}$ is calculated with Eq.47 when the total grid number $k_{Total} = 85$ at the

screen electrode.

$$Area_{total} = Area_{one\ grid} \times k_{Total} \tag{47}$$

The area of the one grid is calculated with Eq.48 when the screen grid diameter is equal to $D_s = 1.9$ mm, and is obtained as $Area_{one\ grid} = 2.84 \times 10^{-6}\ m^2$

$$Area_{one\ grid} = \pi \frac{{D_S}^2}{4}\ , \tag{48}$$

$Area_{total}$ is calculated by using $Area_{one\ grid}$ with Eq.47 and its value is equal to $Area_{total} = 2.41 \times 10^{-4}\ m^2$

The total ion current $I_{i,Comsol}$ is calculated as 0.00569 A or 5.7 mA by using Eq.46 with the calculated ion current density $J_{i,Comsol} = 23.63\ A/m^2$ and total area of the grids $Area_{total} = 2.41 \times 10^{-4}\ m^2$.

Until to this last step the total ion current has been calculated, the net ion beam acceleration potential V_N should be obtained for the thrust and Isp calculations by using Eq.42 and Eq.43. In order to get the V_N, the relation between the Child Langmuir voltage V_T and the V_N are used with Eq.49. The R constant can be chosen between 0.5 and 0.9 from reference [59] and is choosen as 0.7 for the calculations in this thesis.

$$\frac{V_N}{V_T} = R \tag{49}$$

By taking V_T to the right hand side from Eq.36, Eq.50 can be written to calculate V_T.

$$V_T = \left(\frac{I_{i,Child}}{P} \right)^{2/3} \tag{50}$$

The $I_{i,Child}$ should be determined in order to calculate the V_T. Therefore, the relation between the $I_{i,Comsol}$ and $I_{i,Child}$ is used in Eq.51.

$$\frac{I_{i,Comsol}}{I_{i,Child}} = \eta \tag{51}$$

$I_{i,Child}$ is the maximum extractable total ion current with a given constant potential drop which is V_T and it is the limit of the ion current value for the considered system. Due to this reason the measured current always should be smaller than the Child Langmuir Law limited ion current $I_{i,Child}$ and this dependency is clearly seen from Figure 6.11.

Therefore the η value should always be between $0\ and\ 1$. In this thesis the η is chosen as 0.6. It means that the ion producing efficiency of the system is $\%60$ or, in other words, when 10 pieces of the ions are generated in the plasma chamber, 6 ions are pulled from there to the beam ions.

When η is equal to 0.60 and $I_{i,Comsol}$ is equal to 5.7 mA, the Child limited current $I_{i,Child}$ is obtained as 0.00949 A or 9.49 mA by using Eq.51.

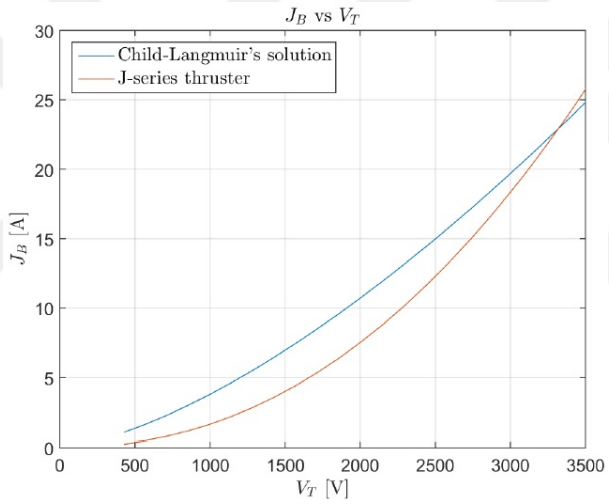

Figure 6.11: Maximum ion current for a given thruster design, as a function of the total voltage [12].

In order to obtain V_T which is the potential drop between the screen and the accel grids, Eq. 50 is used and $I_{i,Child}$ and the perveance are to be used in this calculation. The Child sheath thickness should be calculated with Eq.52 in order to calculate the perveance.

$$l_e = \sqrt{(l_g + t_s)^2 + \frac{D_s^2}{4}} \tag{52}$$

In this equation l_g is the distance between the screen and the accelerator grid, t_s is the grid thickness and D_s is the grid diameter of the screen grid. These geometrical dimensions are given in Figure 6.12. The geometrical dimensions of the electrodes and the grid are taken from literature [60] as $D_S = 1.9$ mm, $t_s = 0.4$ mm, $l_g = 0.6$ mm. By using these values and Eq.52 the l_e is calculated as 1.4 mm.

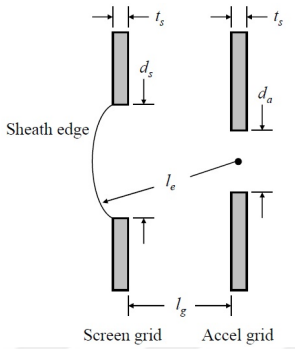

Figure 6.12: Two gridded system and effective sheath approximation [10].

While the main geometrical parameters D_s and l_e are exact, the perveance can be calculated with Eq.37. When $k_{total\ grid\ number}$ is equal to 85, the perveance is calculated as $1.09486 \times 10^{-6}\ A/V^{3/2}$. The V_T is calculated with Eq.50 by using the $I_{i,Child} = 9.49$ mA and by using the calculated perveance value. V_T is obtained and it is equal to 422 V.

After performing the thruster plasma chamber simulations which we have implemented to get the ion plasma density and the electron temperature, we had two set of data. These are the ion Child dependent current $I_{i,Child}$ and electric potential drop V_T. Their calculations are done, when the gas pressure is changed from 50 to 190 mTorr, and power is equal to 300 W and perveance is equal to $1.09486 \times 10^{-6} A/V^{3/2}$. The dependency of $I_{i,Child}\ and\ V_T$ is seen from Figure 6.13

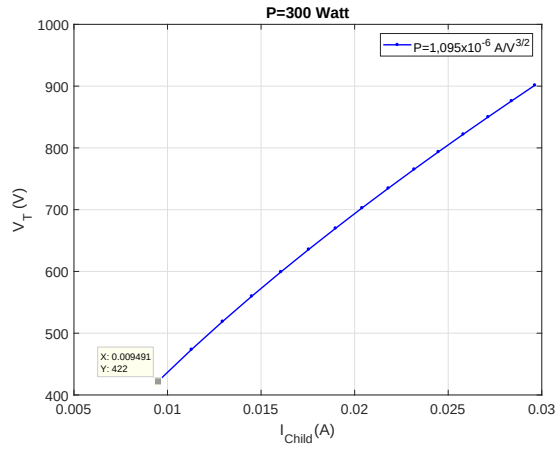

Figure 6.13: Child dependent ion current vs V_T.

After the calculation of the potential drop V_T, the net ion beam voltage V_N is calculated by Eq.49 and is equal to $V_N = 295.4$ V when the voltage ratio is $R = 0.7$. The space potential is calculated with Eq.53 and accel potential is calculated with Eq.54 when $V_{anode} = 100$ V and $V_{screen} = 70$ V.

$$V_{space} = V_{anode} - V_N \tag{53}$$

$$V_{accel} = V_{screen} - V_T \tag{54}$$

Afterwords the calculated values of the space and screen voltages are found as $V_{space} = -195.4$ V and $V_{accel} = -352$ V by using Eq.53 and Eq.54,

The thrust and Isp are calculated by using Eq.42 and Eq.43 and their values are $T = 0.0891$ mN, $Isp = 3848$ s.

The calculated performance parameters are summarized in Table 6.1.

Table 6.1: The table of the performance parameters of the given thruster before the optimum perveance value is applied.

	Value	Equation
$n_{i,Comsol}$	$5.13 \times 10^{16}\ m^{-3}$	Comsol $P = 300\ W, p = 50\ mTorr$
$T_{e,Comsol}$	$3.43625\ eV$	Comsol $P = 300\ W, p = 50\ mTorr$
$u_{Bohm,Comsol}$	$2878.92\ m/s$	Eq.45
k_{total}	85	From the designed geometry
η	0.60	Design constant
R (Voltage Ratio)	0.70	from ref [59]
D_S	$1.9\ mm$	from ref [60]
l_g	$0.6\ mm$	from ref [60]
t_s	$0.4\ mm$	from ref [60]
$Area_{one\ grid}$	$2.84 \times 10^{-6}\ m^2$	Eq.48
$Area_{total}$	$2.41 \times 10^{-4}\ m^2$	Eq.47
$J_{i,Comsol}$	$23.63\ A/m^2$	Eq.44
$I_{i,Comsol}$	$5.7\ mA$	Eq.46
$I_{i,Child}$	$9.49\ mA$	Eq.51
P	$1.09486 \times 10^{-6} A/V^{3/2}$	Eq.37
V_T	$422\ V$	Eq.50
V_N	$295.4\ V$	Eq.49
V_{Anode}	$100\ V$	From the design point.
V_{Screen}	$70\ V$	From the design point.
V_{Space}	$-195.4\ V$	Eq.53
V_{Accel}	$-352\ V$	Eq.54
$Thrust$	$0.0891\ mN$	Eq.42
Isp	3848 s	Eq.43

After performing all these calculations above, the potential distribution along the electrodes is obtained and is given at Figure 6.14.

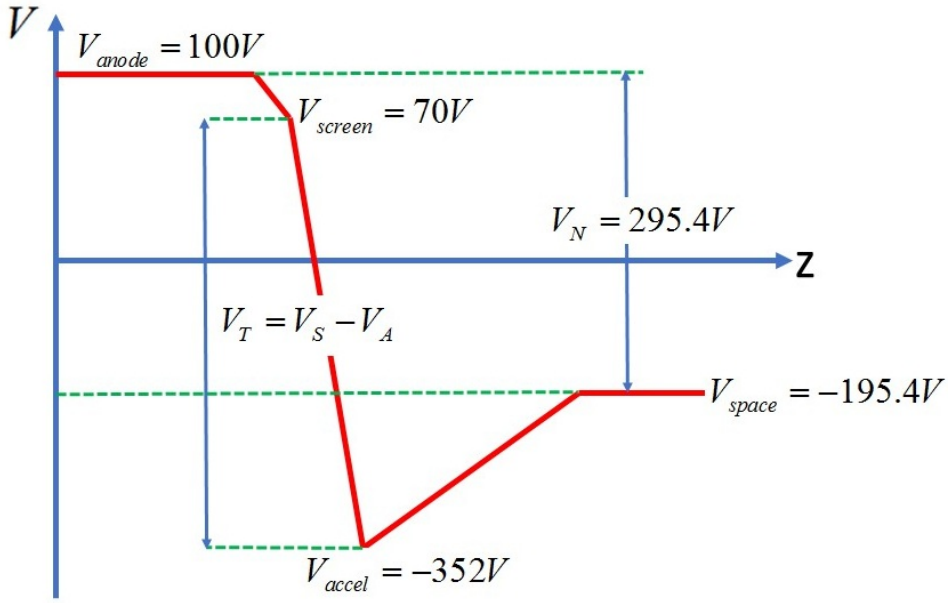

Figure 6.14: Electric potential distribution along the thruster. P=300W, p=50mTorr

6.4 Performance Results

Pressure dependencies of Trust and Isp at constant RF power are clearly seen in Figures 6.15 and 6.16. As seen from Figures 6.15 and 6.16, thrust increases linearly with pressure from 0.089 to 0.41 mN whereas a non-linear increase is observed for the value of Isp with the gas pressure from 3848 to 5624 s. As seen from Figure 6.17, when the net acceleration potential V_N increase from 295.4 V to 631 V, the I_{sp} changes from 3848 s to 5624 s almost linearly.

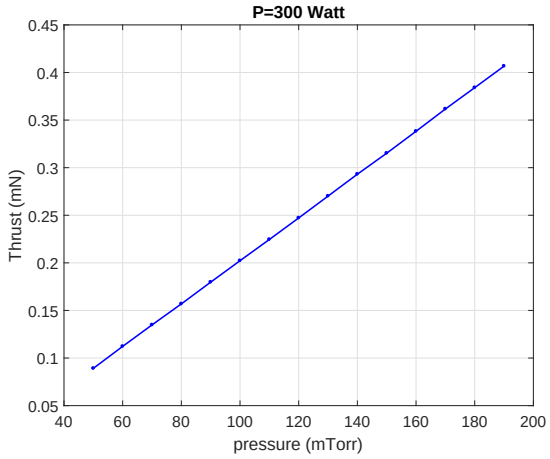

Figure 6.15: Pressure vs Thrust distribution. 3 turn coils, coils are at the below of the chamber. V_{anode} is equal to 100 V, V_{screen} is equal to 70 V, $P = 1.09486 \times 10^{-6} A/V^{3/2}$.

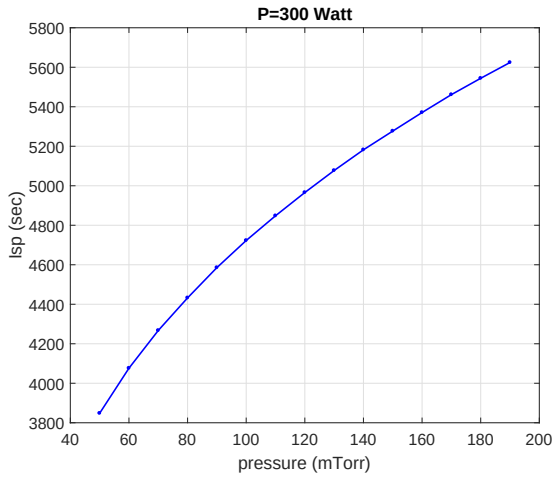

Figure 6.16: Pressure vs Isp distribution. 3 turn coils, coils are at the below of the chamber. V_{anode} is equal to 100 V, V_{screen} is equal to 70 V, $P = 1.09486 \times 10^{-6} A/V^{3/2}$.

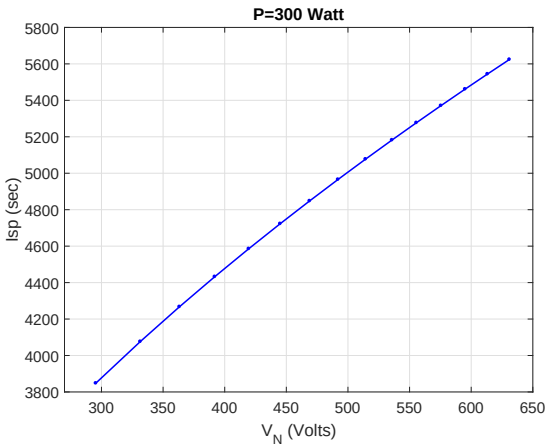

Figure 6.17: Net acceleration potential vs. Isp distribution. 3 turn coils, coils are below the chamber. V_{anode} is equal to $100\ V$, V_{screen} is equal to $70\ V$, $P = 1.09486 \times 10^{-6} A/V^{3/2}$.

Evolutions of the Trust and Isp with respect to the RF power at constant pressure are shown in Figures 6.18 and 6.19. Trust increases non-linearly with RF power from $0.01973\ mN$ to $1.335\ mN$. A non-linear increase is also seen in the value of Isp with power from 2639 to 7570 s. Similar distributions for Figures 6.18 and 6.19 are also observed from references [61–63].

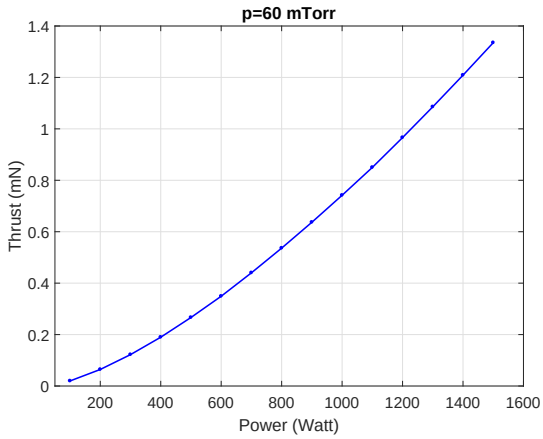

Figure 6.18: Power vs. Thrust distribution. 3 turn coils, coils are at the below of the chamber. V_{anode} is equal to $40\ V$ and V_{screen} is equal to $10\ V$, $P = 1.09486 \times 10^{-6} A/V^{3/2}$.

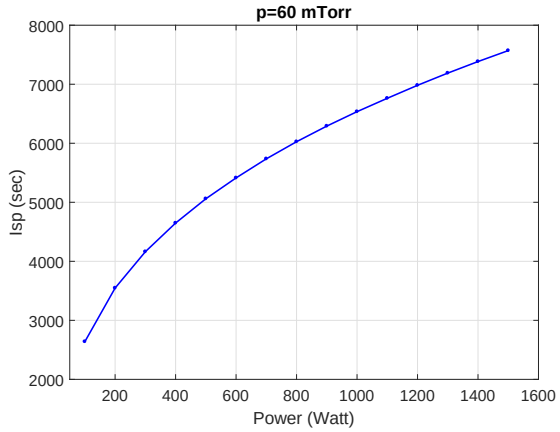

Figure 6.19: Power vs. Isp distribution. 3 turn coils, coils are at the below of the chamber. V_{anode} is equal to $40\ V$ and V_{screen} is equal to $10\ V$, $P = 1.09486 \times 10^{-6} A/V^{3/2}$.

The thrust and Isp dependency with respect to RF coil frequency are seen in Figures 6.20 and 6.21. In these two figures it can be seen that when the coil RF power frequency increases from 1 to 13.56 MHz, the thrust and Isp values exhibit nearly the same behavior. After 13.56 MHz the thrust and Isp is decreasing with the same trend again. In conclusion, it can be said that, the full RF power absorption of the plasma occurs at the 13.56 MHz coil power RF frequency.

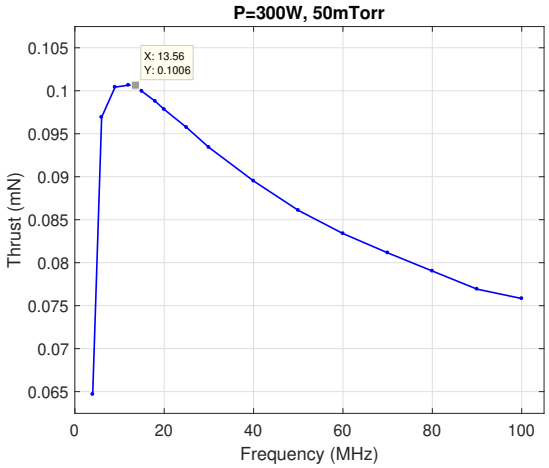

Figure 6.20: Frequency vs. Thrust distribution. 3 turn coils, coils are at the below of the chamber. V_{anode} is equal to $30\ V$ and V_{screen} is equal to $0\ V$, $P = 1.09486 \times 10^{-6} A/V^{3/2}$.

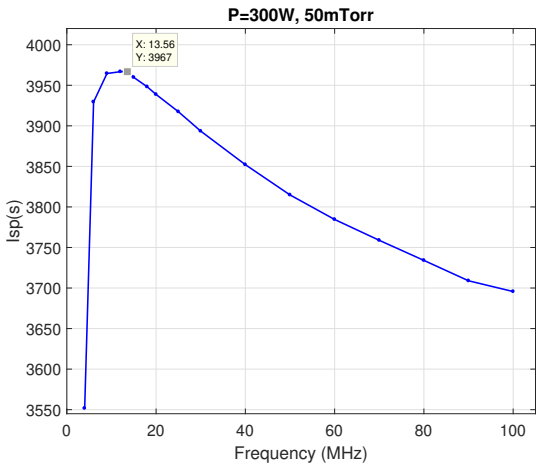

Figure 6.21: Frequency vs. Isp distribution. 3 turn coils, coils are at the below of the chamber. V_{anode} is equal to 30 V and V_{screen} is equal to 0 V, $P = 1.09486 \times 10^{-6} A/V^{3/2}$.

6.5 Simulations of the Electric Field, Electric Potential, and Ion Trajectories

In order to find the well focused ion trajectories for the given ion thruster, the case study is realized also with the electric potential distribution, electric field distribution and ion trajectory simulations with the Comsol software in this thesis. The electric potential and electric field simulations are realized with the Comsol AC/DC electrostatic module and the ion trajectories are simulated with the Charged Particle Tracing module. By using the electrostatic module, we get the strength and the directions of the electric field and the 2D distribution of the electric potential along the solution domain.

6.5.1 Comsol Electrostatic Module and Charged Particle Tracing Module as an Implemented Method

Electrostatic Module The electric field analysis is done according to the following two basic well-known relations.

$$\vec{E} = -\nabla V \tag{55}$$

where $\vec{E}$ is the electric field and V is the electric potential. Therefore, the E-field in any direction can be solved by negative rate of change of the electric potential according to Eq.55.

Boundary conditions chosen for these simulations are given as V_{anode} is 100 V, V_{screen} is 70 V and the following boundary conditions are calculated as V_{acc} is -352 V and V_{space} is -195.4 V and the parameters are set as $p = 50$ mTorr and $P = 300$ W.

Charged Particle Tracing Module Ion trajectories can be drawn by solving the following force equations.

$$\vec{F_e} = \frac{d(m_p \vec{v})}{dt} \tag{56}$$

$$where \;\; m_p = \frac{m_r}{\sqrt{1 - v.v/c^2}} \tag{57}$$

$$\vec{F_e} = eZ\vec{E} \tag{58}$$

where m_r is the particle mass (the propellant gas is the Argon in this thesis) at rest, e is the unit charge in C, $\vec{E}$ is the electric field, $\vec{F_e}$ is the electrical force. The selected conditions for this module are; Z (charge number) is 1, N (particle number per release) is 20 and 100, V_{0y} (initial particle velocity in the y-direction or Bohm velocity at the sheath edge) is approximately $3000\ m/s$.

6.5.2 Results and Discussions of the Comsol electrostatic and ion trajectories simulations

The simulated set-up is composed of two main parts; plasma chamber and the ion optics system as shown in Figure 6.22. Three-turn coil is wrapped around the plasma chamber. Two-grid ion optics system is placed on the chamber. The green electrode is the screen grid while the magenta color electrode is the accelerator grid. There are eighty-five holes on each electrode.

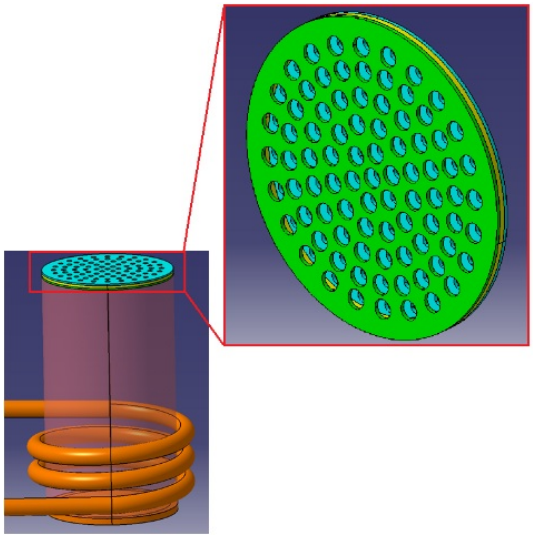

Figure 6.22: Thruster geometry and electrodes

The dimensions of the chamber and coils are given in Figure 6.23. The main geometrical dimensions are given as the chamber length $L = 53.6$ mm and the chamber diameter $D = 26.8$ mm which is determined from reference [57]. The coil diamater is $C = 4$ mm, the wall thickness of the dielectric chamber is $M = 1.6$ mm and the separation distance between coils is $T = 3$ mm.

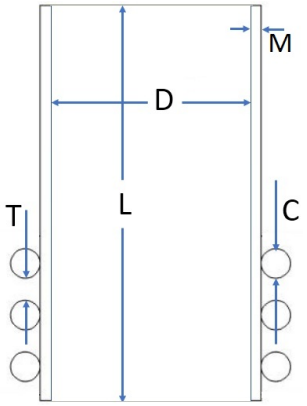

Figure 6.23: Thruster geometry

In order to study the electric potential and the electric field variations in 2D space, the simulations are initiated in the Comsol electrostatic module. Therefore, 2D ion optics solution domain is created firstly as shown in Figure 6.24. The electrostatic and ion trajectory solutions are computed in couple.

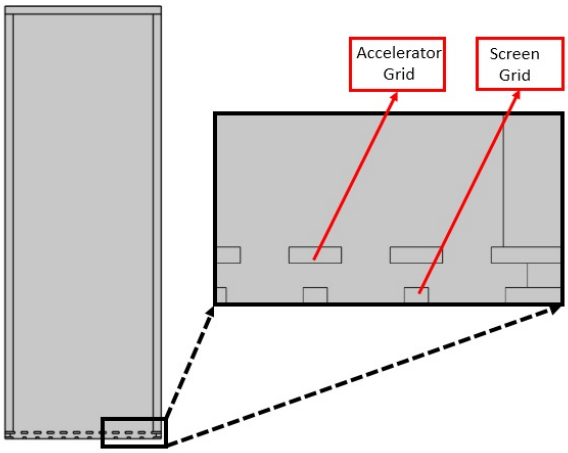

Figure 6.24: The solution domain along the screen and accel grids.

1D Electric potential variations along this solution domain are shown in Figure 6.25. On this figure two potential distributions are seen. One of them is the potential at the axis which is passing through the beamlet centerline and the other distribution is at the axis which is passing through the point between three apertures. The anode and screen potentials are defined as boundary conditions for the thruster and the net beam potential V_N and the potential drop between the screen grid and the accel grid V_T are calculated after plasma chamber simulations. At the last step, the electric potential distribution is obtained in Figure 6.25 along thruster and it is seen that the close-up results are taken from reference [11]

Potential variations along this solution domain in the 2-D are shown in Figure 6.26. From Figure 6.26 it is observed that the maximum positive potential on the screen grid is 70 V and maximum negative potential on the accelerator grid is -352 V. At the boundary of the domain, the space potential is -195.4 V.

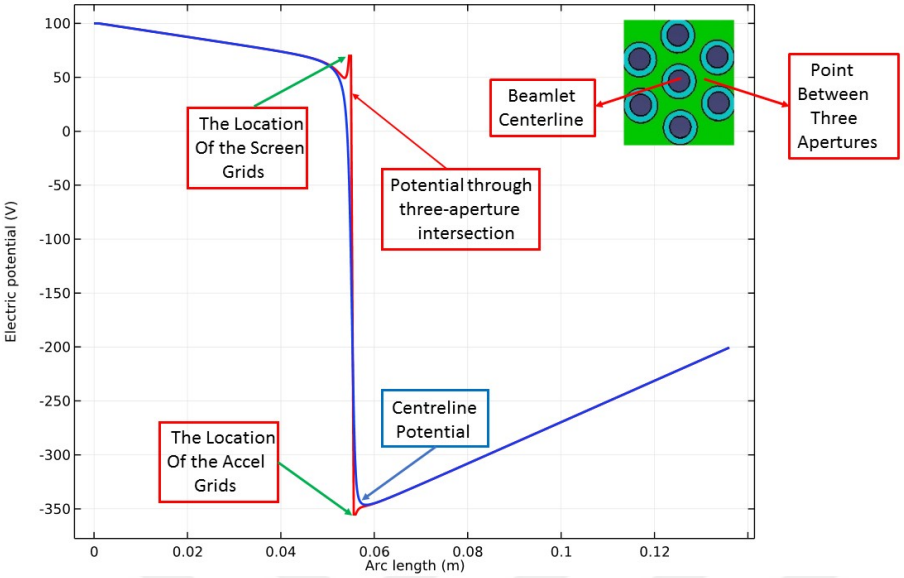

Figure 6.25: Potential variation along two different axis.

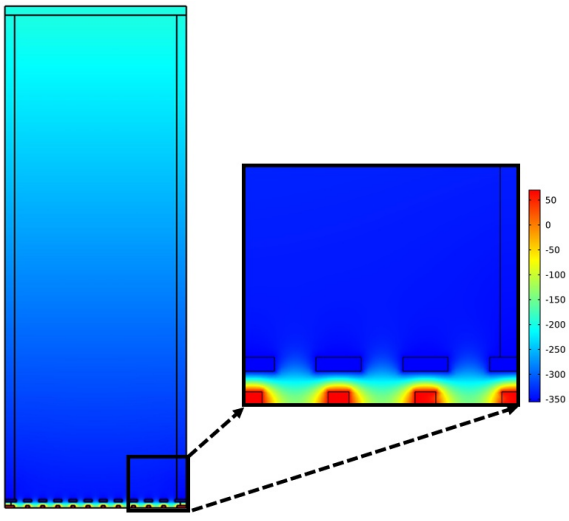

Figure 6.26: 2D electric potential distribution along the solution domain. Unit: Volts.

Furthermore, the equipotential lines of the electric potential in 2-D domain is seen in Figure 6.27. The color of each line corresponds to a unique electrical potential value and their quantities are seen from the color bar at the right side of Figure 6.27.

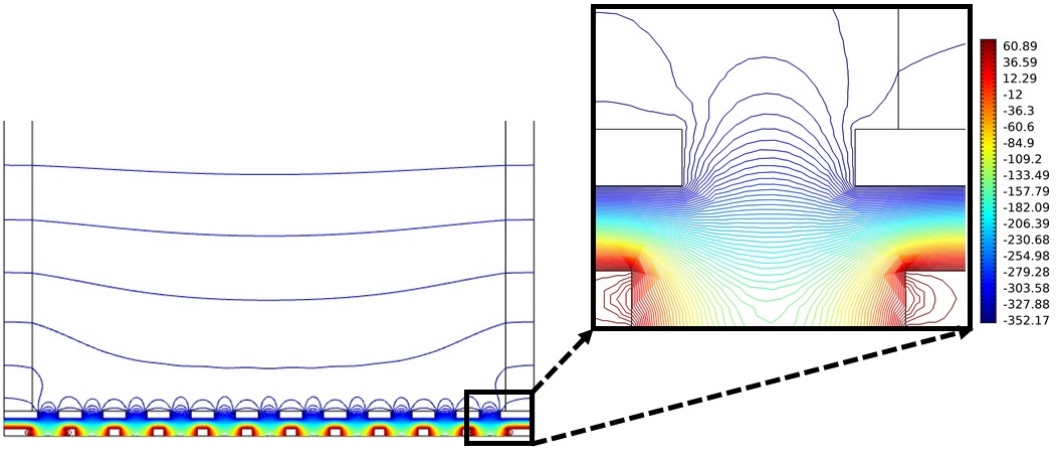

Figure 6.27: 2D electric equipotential lines along the solution domain. Unit:Volts.

In Figure 6.28, the magnitude of the electric field distribution along the 2-D domain is clearly observed. At the sharp edges, the field strength has the highest value. As it is known the stroke of lightning happens at sharp edges in nature, similarly the maximum electric field is expected to happen at these regions. As we know, the electric field is zero in the metals (grids). Between the grids, the field strength is high enough since the electric field vectors want to pass at the shortest path between the two metal surfaces.

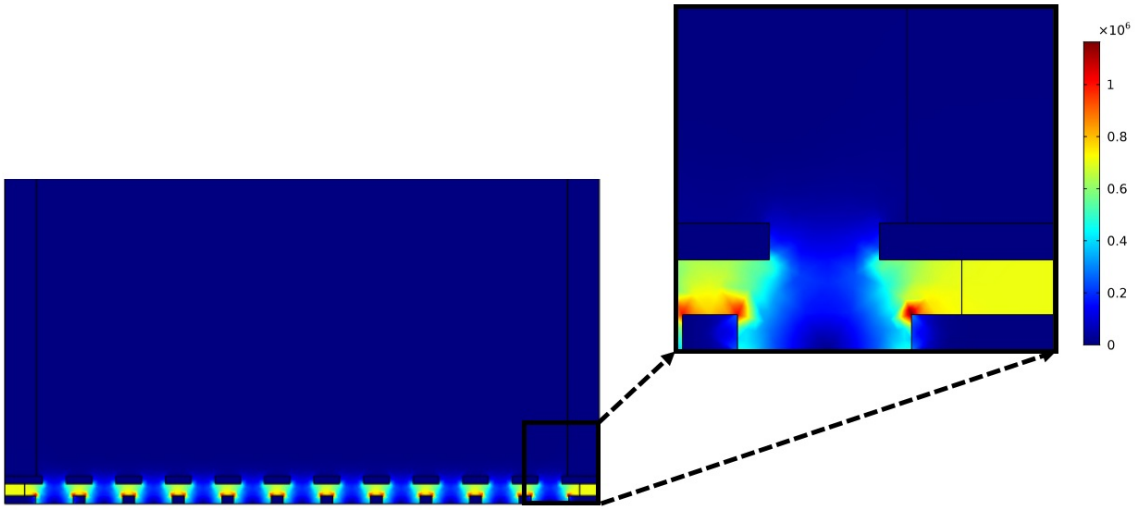

Figure 6.28: 2D magnitude of the electric field distribution. Units are in the V/m.

As seen from Figure 6.29, the E-field streamlines are perpendicular to the electric potential lines in 2-D domain. Also, the E-field lines can not penetrate the bulk metal body as known from electro-magnetism.

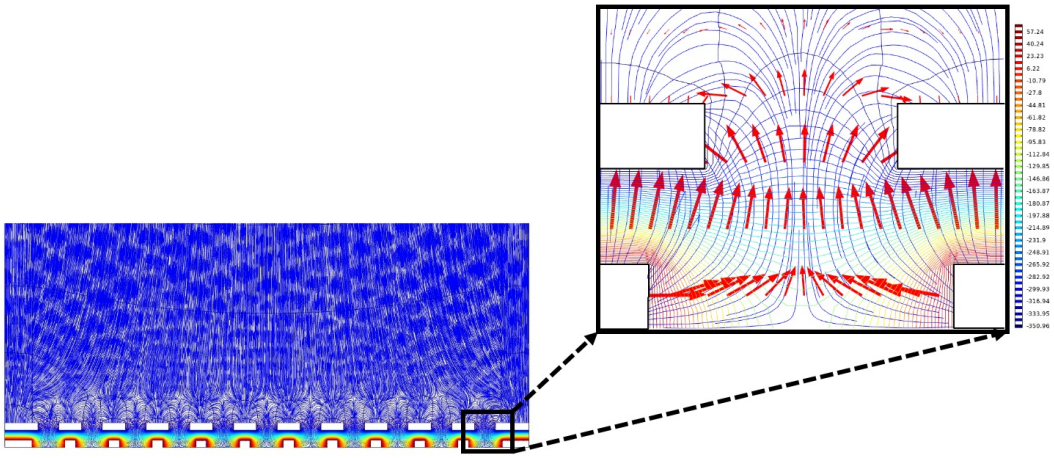

Figure 6.29: The electric field and potential iso-contour at 2D. Units: V/m and Volt.

Figures 6.30 to 6.33 show the ion trajectories and the electric equipotential lines of the ion optics system under different source origin. In Figure 6.30, the sheath is assumed to be flat and the ions are released from this flat line by changing the particles. Number of particles is $N = 20$ for the figure on the left and on the right figure $N = 100$. The color legends are shown at the right hand side as the electric potential contours (unit is V) and y-component of the ion velocity (unit is m/s). As compared

both shapes and the trajectories are completely the same looking like a cone.

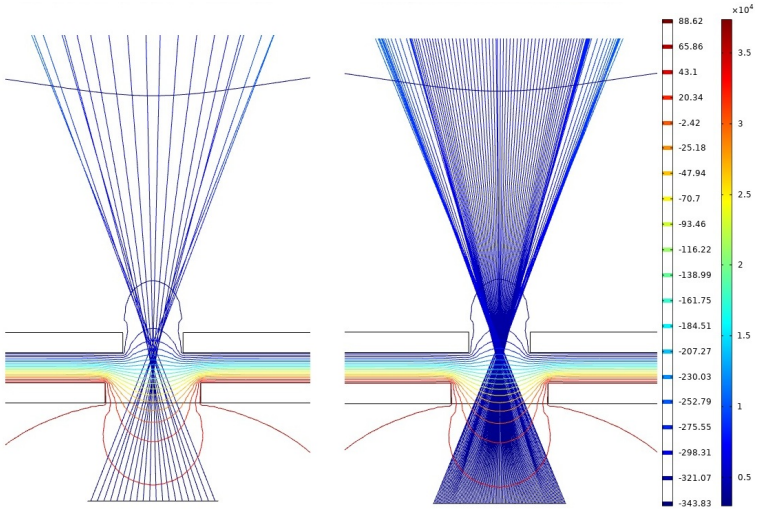

Figure 6.30: The ions are released from the sheath.

When the origin of the particles is changed to a concave surface, the particles are scattered more as seen in Figure 6.31. The crossing of trajectories are seen again. The color legends are shown at the right hand side as the electric potential contours (unit is V) and y-component of the ion velocity (unit is m/s).

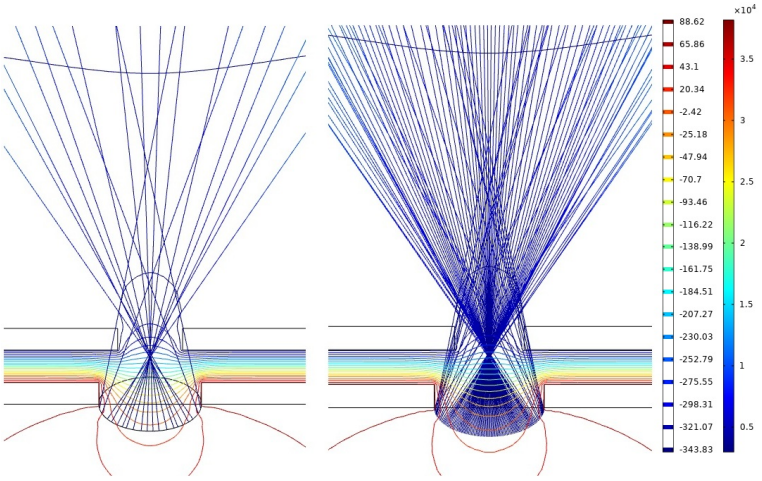

Figure 6.31: The ions are released from the concave boundary

When the origin of the particles is changed again to a flat surface along the screen electrodes, the particles are still scattered and the trajectories are crossing as observed in Figure 6.32. The color legends are shown at the right as the electric potential

contours (unit is V) and y-component of the ion velocity (unit is m/s)

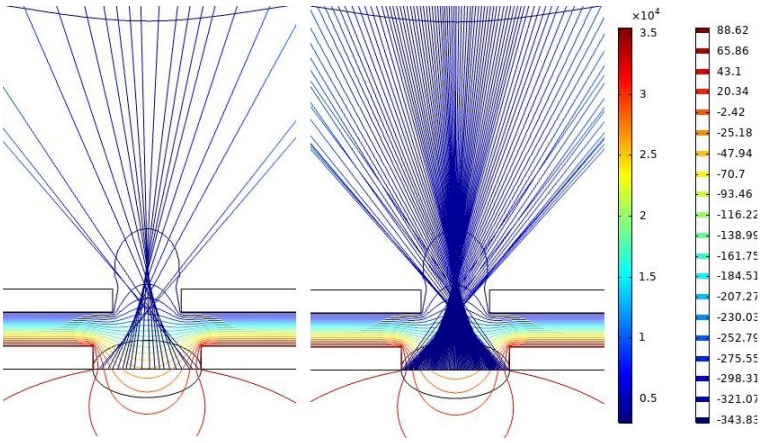

Figure 6.32: The ions are released from the flat boundary.

Figure 6.33 shows the focused ion beam with the 20 trajectories on the figure at the left and 100 trajectories (number particles) on figure at the right when the trajectories are all released from the convex surface. The separation of ions is clearly seen and they are not well-focused. Although these ion trajectories are not perfect, the performance calculations, thrust and Isp are done for this screen grid diameter as 1.9 mm and the calculation of the performance parameters is completed at the previous section. The color legends are shown at the right hand side as the electric potential contours (unit is V) and y-component of the ion velocity (unit is m/s).

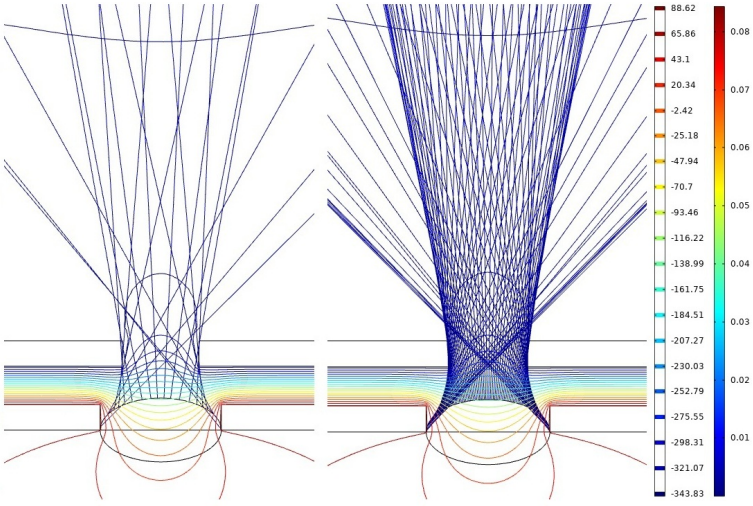

Figure 6.33: The ions are released from the convex boundary.

From Figure 6.34 is seen that when the release boundary of the ions is slided towards

the upper part of the screen grid as a convex shape, one can see that the trajectories of the ions are more suitable than the other previous cases and they are well-focused. The color legends are shown at the right hand side as the electric potential contour (unit is V) and y-component of the ion velocity (unit is m/s). At the same time the diameters of the screeen and accel grids are changed to the 1.2 mm and 1.0 mm respectively.

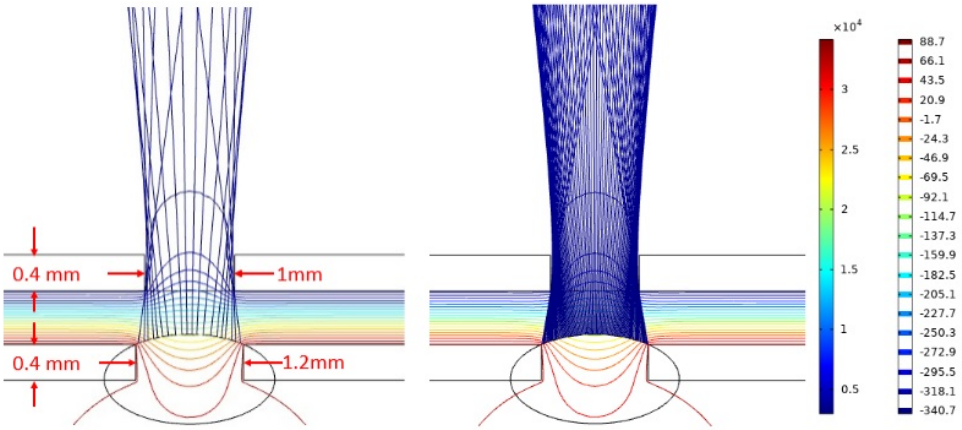

Figure 6.34: The ions are released from the convex boundary and at the upper part of the screen grid.

For comparison purposes experimentally observed well focused ion trajectories are presented in Figure 6.35. As an optimum case for proper ion trajectories, the lines of the ion passing through the accel grids are seen clearly thanks of the atomic luminescence of the ions as shown in Figure 6.35.

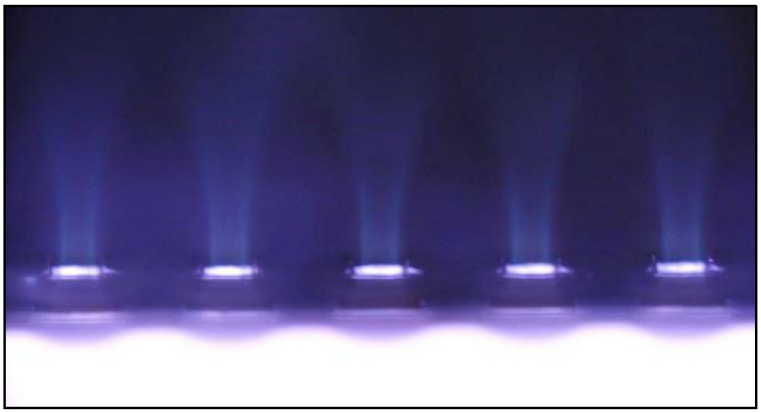

Figure 6.35: The experimentally observed well focused ion trajectories from a RF ICP ion thruster [13].

CHAPTER 7

CONCLUSION

This thesis is the first of its kind completed in the Aerospace Engineering Department of Middle East Technical University on the subject of plasma physics. No thesis have been completed until now on the topics of plasma physics related to electric propulsion. The thesis is about the design of a simple electric propulsion system called as "the inductively coupled ion thruster". The thruster is driven by a RF current source of variable frequency. Electric thrusters are of great interest in space propulsion due to their very high specific impulse values when compared to other propulsion systems. The specific impulse, Isp, values of electric propulsion systems are of the order of 2500-3600 seconds whereas those of the chemical propulsive systems have significantly low specific impulses. For example those of the mono-propellants are of 150 to 225 seconds and those of the bipropellants range between 300 - 450 seconds. This is the reason why electric propulsion is so attractive for space applications. Because of this significantly high value of their specific impulses the electric propulsion system of a space vehicle can function for very long periods of time. This makes the electric propulsion to be very attractive and provide a suitable solution for very long lasting deep space exploration missions. The thesis covers the fundamental concepts of the plasma systems, starting from the basic definitions of plasma, bulk plasma, sheath, Debye length, Bohm velocity and so on to extending to present a complete design of a simple ion thruster. Furthermore, the present design is validated by numerical simulations using the commercially available software package called COMSOL. COMSOL is a powerful numerical tool used for plasma calculations. It uses the FEM (Finite Element Method) to solve the plasma drift-diffusion equations and the well known Maxwell equations in couple. Hence in this respect, the thesis is a complete work of a propulsion system design whose results are validated by numeri-

cal simulations. In this thesis, a successful design of an "Inductively Coupled Plasma Ion Thruster" powered by means of a RF source, therefore the name ICP-RF, is presented. The overall concept description of the experimental plasma set-up is given in Figure 4.6 and the geometric details of the design are given in Figure 4.2, showing the basic dimensions in Figure 4.3. The number of coils is selected as variable (with minimum coil turn number 2, maximum coil turn number 23) and the wire diameter is 9.5 mm. With the given geometry and the boundary conditions specified in Figure 5.1 the solution domain is discretized by triangular finite elements of 106974 cells and the plasma flow is solved for electron temperature, Bohm velocity, ion density fields. For the solution procedure appropriate grid refinement is performed and the converged solutions are obtained using a personal computer. A typical convergence history for the solutions is presented in Figure 5.2. Once the computational method for the plasma system is validated, further analysis of the performance of the design are performed by changing various geometrical parameters of the thruster such as the coil turn numbers, coil geometry, the anode voltage, the RF frequency, the location of the coil and power of the RF source and the effects of these changes on the thruster performance are determined. Effect of changing the coil turn numbers for the design is treated in Chapter 5. When the coil number is changed from 3 to 23, it is seen that both the electron density and the ion density distributions within the plasma approach the Gaussian distributions. For each coil turn number increment case the quasi-neutrality of the plasma is sustained as seen from Figure 5.5-5.6, and 5.7. The sheath phenomena is observed at each boundaries for which the ion density is becoming more than the electron density in these regions. The effect of the coil location is also studied. When the coil location is approached to the screen grid, the ion density distribution exhibits an increase. When the coils are distributed uniformly around the chamber, with increasing coil turn numbers, the electric potential distribution also approaches the Gaussian distribution. The electron temperature distributions has the uniform distribution for high coil turns as seen in Figure 5.11 and when the coil number is 3, the electron temperature value is larger than other cases. The boundary conditions are specified and the resulting distribution obeys the boundary values at the anode and the screen grid as observed in Figures 5.13 and 5.14. The effect of changing the anode voltage on the plasma parameters are also investigated and the Child Langmuir sheath analysis is performed. It is clearly observed that for every

anode voltage the boundary conditions are well statisfied with the peak voltage value at the anode and zero voltage at the screen grid. At the screen grid location a very sharp voltage drop is observed within a very short distance of a few Debye lengths. Conversely this corresponds to a very sharp increase in the electric field at the same location. At this Child shield, the electron density goes nearly to zero while the ion density is highly increased. The plasma sheath phenomena is also clearly observed in Figure 5.14.

After tracing all the well focused trajectories of the ions, the geometry and the aspect ratio AR and turn coil numbers and their locations around the chamber are determined. The resulting electron temperature and the ion density, the Bohm velocity as well as the electric field values are calculated by simulating the flow using the COMSOL code. It was also possible to calculate the total ion current for the selected design parameters. For the present design it was determined that about 10 ions are generated and out of these 10 ions only 6 of them find their way through the successive grids. Of course, one has to keep in mind that this 10 unit of ions are the Child dependent current and is the maximum extractable current. This maximum level of current depends on the present geometry locations of the screen and the accelarator grids and is given by the perveance. Perveance is of course a function of the geometry and the atomic mass of the gas used as propellent in the thruster which in this case is Argon. Perveance is defined as the relation between the ion or the electron beam current and the extraction voltage of the source. The aperture size of the screen grid must therefore be determined for sufficient extraction of the ions. Besides, one has to keep in mind that the trajectories of the individual ions (stream lines in the case of fluid mechanics applications) must be carefully computed; such that they should neither intersect with other trajectories nor hit the boundaries of the screen and the accel grids as depicted in Figure 7.1.

After the Perveance and the Child limited current are calculated the potential difference between the screen and the accel grids is calculated. As stated in the text, this potential drop which has the value of V_T is not the net accelarator potential. Instead the net potential difference between the anode and the space voltages, V_N, must be used as the driving force for the calculations of the thrust. Then, one can easily calculate the specific impulse and therefore the thrust for the present plasma thruster.

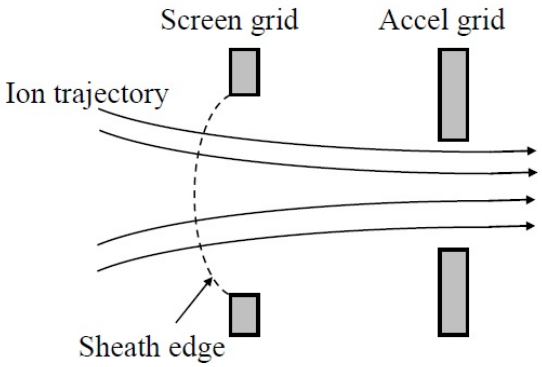

Figure 7.1: Optimum perveance [10].

Another important outcome of this thesis is probably related to the determination of the optimum grid dimensions for the ion thruster. A typical two gridded plasma thruster geometry with screen and accel grids is given in Figure 6.12. This figure also indicates the important dimensions to be specified for the design. This analysis is strikingly similar to geometrical optics since for determining the optimum shape of the ion trajectories, same concepts as in convex and concave lenses in optics are employed. The placement of the first grid, called the screen grid, and the second grid, called the accelarator grid, are very important to determine the trajectories of the ions such as the light beams in optics for determining the correct locations of the lenses. In these analysis the most suitable ion trajectories are found when the location of the released ions is on the outer edge of the screen grid (first grid) as a convex surface boundary and the ions are well aligned without any crossing over with other trajectories. In this case, the discharge from the thruster is at its best and the plume divergence is at its lowest level. Hence the key for achieving the best performance for the ion trajectories is not to cross over other trajectories. Every ion trajectory must be well aligned and exit the discharge slots of the grid without any interference with the slot geometry. These trajectories are well simulated by using the code COMSOL and the optimum geometry for design is determined by in general by simulating the ion flow through the grids. The performance parameters of the designed ion thruster is presented in Table 6.1. This table presents the values of most of the parameters used in the ion plasma thruster. These performance parameters are obtained for the optimum perveance value. For this a systematic analysis is performed to see the effect of pressure, (in fact vacuum) on the generated thrust and on the specific impulse

Isp as in Figure 6.15 ve Figure 6.16 respectively. The dependency of the thrust and the specific impulse values with respect to the supply power are presented in Figure 6.18 ve Figure 6.19 respectively. These are both non-linear dependency as one can expect and therefore they should be calculated. But one case simply say that with in increasing power both the thrust and the specific impulse values increase. Finally the dependency of the thrust and the specific impulse with respect to the frequency of the input power, since this is a RF ion plasma thruster, are given on Figure 6.20 ve Figure 6.21. These two figures are very similar in their trends and they both exhibit maxima values at a specific radio frequency for the specified iner gas Argon which is f=13.56 MHz. The results presented in this thesis cover only the theoretical and computational aspects of the plasma ion thruster. It would be a real challenge to realize the same study experimentally and compare the true experimental results with those of the simulations obtained from COMSOL code. This is a study that foreseen for the future most probably for the PhD thesis of the author.

REFERENCES

[1] J. R. Wertz and W. J. Larson, "Space mission analysis and design. torrance, ca (united states); microcosm," 1999.

[2] E. Bozkurt, Ü. E. Güngör, and N. Alemdaroğlu, "Validation and benchmarking of comsol 2d axisymmetric inductively coupled argon plasma model,"

[3] S. Mazouffre, "Electric propulsion for satellites and spacecraft: established technologies and novel approaches," *Plasma Sources Science and Technology*, vol. 25, no. 3, p. 033002, 2016.

[4] "http://cs.space.eads.net/sp/SpacecraftPropulsion/Rita/RIT-10.html."

[5] M. Tsay, K. Hohman, and L. Olson, "Micro rf ion engine for small satellite applications," 2009.

[6] F. F. Chen, *Introduction to plasma physics*. Springer Science & Business Media, 2012.

[7] R. Henrich, "Development of a plasma simulation tool for radio frequency ion thrusters," 2013.

[8] F. F. Chen and J. P. Chang, *Lecture notes on principles of plasma processing*. Springer Science & Business Media, 2012.

[9] F. Gao, S.-X. Zhao, X.-S. Li, and Y.-N. Wang, "Comparison between experiment and simulation for argon inductively coupled plasma," *Physics of Plasmas*, vol. 16, no. 11, p. 113502, 2009.

[10] L. T. Williams, *Ion acceleration mechanisms of helicon thrusters*. PhD thesis, Georgia Institute of Technology, 2013.

[11] C. C. Farnell, *Performance and lifetime simulation of ion thruster optics*. 2007.

[12] C. Sánchez Lara, "Design and performance analysis study of an ion thruster," B.S. thesis, Universitat Politècnica de Catalunya, 2016.

[13] Y. Nakayama and F. Tanaka, "Experimental visualization of ion thruster neutralization phenomena," *IEEE Transactions on Plasma Science*, vol. 43, no. 1, pp. 269–276, 2014.

[14] W. Ernst, M. Dieter, L. Helmut, and M. Karl, "Development and utilization objectives of a low-power arcjet for the p3-d (oscar) satellite," *IEPC Paper*, pp. 93–056, 1993.

[15] K. Sankaran, *Simulation of plasma flows in self-field lorentz force accelerators*. PhD thesis, Princeton University, 2004.

[16] O. Gorshkov, V. Shutov, K. Kozubsky, V. Ostrovsky, and V. Obukhov, "Development of high power magnetoplasmadynamic thrusters in the ussr," in *30th International Electric Propulsion Conference, Florence, Italy. IEPC-2007-136*, 2007.

[17] V. Hruby, J. Monheiser, and J. Kolencik, "A high thrust density, c60 cluster, ion thruster.," tech. rep., BUSEK CO INC NATICK MA, 1996.

[18] C. Yunculer, "One dimensional numerical analysis of plasma properties in the discharge channel of a hall effect thruster," Master's thesis, METU, the Turkey, September 2014.

[19] D. M. Goebel and I. Katz, *Fundamentals of electric propulsion: ion and Hall thrusters*, vol. 1. John Wilemazouffre2016electricy & Sons, 2008.

[20] R. V. Petrescu, R. Aversa, B. Akash, R. Bucinell, J. Corchado, F. Berto, M. Mirsayar, A. Apicella, and F. I. Petrescu, "Modern propulsions for aerospace-part ii," 2017.

[21] H. J. Leiter, R. Killinger, H. Bassner, J. Müller, and R. Kukies, "Development of the radio frequeny ion thruster rit xt-a status report," *Proceedings of the 27th Intern. Electric Propulsion Conferce, Pasadena, California, USA*, 2001.

[22] H. Bassner, R. Killinger, H. Leiter, and J. Müller, "Development steps of the rf-ion thrusters rit," in *27th International Electric Propulsion Conference*, pp. 01–105, 2001.

[23] H. Kuninaka and S. Satori, "Development and demonstration of a cathodeless electron cyclotron resonance ion thruster," *Journal of Propulsion and Power*, vol. 14, no. 6, pp. 1022–1026, 1998.

[24] M. M.-T. Tsay, *Two-dimensional numerical modeling of radio-frequency ion engine discharge*. PhD thesis, Massachusetts Institute of Technology, 2010.

[25] "http://www.space-propulsion.com/videos/artemis-recovery.html."

[26] I. Funaki, Y. Nakayama, H. Horisawa, and M. Ando, "Micro-thruster options for the japanese space gravitational wave observatory missions," in *IEPC, Presented at the 32nd International Electric Propulsion Conference*, vol. 308, 2011.

[27] F. Martel, L. Perna, and P. Lozano, "Miniature ion electrospray thrusters and performance test on cubesats," 2012.

[28] V. Pizzagalli, J. Gonzalez del Amo, D. Stramaccioni, and F. Ponti, "Darwin mission: The field emission electric propulsion (feep) option," in *4th International Spacecraft Propulsion Conference*, vol. 555, 2004.

[29] E. Turkoz and M. Celik, "2d rf ion thruster modeling with fluid plasma and analytical sheath formulation," in *Space Propulsion Conference, Cologne, Germany*, 2014.

[30] J. D. Gerst, *Investigation of magnetized radio frequency plasma sources for electric space propulsion*. PhD thesis, Université d'Orléans, 2013.

[31] J. Browning, C. Lee, D. Plumlee, S. Shawver, S. M. Loo, M. Yates, M. McCrink, and J. Taff, "A miniature inductively coupled plasma source for ion thrusters," *IEEE Transactions on Plasma Science*, vol. 39, no. 11, pp. 3187–3195, 2011.

[32] A. Aanesland, J. Bredin, L. Popelier, and P. Chabert, "Direction for the future-successive acceleration of positive and negative ions applied to space propulsion," *arXiv preprint arXiv:1411.1538*, 2014.

[33] N. Z. Warner, *Theoretical and experimental investigation of Hall thruster miniaturization*. PhD thesis, Massachusetts Institute of Technology, 2007.

[34] E. Kawamura, D. Graves, and M. Lieberman, "Fast 2d hybrid fluid-analytical simulation of inductive/capacitive discharges," *Plasma Sources Science and Technology*, vol. 20, no. 3, p. 035009, 2011.

[35] T. Suekane, T. Taya, Y. Okuno, and S. Kabashima, "Numerical studies on the nonequilibrium inductively coupled plasma with metal vapor ionization," *IEEE transactions on plasma science*, vol. 24, no. 3, pp. 1147–1154, 1996.

[36] E. Hammond, K. Mahesh, and P. Moin, "A numerical method to simulate radio-frequency plasma discharges," *Journal of Computational Physics*, vol. 176, no. 2, pp. 402–429, 2002.

[37] H. Kumar and S. Roy, "Two-dimensional fluid model of dc and rf plasma discharges in magnetic field," in *36th AIAA Plasmadynamics and Lasers Conference*, p. 4788, 2005.

[38] C.-C. Hsu, M. A. Nierode, J. W. Coburn, and D. B. Graves, "Comparison of model and experiment for ar, ar/o2 and ar/o2/cl2 inductively coupled plasmas," *Journal of Physics D: Applied Physics*, vol. 39, no. 15, p. 3272, 2006.

[39] B. Parent, S. O. Macheret, and M. N. Shneider, "Electron and ion transport equations in computational weakly-ionized plasmadynamics," *Journal of Computational Physics*, vol. 259, pp. 51–69, 2014.

[40] D. Y. Oh, *Computational modeling of expanding plasma plumes in space using a PIC-DSMC algorithm*. PhD thesis, Massachusetts Institute of Technology, 1996.

[41] J. M. Fife, *Hybrid-PIC modeling and electrostatic probe survey of Hall thrusters*. PhD thesis, Massachusetts Institute of Technology, 1998.

[42] J. J. Szabo, *Fully kinetic numerical modeling of a plasma thruster*. PhD thesis, Massachusetts Institute of Technology, 2001.

[43] M. Celik, M. Santi, S. Cheng, M. Martinez-Sanchez, and J. Peraire, "Hybrid-pic simulation of a hall thruster plume on an unstructured grid with dsmc collisions," in *28th International Electric Propulsion Conference*, pp. 17–20, Citeseer, 2003.

[44] D. M. Goebel, "Analytical discharge model for rf ion thrusters," *IEEE transactions on plasma science*, vol. 36, no. 5, pp. 2111–2121, 2008.

[45] P. Chabert, J. Arancibia Monreal, J. Bredin, L. Popelier, and A. Aanesland, "Global model of a gridded-ion thruster powered by a radiofrequency inductive coil," *Physics of Plasmas*, vol. 19, no. 7, p. 073512, 2012.

[46] M. M. Tsay and M. Martinez-Sanchez, "Simple performance modeling of a radio-frequency ion thruster," in *Proceedings of the 30th International Electric Propulsion Conference*, 2007.

[47] Y. Takao, K. Eriguchi, and K. Ono, "Two-dimensional particle-in-cell simulation of a micro rf ion thruster," in *Proceedings of the 32nd International Electric Propulsion Conference*, pp. 1–11, Electric Rocket Propulsion Soc. Fairview Park, OH, 2011.

[48] R. Henrich and C. Heiliger, "Three dimensional simulation of micro newton rits," in *33rd International Electric Propulsion Conference*, 2013.

[49] S. Eliezer and Y. Eliezer, *The fourth state of matter: an introduction to plasma science*. CRC Press, 2001.

[50] C. Hartman, G. Carlson, M. Hoffman, R. Werner, and D. Cheng, "A conceptual fusion reactor based on the high-plasma-density z-pinch," *Nuclear Fusion*, vol. 17, no. 5, p. 909, 1977.

[51] M. A. Lieberman and A. J. Lichtenberg, *Principles of plasma discharges and materials processing*. John Wiley & Sons, 2005.

[52] E. Turkoz and M. Celik, "Aether: A simulation platform for inductively coupled plasma," *Journal of Computational Physics*, vol. 286, pp. 87–102, 2015.

[53] A. O. Brezmes and C. Breitkopf, "Simulation of inductively coupled plasma with applied bias voltage using comsol," *Vacuum*, vol. 109, pp. 52–60, 2014.

[54] A. O. Brezmes and C. Breitkopf, "Fast and reliable simulations of argon inductively coupled plasma using comsol," *Vacuum*, vol. 116, pp. 65–72, 2015.

[55] C. Jia, J. Linhong, W. Kesheng, H. Chuankun, and S. Yixiang, "Two-dimensional simulation of inductively coupled plasma based on comsol and

comparison with experimental data," *Journal of Semiconductors*, vol. 34, no. 6, p. 066004, 2013.

[56] "COMSOL Multiphysics 4.3b Manual." `https://www.airpbortcab.ga/forum/thread/attachment/146641/models.plasma.oxygen_gec_icp-28971.pdf`.

[57] R. E. Wirz, "Miniature ion thrusters: A review of modern technologies and mission capabilities," in *Joint Conference of 30th ISTS, 34th IEPC and 6th NSAT*, Univ. of California Los Angeles, CA, 2015.

[58] R. A. Martinez and J. D. Williams, "Electric field breakdown characteristics of carbon-based ion optics," in *IEPC-2005–284*, 2005.

[59] G. Aston, H. Kaufman, and P. Wilbur, "Ion beam divergence characteristics of two-grid accelerator systems," *AiAA Journal*, vol. 16, no. 5, pp. 516–524, 1978.

[60] M. Tartz, E. Hartmann, R. Deltschew, and H. Neumann, "Study of extraction grid erosion in a long-time ion thruster operational test," Paper IEPC-03-176, 28th Int. Electric Propulsion Conf., Toulouse, 17.-21, 2003.

[61] J. Foster, T. Haag, H. Kamhawi, M. Patterson, S. Malone, and F. Elliot, "The high power electric propulsion (hipep) ion thruster," in *40th AIAA/ASME/SAE/ASEE Joint Propulsion Conference and Exhibit*, p. 3812, 2004.

[62] M. Dobkevicius, *Modelling and design of inductively coupled radio frequency gridded ion thrusters with an application to Ion Beam Shepherd type space missions*. PhD thesis, University of Southampton, 2017.

[63] B. Lotz, "Plasma physical and material physical aspects of the application of atmospheric gases as a propellant for ion-thruster of the rit-type," 2013.

Appendix A

THE DERIVATION OF THE THRUST DENSITY EQUATION

The space charge limited current density is stated in the Eqn C1.

$$J = \frac{4\sqrt{2}}{9}\varepsilon_0\left(\frac{e}{M_i}\right)^{1/2}\frac{V_a^{3/2}}{d^2} \tag{A1}$$

The conservation of electric energy is stated in the Eqn C2

$$\frac{1}{2}M_i v_{ex}^2 = eV_a \tag{A2}$$

V_a is given at the Eqn C3

$$V_a = \frac{M_i v_{ex}^2}{2e} \tag{A3}$$

The thrust which the EP device produces is stated in the Eqn A4

$$T = \dot{m}v_{ex} \tag{A4}$$

The relation between the consumed mass flow rate and the electrical current is given at the Eqn C5

$$\dot{m} = I\frac{M_i}{e} \tag{A5}$$

The thrust in a modified view is given at the Eqn C6.

$$T = I\frac{M_i}{e}v_{ex} \tag{A6}$$

The relation between current and current density is given at the Eqn A7.

$$I = JA \tag{A7}$$

The relation between thrust, current density, atomic mass and propelant gas exhaust velocity is stated in the Eqn C8.

$$T = AJ\frac{M_i}{e}v_{ex} \tag{A8}$$

After substitution of the Eqn C1 and Eqn A7 into Eqn C8, the Eqn C9 is obtained.

$$\frac{T}{A} = \frac{4\sqrt{2}}{9}\varepsilon_0\left(\frac{e}{M_i}\right)^{1/2}\frac{V_a^{3/2}}{d^2}\frac{M_i}{e}v_{ex} \tag{A9}$$

After substitution of the Eqn C3 into Eqn C9, the Eqn C10 is obtained.

$$\frac{T}{A} = \frac{4\sqrt{2}}{9}\varepsilon_0\left(\frac{e}{M_i}\right)^{1/2}\frac{1}{d^2}\left(\frac{M_i v_{ex}^2}{2e}\right)^{3/2}\frac{M_i}{e}v_{ex} \tag{A10}$$

At the last step, the equation of the thrust density is obtained and it is shown in the Equation C11

$$\frac{T}{A} = \frac{2}{9e^2}\varepsilon_0\frac{v_{ex}^4}{d^2}M_i^2 \tag{A11}$$

Appendix B

THE DERIVATION OF THE TSIOLKOVSKY ROCKET EQUATION

$$T = -\frac{\mathrm{d}}{\mathrm{d}t}(m_p v_{ex}) \tag{B1}$$

Where the m_p is the propellant mass, and v_{ex} is the exhaust gas velocity. Obtained thrust is the opposite side of the time rate of the change of the momentum which ejected propellant carries.

$$-\frac{\mathrm{d}m_p v_{ex}}{\mathrm{d}t} = -v_{ex}\frac{\mathrm{d}m_p}{\mathrm{d}t} - m_p\frac{\mathrm{d}v_{ex}}{\mathrm{d}t} \tag{B2}$$

With the chain rule of the derivation of the Eqn B1, Eqn B2 is obtained. Due to the constant exhaust gas velocity, the time derivative of the it equals to zero and it drops.

$$M(t) = m_p + m_d \tag{B3}$$

The sum of the propellant mass and the spacecraft dry mass is the total mass $M(t)$ and it is written at the Eqn B3.

$$\frac{\mathrm{d}M(t)}{\mathrm{d}t} = \frac{\mathrm{d}m_p}{\mathrm{d}t} + \frac{\mathrm{d}m_d}{\mathrm{d}t} \tag{B4}$$

The time rate of the change of the total mass is given at the Eqn B4 and the time rate of change of the dry mass drops due to constant spacecraft mass.

$$M(t)\frac{\mathrm{d}v}{\mathrm{d}t} = -v_{ex}\frac{\mathrm{d}m_p}{\mathrm{d}t} \tag{B5}$$

When the term dm_p/dt from the Eqn. B4 is inserted to the Eqn B5, the Eqn B6 is obtained.

$$M(t)\frac{\mathrm{d}v}{\mathrm{d}t} = -v_{ex}\frac{\mathrm{d}M(t)}{\mathrm{d}t} \tag{B6}$$

After canceling of the dt of the Eqn B6, the Eqn B7 is obtained with the integration of the initial and final states.

$$\int_{v_i}^{v_f} dv = -v_{ex}\int_{M_i}^{M_f}\frac{\mathrm{d}M(t)}{M(t)} \tag{B7}$$

$$(v_f - v_i) = \triangle v = -v_{ex}(lnM_f - lnM_i) \tag{B8}$$

$$ln(\frac{M_f}{M_i}) = -\frac{\triangle v}{v_{ex}} \tag{B9}$$

$$M_f = M_i exp(-\frac{\triangle v}{v_{ex}}) \tag{B10}$$

$$m_d = (m_p + m_d)exp(-\frac{\triangle v}{v_{ex}}) \tag{B11}$$

$$m_d = m_p exp(-\frac{\triangle v}{v_{ex}}) + m_d exp(-\frac{\triangle v}{v_{ex}}) \tag{B12}$$

The Rocket Eqn. B13 is obtained at that final step. The required propellant mass is depend on the mission $\triangle v$, the exhaust gas velocity v_{ex} and dry mass m_d.

$$m_p = m_d(e^{\frac{\triangle v}{v_{ex}}} - 1) \tag{B13}$$

Appendix C

THE DERIVATION OF FREQUENCY DOMAIN AMPERE'S LAW EQUATION

Ampere's Maxwell law differential equation form is given the Eqn C1

$$\vec{\nabla} \times \vec{H} = \vec{J} + \frac{\partial \vec{D}}{\partial t} \tag{C1}$$

$$\vec{J} = \sigma \vec{E} + \sigma \vec{v} \times \vec{B} + \vec{J^e} \tag{C2}$$

$$\vec{\nabla} \times \vec{H} = \sigma \vec{E} + \vec{J^e} + \frac{\partial \vec{D}}{\partial t} \tag{C3}$$

$$\vec{E} = -\frac{\partial \vec{A}}{\partial t}, \;\; \vec{A} = e^{jwt}, \;\; \vec{E} = -jw\vec{A} \tag{C4}$$

$$\vec{D} = \varepsilon_0 \varepsilon_r \vec{E}, \;\; \vec{D} = -jw\varepsilon_0 \varepsilon_r \vec{A} \tag{C5}$$

$$\frac{\partial \vec{D}}{\partial t} = -jw\varepsilon_0 \varepsilon_r \frac{\partial \vec{A}}{\partial t}, \;\; \frac{\partial \vec{A}}{\partial t} = -\vec{E} \tag{C6}$$

$$\frac{\partial \vec{D}}{\partial t} = jw\varepsilon_0 \varepsilon_r (-jw\vec{A}) \tag{C7}$$

$$\frac{\partial \vec{D}}{\partial t} = w^2 \varepsilon_0 \varepsilon_r \vec{A} \tag{C8}$$

$$\vec{\nabla} \times \vec{H} = -\sigma j w \vec{A} + \vec{J^e} + w^2 \varepsilon_0 \varepsilon_r \vec{A} \tag{C9}$$

$$(jw\sigma - w^2 \varepsilon_0 \varepsilon_r)\vec{A} + \vec{\nabla} \times \vec{H} = \vec{J^e}, \;\; \vec{H} = \mu_0^{-1} \mu_r^{-1} \vec{B} \tag{C10}$$

$$(jw\sigma - w^2 \varepsilon_0 \varepsilon_r)\vec{A} + \vec{\nabla} \times (\mu_0^{-1} \mu_r^{-1} \vec{B}) = \vec{J^e}, \;\; \vec{B} = \vec{\nabla} \times \vec{A} \tag{C11}$$

$$(jw\sigma - w^2 \varepsilon_0 \varepsilon_r)\vec{A} + \vec{\nabla} \times (\mu_0^{-1} \mu_r^{-1} \vec{\nabla} \times \vec{A}) = \vec{J^e} \tag{C12}$$

Appendix D

THE DERIVATION OF THE CHILD LANGMUIR LAW

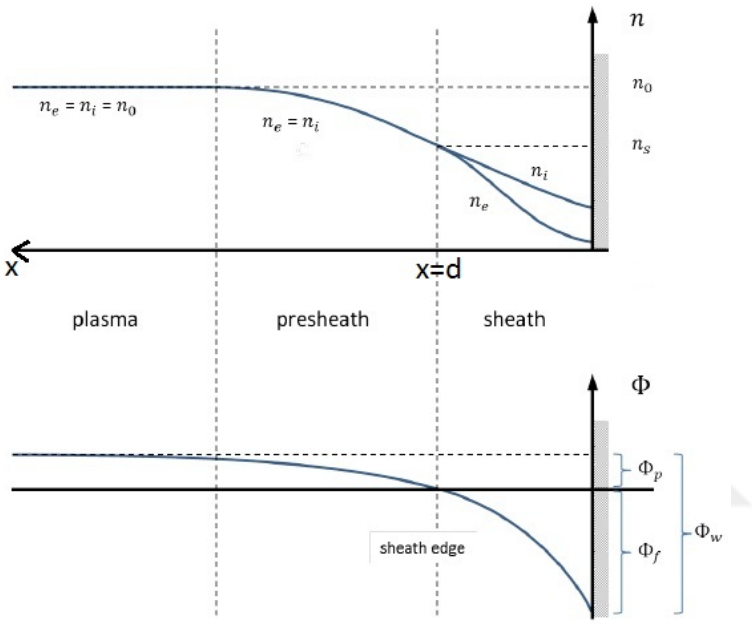

Figure D.1: Plasma sheath and sheath edge

From the conservation of the energy the Equation D1 is obtained.

$$v(x) = \sqrt{\frac{2e}{M_i}}\Big(\phi_0 - \phi(x)\Big)^{1/2} \tag{D1}$$

The total ion current density is written in the Equation D2.

$$J_i(x) = n_i(x)e\sqrt{\frac{2e}{M_i}}\Big(\phi_0 - \phi(x)\Big)^{1/2} = cnst \tag{D2}$$

The ion number density is obtaned in the Equation D3.

$$n_i(x) = \frac{1}{e} J_i \sqrt{\frac{M_i}{2e}} \frac{1}{\Big(\phi_0 - \phi(x)\Big)^{1/2}} \tag{D3}$$

$$n_i(x) = \frac{J_i}{e} \left(\frac{M_i}{2e} \frac{1}{\phi_0 - \phi(x)} \right)^{1/2} \tag{D4}$$

The Poisson's Equation is written in the Equation D5.

$$\frac{\mathrm{d}^2\phi(x)}{\mathrm{d}x^2} = -\frac{en_i}{\varepsilon_0} \tag{D5}$$

If the ion number density is inserted into the Poisson's equation, the Equation D6 is obtained.

$$\frac{\mathrm{d}^2\phi(x)}{\mathrm{d}x^2} = -\frac{J_i}{\varepsilon_0} \left(\frac{M_i}{2e} \frac{1}{\phi_0 - \phi(x)} \right)^{1/2} \tag{D6}$$

To integrate the Equation D6, each side of the Equation D6 is multiplied with the $d\phi/dx$

$$\frac{\mathrm{d}^2\phi(x)}{\mathrm{d}x^2} \frac{\mathrm{d}\phi}{\mathrm{d}x} = -\frac{J_i}{\varepsilon_0} \left(\frac{M_i}{2e} \frac{1}{\phi_0 - \phi(x)} \right)^{1/2} \frac{\mathrm{d}\phi}{\mathrm{d}x} \tag{D7}$$

The differentiation rule in the Equation D8 can be written mathematically.

$$2\frac{\mathrm{d}^2\phi}{\mathrm{d}x^2} \frac{\mathrm{d}\phi}{\mathrm{d}x} = \frac{\mathrm{d}}{\mathrm{d}x} \left(\frac{\mathrm{d}\phi}{\mathrm{d}x} \right)^2 \tag{D8}$$

The right side of the Equation D8 equals to the right side of the Equation D7. The Equation D9 is obtained after this equalization step.

$$\frac{\mathrm{d}}{\mathrm{d}x} \left(\frac{\mathrm{d}\phi}{\mathrm{d}x} \right)^2 = -2\frac{J_i}{\varepsilon_0} \left(\frac{M_i}{2e} \frac{1}{\phi_0 - \phi(x)} \right)^{1/2} \frac{\mathrm{d}\phi}{\mathrm{d}x} \tag{D9}$$

The Equation D10 is obtained, after the canceling of the dx for each side in the Equation D9,

$$d\left(\frac{\mathrm{d}\phi}{\mathrm{dx}}\right)^2 = -2d\phi\frac{J_i}{\varepsilon_0}\left(\frac{M_i}{2e}\frac{1}{\phi_0-\phi(x)}\right)^{1/2} \tag{D10}$$

The electric field can be written with the minus gradient of the electric potential function as seen the Equation D11.

$$E = -\frac{d\phi}{dx} \tag{D11}$$

If the electric field is inserted into the Equation D10, the Equation D12 is obtained.

$$d(-E)^2 = -2d\phi\frac{J_i}{\varepsilon_0}\left(\frac{M_i}{2e}\frac{1}{\phi_0-\phi(x)}\right)^{1/2} \tag{D12}$$

The Equation D13 is obtained after doing variable replacement with the $u(x)$.

$$\phi_0-\phi(x) = u(x), \frac{\mathrm{d}u}{\mathrm{d}x} = -\frac{\mathrm{d}\phi}{\mathrm{d}x}, du = -d\phi \tag{D13}$$

After inserting to $u(x)$ and du to the Equation D12, the first integral equation is obtained in the Equation D14.

$$\int d(E)^2 = 2\frac{J_i}{\varepsilon_0}\left(\frac{M_i}{2e}\frac{1}{u(x)}\right)^{1/2}\int du \tag{D14}$$

After once differentiation of the Equation D14, the Equation D15 is obtained.

$$E^2 = 4\frac{J_i}{\varepsilon_0}\left(\frac{M_i}{2e}\right)^{1/2}u^{1/2} \tag{D15}$$

$$E = \frac{\mathrm{d}\phi}{\mathrm{d}x} = \left(4\frac{J_i}{\varepsilon_0}\left(\frac{M_i}{2e}\right)^{1/2}u^{1/2}\right)^{1/2} \tag{D16}$$

$$\frac{\mathrm{d}\phi}{\mathrm{d}x} = 2\sqrt{\frac{J_i}{\varepsilon_0}}\left(\frac{M_i}{2e}\right)^{1/4} u^{1/4} \tag{D17}$$

From changing the variable $u(x)$ to $\phi(x)$ the Equation D18 is obtained

$$\frac{\mathrm{d}\phi}{\mathrm{d}x} = 2\sqrt{\frac{J_i}{\varepsilon_0}}\left(\frac{M_i}{2e}\right)^{1/4} \Big(\phi_0 - \phi(x)\Big)^{1/4} \tag{D18}$$

After obtaining the differential equation D18, the integral equation D19 can be obtained.

$$\int_0^{\phi(x=l_e)} \frac{d\phi}{\Big(\phi_0 - \phi(x)\Big)^{1/4}} = 2\sqrt{\frac{J_i}{\varepsilon_0}}\left(\frac{M_i}{2e}\right)^{1/4} \int_0^{x=l_e} dx \tag{D19}$$

The equation D20 is obtained after the differentiation of the Equation D19.

$$\Big(\phi_0 - \phi(x)\Big)^{3/4} = \frac{3}{2}\sqrt{\frac{J_i}{\varepsilon_0}}\left(\frac{M_i}{2e}\right)^{1/4} l_e \tag{D20}$$

With the extraction of the J_i to left side from the Equation D20, Equation D21 is obtained.

$$J_i = \frac{4\varepsilon_0}{9}\sqrt{\frac{2e}{M_i}}\frac{\big(\phi_0 - \phi(x)\big)^{3/2}}{l_e^2} \tag{D21}$$

The Equation D21 is known as Child Langmir Law and it determines to the space charge limited current.